ISSN 1068-3755, Surface Engineering and Applied Electrochemistry, 2007, Vol. 43, No. 4, pp. 231–238. © Allerton Press, Inc., 2007.
Original Russian Text © A.I. Dikusar, I.A. Ivanenkov, B.P. Saushkin, S.A. Silkin, S.P. Yushchenko, 2007, published in Elektronnaya Obrabotka Materialov, 2007, No. 4, pp. 4–11.

ELECTRIC DIMENSIONAL TREATMENT OF MATERIALS

High-Speed Anode Dissolution of Heat-Resistant Chrome–Nickel Alloys Containing Tungsten and Rhenium: III. Chloride–Nitrate Solutions

A. I. Dikusar[1, 2], I. A. Ivanenkov[3], B. P. Saushkin[3], S. A. Silkin[2], and S. P. Yushchenko[1, 2]

[1] *Institute of Applied Physics, Academy of Sciences of Moldova, ul. Akademiei 5, Chisinau, MD-2028 Moldova*
[2] *Pridnestrovskii Shevchenko State University, ul. 25 Oktyabrya 128, Tiraspol', Moldova*
[3] *MATI-RGTU Tsiolkovskii Russian State University of Technology, Berezhkovskaya nab. 14, Moscow, 109240 Russia*

Received October 26, 2006

Abstract—The anodic dissolution rates of two heat-resistant tungsten (12 wt %) and tungsten and rhenium (8 wt % W : 6 wt % Re) alloys in chloride, nitrate, and chloride–nitrate (30 g/l NaCl : 120 g/l $NaNO_3$) electrolytes have been compared. An excess of the critical current density i_{crit} depending on the hydrodynamic conditions leads to (i) the decreasing dependence of the current efficiency on the current density and (ii) the independence of the dissolution rate on the solution content. The mass-transfer mechanism, which determines the dissolution rate and the structure of superficial layers at $i > i_{crit}$, is discussed. Data on the chemical content of the surface layers depending on the machining modes are presented. The modes of the electrochemical dimensional machining (ECDM) of the parts made of these alloys are offered to attain the best performance parameters for machining.

DOI: 10.3103/S1068375507040011

INTRODUCTION

Chloride–nitrate mixtures have widespread application in the ECDM of heat-resistant Cr–Ni alloys due to their polymorphism [1–6]. As a rule, this processing makes it possible to equalize the rate of anodic dissolution for various phases of the alloys and, in so doing, to improve a number of the technological characteristics of the machining along with the finish quality of the surface layer [4–6]. The electrochemical aspects of the high-rate dissolution of Cr–Ni alloys containing tungsten and rhenium in chloride and nitrate solutions were outlined in [7, 8]. The optimum conditions of the machining were studied in [8]. These conditions are defined by a noticeable oxidation of the surface layers, which occurs at a current density in excess of some critical value; this value depends on the hydrodynamic regime. The oxidation causes the value of the current yield, as well as other characteristics of the surface finish quality, to decrease.

In this paper, the high-rate anodic dissolution of the above-mentioned alloys in a mixed chloride–nitrate electrolyte is outlined.

EXPERIMENTAL

The anodic dissolution of two Cr–Ni alloys of different compositions was investigated (see table). The investigation was performed using the procedure in [7, 8], which differed in two points: (i) the maximum current densities obtained were about 30 A/cm^2 and (ii) the anodic dissolution was carried out in a NaCl (0.5 M) : $NaNO_3$ (1.5 M) mixture that corresponds to NaCl (30 g/l) : $NaNO_3$ (120 g/l).

RESULTS AND DISCUSSION

Polarization Measurements

Figures 1 and 2 give the results of the galvanoscope polarization measurements. First, at a current density below the critical value i_{crit}, the dissolution is in progress under a lower potential than in the case of a solution containing only nitrates (Fig. 2); the nature of this phenomenon will be discussed later. Second, the rhenium-containing alloy denoted as alloy I shows a lower dissolution potential at any current density. Third, as shown in Fig. 2, the dissolution potential for a ZhS-6U alloy exceeds the one obtained in a nitrate solution with 2M $NaNO_3$ at $i > i_{crit}$.

As is clear from Figs. 1 and 2 as well as from [7], at $i > i_{crit}$, the dissolution potential in this solution exceeds the one observed for rhenium-containing alloy I and is less for the ZhS-6U alloy as compared to the chloride (2M NaCl) solution used.

The critical value i_{crit} in the chloride solution is correlated to the salt passivation due to the formation of a saturated solution at the surface of an alloy from the products of anodic dissolution of nickel and cobalt as the main components [7]. The closely related values of

Surface composition of investigated alloys

Alloy	Observing site in the figure	i, A/cm^2	Phase	Ni	Cr	W	Re	Co	Ti	Al	C	Si	O
Alloy I			Starting phase	62.1 ± 0.1	4.8 ± 0.1	7.8 ± 0.5	5.6 ± 0.7	10.1 ± 0.4	–	5.0 ± 0.3	3.7 ± 0.2	0.9 ± 0.1	–
	4a and 4b	2.0		59.6 ± 0.4	5.2 ± 0.2	11.0 ± 0.2	1.2	10.2 ± 0.5	–	4.8 ± 0.5	4.6 ± 0.5	~0.03	3.5 ± 0.5
	4c	5.0	Main phase	75.9 ± 0.6	2.5 ± 0.3	–	–	8.4 ± 0.2	–	10.4 ± 0.2	–	2.9 ± 0.1	–
	4d		Oxidized phase	51.1 ± 0.3	5.5 ± 0.3	11.8 ± 0.7	–	8.4 ± 0.4	–	4.5 ± 0.5	11.2 ± 0.4	–	7.8 ± 0.2
			Average value	63.5	4.0	5.9	–	8.4	–	7.5	5.6	1.5	3.9
	4f	29.0	Main phase	61.9 ± 6.3	4.5 ± 1.4	10.2 ± 2.4	5.9 ± 1.6	9.0 ± 0.6	–	6.9 ± 1.6	–	–	4.7 ± 1.7
	4e		Oxidized phase	13.1	7.8	42.2	–	2.7	–	–	–	4.9	29.0
ZhS-6U			Starting phase	56.5 ± 0.8	9.1 ± 0.7	12.1 ± 2.0	–	9.5 ± 0.4	2.6 ± 0.5	5.5 ± 0.1	4.5 ± 0.6	–	–
	5b	2.0	Main phase	57.1	8.1	14.5	–	10.0	1.8	5.2	3.2	–	–
	5a		Oxidized phase	15.9 ± 7.3	3.4 ± 1.0	39.1 ± 6.8	–	2.7 ± 1.4	15.8 ± 6.8	~0.5	13.3 ± 0.3	–	9.4 ± 3.1
	5d	5.0	Main phase	62.2 ± 3.6	6.8 ± 2.2	9.2 ± 4.5	–	8.8 ± 1.6	3.9 ± 1.5	6.6 ± 0.7	~2.5	–	–
	5c		Oxidized phase	10.8	2.8	43.8	–	–	23.8	–	11.5	–	7.3
	5f	25.0	Main phase	43.6 ± 4.1	7.9 ± 2.7	23.1 ± 2.8	–	8.5 ± 0.2	–	~2.2	~2.0	–	13.9 ± 1.5
	5e		Oxidized phase	9.9	7.6	59.0	–	1.8	–	–	–	–	21.6

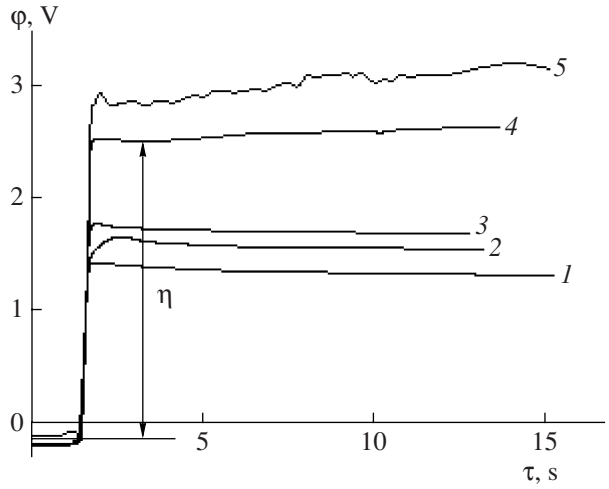

Fig. 1. Potential for anodic dissolution of (*1*, *3*, and *4*) alloy I and (*2*, *5*) ZhS-6U alloy vs. time at current density of (*1*) 0.1, (*2*) 0.3, (*3*) 3, and (*4*, *5*) 10 A/cm^2 in a chloride–nitrate solution at an RDE rotation velocity of 1260 rpm.

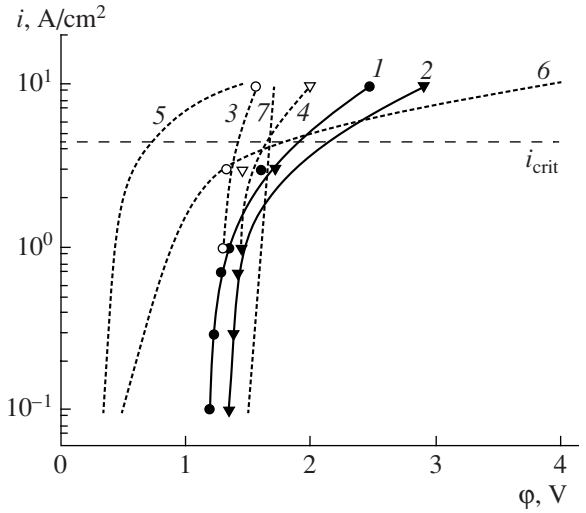

Fig. 2. Polarization curves for the anodic dissolution of (*1*) alloy I and (*2*) ZhS-6U alloy in a chloride–nitrate solution. The values of the potential adjusted for the active component of alloy I (*3*) and ZhS-6U alloy (*4*) are indicated by the open symbols. Polarization curves adjusted for the active component of (*5*) alloy I and (*6*) ZhS-6U in a 2 M NaCl electrolyte [7] and (*7*) ZhS-6U in a 2 M $NaNO_3$ electrolyte [8] are indicated by the dotted lines.

i_{crit} are observed for nitrate solutions at the same concentration of 2 M when a rotating-disc electrode (RDE) moving at a specific speed is used [8]. This may arise from the attainment of saturation in the nitrate solutions as well. As is seen from Fig. 3, the values of i_{crit} for the chloride–nitrate mixture approach the ones observed in chlorides and nitrates. However, the mechanism of the formation of the limiting condition for dissolution may be quite different. It can only be said with confidence that this centers around the retardation of transport in the solution. This process may arise from slowing down the extraction of the dissolution products, since it takes place for chloride solutions and from slowing down the supply of activating ions as well as from the retardation of the transport for solvent molecules (for further details, see, for example, [9]). These mechanisms are each liable to initiate the critical current density; the excess in the current density can radically alter the nature of the dissolution.

Specific Dissolution Rate Depending upon the Current Density and Alloy Composition

Figure 3 presents the dependence of the measured specific dissolution rate ε*C*, g/(A h), where ε is the current efficiency for a metal and *C* is the electrochemical equivalent for an alloy, upon the polarization current density for rhenium-containing alloy I; as in the case of the dissolution in NaCl and $NaNO_3$, this dependence peaks at $i = i_{crit}$. Similar dependences for this alloy are obtained upon dissolution in 2 M NaCl and 2 M $NaNO_3$ (Fig. 3). One can easily identify the two regions with $i < i_{crit}$ and $i > i_{crit}$ in these dependences. At $i < i_{crit}$, the specific dissolution rate depends on the electrolyte used and is greater in value in the case of the $NaNO_3$ solution as compared to that of NaCl and the maximum dissolution rate is observed at a preassigned current density in a mixed chloride–nitrate electrolyte. Moreover, within this region of the current density, the observed values of ε*C* in the mixed electrolyte exceeds the calculated ones

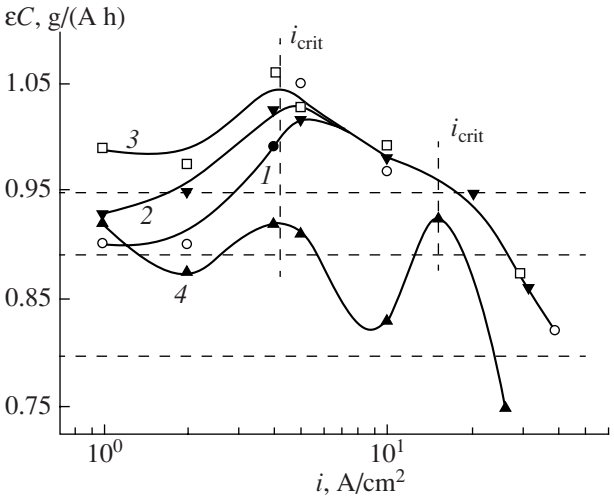

Fig. 3. Specific dissolution rate of (*1–3*) alloy I and (*4*) ZhS-6U alloy in (*1*) 2 M NaCl, (*2*) 2 M $NaNO_3$, and (*3*, *4*) chloride–nitrate solutions vs. current density at a rotational velocity of 1260 rpm and $Q = 0.023$ A h. The horizontal dotted lines are related to the values of ε*C* equal to 0.95 and 0.89 g/(A h) for alloy I and 0.89 and 0.79 g/(A h) for ZhS-6U alloy calculated at 100% of the current yield.

assuming that (i) the electrochemical dissolution mechanism alone takes place and (ii) this mechanism generates bivalent nickel and bivalent cobalt as the products of dissolution and other alloy components of the highest oxidation level (Fig. 3).

It is obvious that, together with the electrochemical dissolution, the abnormal nonelectrochemical removal of the alloy components from the surface occurs under anodic dissolution in the above-mentioned electrolyte as well as in the $NaNO_3$ solution. However, the values of εC obtained from the experiments in the mixed electrolyte exceed the ones in nitrate solution. As yet, we cannot explain this result within the limits of the proposed hypothesis on the plausible mechanisms for the nonelectrochemical removal of a metal [7, 8].

In accordance with the polarization measurements (Figs. 1 and 2), ionization of the alloy components shall follow the mechanism of transpassive dissolution, that is, at the highest oxidation level. Therefore, ionization shall proceed through the step of generation and the dissolution of surface oxide formations.

As is seen from the investigations of the chemical composition of the surface layer (see table), the oxide layers already arise even at the current density of 2 A/cm^2. However, further investigations are needed to understand why the effective valence for the dissolution of the alloy is lower than for neutral and chloride solutions.

At $i > i_{crit}$, the specific dissolution rate observed decreases with a growth in the current density and is independent of the electrolyte composition (Fig. 3). When the current density is about 20–30 A/cm^2, the measured values of εC for alloy I are below the ones calculated under the assumption on the electrochemical mechanism of dissolution.

It is obvious that, within this range of the current density, a surface is actively oxidized in keeping with the following general diagram:

$$\mathrm{Me} + n\mathrm{H_2O} \longrightarrow \mathrm{MeO}_n + 2n\mathrm{H}^+ + 2n\bar{e}\,. \qquad (1)$$

Ionization of a surface in keeping with (1) does not produce the removal of a metal from the surface. Clearly, along with the electrochemical dissolution, ionization in keeping with (1) is observed at $i > i_{crit}$; in this case, a share of the charge used up in reaction (1) grows with the current density. This results in a decline in the value of εC, that is, in the growth of the effective valence of dissolution. Therefore, a significant surface oxidation takes place, which is supported by the results presented in the table: one can make inquiries on the growth of the oxygen concentration in a surface layer upon an increase in the current density under machining.

A surface is not uniform in terms of its oxidation level due to the polymorphism of the alloy: there are regions free of oxidation and others with active oxidation (see the table and Figs. 4 and 5).

The nature of an anion leaves the oxidation unaffected. We can suppose that, in the previously indicated range of the current density, the transport of solvent molecules, that is, aqueous ones, is directed towards the surface and a decrease in its surface concentration up to the zero level (see diagram [III] in Fig. 6) turns out to be a limiting stage of the process. Consequently, the combined dissolution rate is defined by reaction (1).

Up to now, we have dealt with the peculiarities of the dissolution of rhenium-containing alloy I. As for ZhS-6U alloy, it ranks below alloy I in the measured values of εC, which is, in part, derived from its lower rated value for the electrochemical equivalent due to a greater content of chrome and tungsten in the alloy. One can see at least two values of i_{crit}; either one is coincident with the value of i_{crit} for alloy I, while the other is observed at a higher current density in the same manner as at dissolution in nitrates [8]. A number of mechanisms for the mass transport towards the surface under anodic dissolution may occur (see Fig. 6 from [9]). This makes it possible to ensure several values of i_{crit}, which is observed in the case of the ZhS-6U alloy in particular (Fig. 3). As is known, the critical conditions for the dissolution in accordance with either of three mechanisms (I, II, or III) can be attained for only one metal, as the situation requires, for instance, depending upon the bulk concentration of an activating ion (Fig. 6). For example, the dissolution of tungsten in alkalis was discussed in [1, p. 140]. The electrolyte, as well as the alloy, has the multicomponent property; therefore, the possibilities for replacing the transport mechanism at an increase in the current density under these conditions grow.

An increase in the surface temperature is of importance in the dissolution rate of an alloy. The surface temperatures of dissolution presented in Fig. 7 were calculated from the following equation [10]:

$$\Delta T_s = \frac{i(\eta + \pi)}{\alpha}, \qquad (2)$$

where ΔT_s is the excess of the surface temperature over the bulk, η is the overvoltage of the process, π is the Peltier coefficient, and α is the heat-transfer coefficient from an electrode surface.

The values presented in Fig. 7 were obtained for $\eta \gg \pi$, where the measured values of η were taken (Fig. 1); the coefficient $\alpha = 0.63$ W/(cm^2 deg) was taken for the RDE rotating velocity equal to 1260 rpm [10, p. 59]. As is seen, at $i < i_{crit}$, the surface temperature is little more than the bulk, equal to 20°C; on the contrary, at $i > i_{crit}$, a steep rise in the surface temperature is

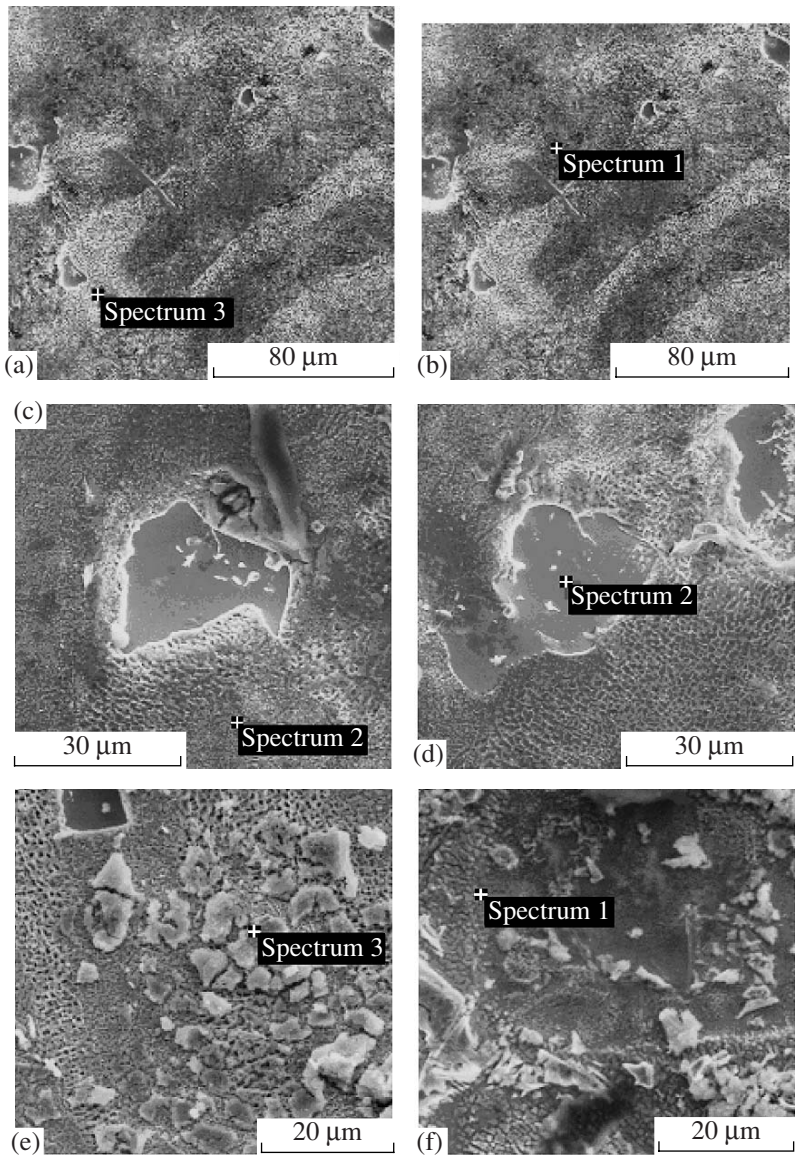

Fig. 4. Photomicrographs of the surface of alloy I obtained after anodic dissolution at 0.023 A h in a chloride–nitrate solution at an RDE rotational speed of 1260 rpm and a current density of (a, b) 2.0, (c, d) 5.0, and (e, f) 29.0 A/cm^2. The sites where the elemental composition was measured are indicated by crosses (see also table).

observed and it is close to the boiling temperature of the solution at the maximum current density used.

Change in the Composition of the Surface Layer During the Process of Machining

Alloy I. The concentrations in the surface layer after machining are given in the table, and the sites of the surface where these measurements are performed are pointed out in Fig. 4. As is seen from Figs. 4a and 4b, the oxidation of the surface occurs even at a low current density when $i < i_{crit}$. The starting concentrations of all chemical elements, with the exception of rhenium, in the surface layer are essentially independent of the machining with the dissolution at these current densities. Only rhenium significantly changes its concentration in the surface layer; in other words, the composition of the surface remains essentially the same.

A similar picture is also observed at $i \approx i_{crit}$, when i is equal to 5 A/cm^2 (Figs. 4c and 4d); however, this is only true when the average concentration over a machining surface is considered. The measurements results for a porous surface (see Fig. 4c and the results for the oxide phase in the table) are indicative of significant oxidation in the layer. This occurs due to the formation of tungsten oxides and a gain in the carbide concentration (table). As for a polished surface, tungsten oxides and carbides are absent (see Fig. 4d and the main phase in the table). On average, the proportion of an

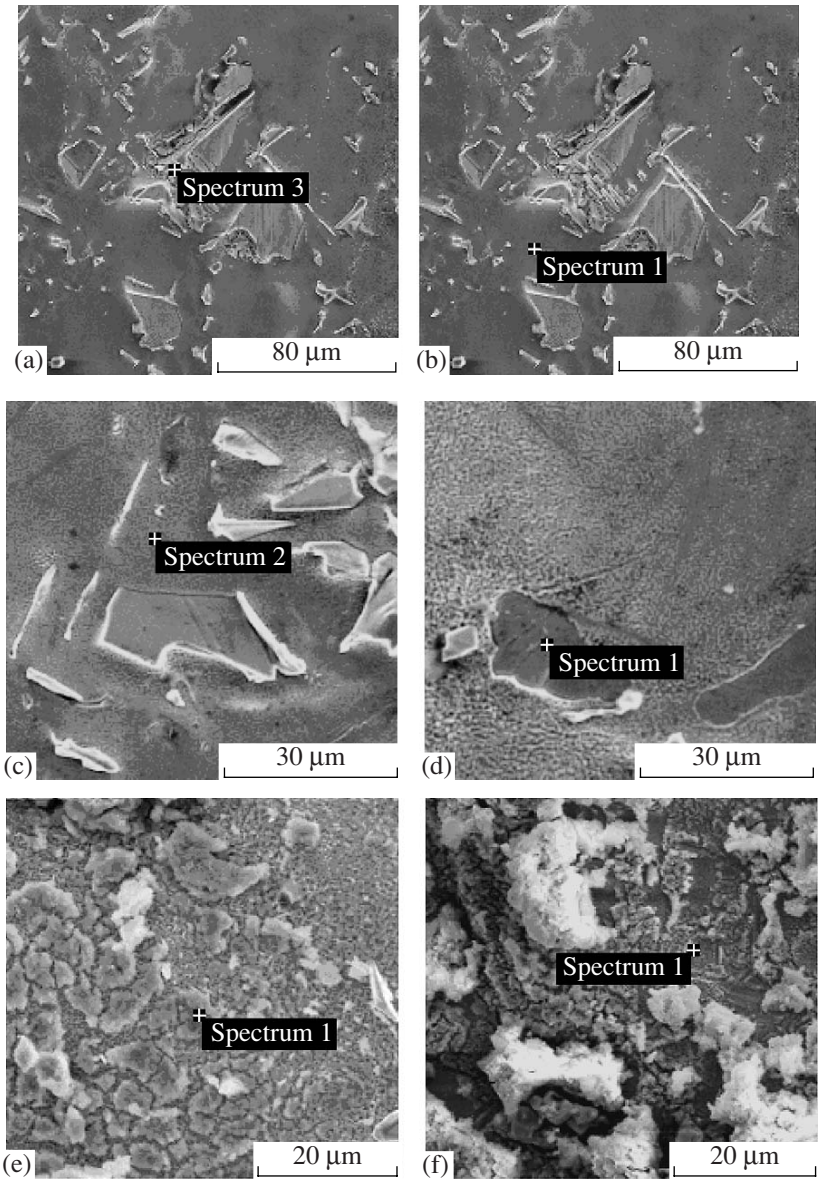

Fig. 5. Photomicrographs of the surface of the ZhS-6U alloy obtained after anodic dissolution at 0.023 A h in a chloride–nitrate solution at an RDE rotation speed of 1260 rpm and a current density of (a, b) 2.0, (c, d) 5.0, and (e, f) 25.0 A/cm^2. The sites where the elemental composition was measured are indicated by crosses (see also table).

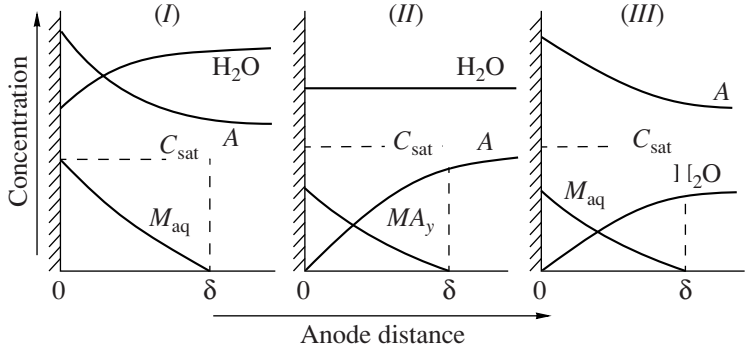

Fig. 6. Diagrams of the mass-transfer mechanisms defined by (*I*) the anodic generation of ions M_{aq}, (*II*) the introduction of an activating ion or (*III*) aqueous molecules. MA_y is related to the complex ion formed and C_{sat} is the saturation concentration.

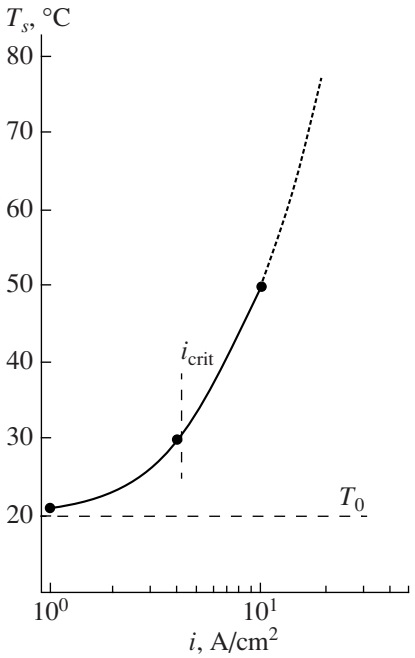

Fig. 7. Surface temperature calculated using formula (2) for alloy I in a chloride–nitrate solution vs. the current density at an RDE rotation speed of 1260 rpm. The extrapolated values of the overvoltage at $i > 10$ A/cm^2 are indicated by the dotted line.

oxidized surface does not exceed the one observed at $i < i_{crit}$ (table). This proportion shows a significant rise at $i > i_{crit}$ ($i = 29$ A/cm^2). In this case, the main phase is oxidized (Fig. 4f) and the surface formations shown in Fig. 4e are composed predominantly of tungsten oxide.

Thus, the current density $i \approx i_{crit}$ provides the optimum condition for machining. The current i_{crit} can be elevated through the intensification of the hydrodynamic regimes, which results in an equalizing of the bulk and surface concentrations of the electrolyte components and in a decrease in the surface temperature.

ZhS-6U alloy. The elevated concentration of tungsten in the alloy favorable to passivation in neutral solutions results in its essential oxidation even at low current densities. In the same manner as for alloy I, the oxidation level of its surface grows with an increase in the current density. Taking into account the changes in the surface layer after machining, one may advocate that this material is processed worse with electrochemical machining in the given electrolyte.

CONCLUSIONS

High-rate anodic dissolution of heat-resistant chromium–nickel alloys containing tungsten and rhenium was performed in a mixed chloride–nitrate electrolyte (30 g/l NaCl : 120 g/l $NaNO_3$). The electrochemical investigation shows that the alloy components are ionized in the transpassive region at a negative potential that is approximately 0.2–0.3 V above the absolute value of the potential for dissolution in an $NaNO_3$ solution. In parallel with the electrochemical dissolution, a number of mechanisms that define the combined rate of the process occur. This is also true with regards to dissolution in nitrates and chlorides.

It is shown that the critical current densities i_{crit} are in existence; if this current density is exceeded, the dissolution rate will no longer obey the nature of an anion in a solution. When $i < i_{crit}$, the dissolution rate at the given range of the current grows in the following orderly sequence: chloride, nitrate, and chloride–nitrate mixture. It was experimentally established that, at $i > i_{crit}$, the active oxidation of surface layers and a decrease in the current yield are observed at an increase on the current density. The proposal for the limiting stage of the mass-transfer process at $i > i_{crit}$ has been put forward.

The possibilities for the optimization of ECDM for the investigated materials with the use of chloride–nitrate mixtures as electrolytes are presented.

ACKNOWLEDGMENTS

We are grateful to E. Monaiko (Investigating and Testing Center of Materials, Moldova Technical University) for performing the surface analyses.

REFERENCES

1. Dikusar, A.I., Engel'gardt, G.R., Petrenko, V.I., and Petrov, Yu.N., *Elektrodnye protsessy i protsessy perenosa pri elektrokhimicheskoi razmernoi obrabotke metallov* (Electrode Mass-Transfer Processes in Electrochemical Dimensional Machining of Metals), Kishinev: Shtiintsa, 1983.
2. Davydov, A.D. and Kozak, E., *Vysokoskorostnoe elektrokhimicheskoe formoobrazovanie* (High-Rate Electrochemical Shaping), Moscow: Nauka, 1990.
3. Eliseev, Yu.S., Krymov, V.V., Mitrofanov, A.A., Saushkin, B.P., Sychkov, G.A., and Troshin, A.I., *Fiziko-khimicheskie metody obrabotki v proizvodstve gazoturbinnykh dvigatelei* (Physicochemical Methods for Processing in the Production of Gas-Turbine Engines), Saushkin, B.P., Ed., Moscow: Drofa, 2002.
4. Atanasyants, A.G., Kuznetsova, T.N., Komienko, V.A., and Kuzin, V.I., A Study of the Anodic Dissolution of Type Zh-64 and Ah-26 Alloys with Respect to Electrochemical Machining to Size, *Sov. Surf. Eng. Appl. Electrochem.*, 1985, no. 3, pp. 1–5.
5. Petrenko, V.I., Investigation into Influence of Electrode Processes on the Technological Characteristics of Electrochemical Machining of Nickel, Chrome, and Heat-resistant Alloys on Their Base, *Author's Abstract of Cand. Sci. (Techn.) Dissertation*, Novocherkassk, 1979.

6. Amirkhanova, N.A., Balmasov, A. V., Lilin, S.A, Pimenova, N.I., and Saypova, V.V., Comparative Characteristics of High-Rate Anodic Dissolution of Prospective Heat-Resistant Nickel-based Alloys, *Surf. Eng. Appl. Electrochem.*, 1997, no. 5, pp. 23–27.

7. Dikusar, A.I., Ivanenkov, I.A., Saushkin, B.P., Silkin, S.A., and Yushchenko, S.P., High-Rate Anode Dissolution of Heat-resistant Chrome–Nickel Alloys Containing Tungsten and Rhenium: I. Chloride Solutions, *Electron. Processing of Materials*, 2007, no. 1, pp. 4–15.

8. Dikusar, A.I., Ivanenkov, I.A., Saushkin, B.P., Silkin, S.A., and Yushchenko, S.P., High-Rate Anodic Dissolution of Heat-Resistant Chrome–Nickel Alloys Containing Tungsten and Rhenium: II. Nitrate Solutions, *Electron. Processing of Materials*, 2007, no. 3, pp. 4–12.

9. Landolt, D., Fundamental Aspects of Electropolishing, *Electrochim. Acta*, 1987, vol. 32, no. 1, pp. 1–11.

10. Dikusar, A.I., Engel'gardt, G.R., and Molin, A.N., *Termokineticheskie yavleniya pri vysokoskorostnykh elektrodnykh protsessakh* (Thermokinetic Phenomena in High-Rate Electrode Processes), Kishinev, 1989.

ISSN 1068-3755, Surface Engineering and Applied Electrochemistry, 2007, Vol. 43, No. 4, pp. 239–247. © Allerton Press, Inc., 2007.
Original Russian Text © Zh.I. Bobanova, D.Z. Grabco, Z. Danitse, Ya. Mirgorodskaya, A.I. Dikusar, 2007, published in Elektronnaya Obrabotka Materialov, 2007, No. 4, pp. 12–21.

ELECTRICAL SURFACE TREATMENT METHODS

Electrodeposition and Properties of an Iron–Tungsten Alloy

Zh. I. Bobanova, D. Z. Grabco, Z. Danitse, Ya. Mirgorodskaya, and A. I. Dikusar

Institute of Applied Physics, Academy of Sciences of Moldova, ul. Academiei 5, Chisinau, MD–2028 Republic of Moldova

Received January 15, 2007

Abstract—Iron–tungsten alloys were obtained from citrate electrolytes. The relation between Fe(II) and Fe(III), which permits maintaining the stability of an electrolyte as well as obtaining high-quality deposits for a long time, is revealed. The results of investigations show that the discharge of iron ions takes place from the three valent ions. It is found that the concentration of sodium tungstate in the electrolyte contributes to the codeposition of tungsten, increasing its ratio in the alloy. It is established that the current efficiency and composition of iron–tungsten coatings depend on the current density and the conditions of electrolysis. The microhardness of iron–tungsten deposits increases with an increase in the deposition temperature and depends on the tungsten content in the alloy. Investigations with an electron microscope have shown that, on the alloy surface, superficial inhomogeneous films with the content of tungsten and oxygen different from that in the deposit are formed. The obtained alloys have concentration and structure inhomogeneities.

DOI: 10.3103/S1068375507040023

INTRODUCTION

The unique physicochemical properties of tungsten and its alloys determine their application in the most important fields of modern engineering. Since there is a deficiency of tungsten in nature, the coatings of tungsten alloys exceeding pure tungsten in some parameters are given preference. Alloys of tungsten and iron-group metals are characterized by a high hardness, wear resistance, and corrosion stability. Due to their physicochemical properties, they can be considered an alternative to chromium coatings deposited from Cr(IV) solutions; at present, their wide application is limited because their environmental safety is insufficient.

A number of publications have been dedicated to the electrodeposition of alloys of tungsten and iron-group metals [1, 2]. The overwhelming majority of these works concern studying the regularities of the deposition of nickel–tungsten and cobalt–tungsten alloys, although an iron–tungsten coating is considerably cheaper than those of nickel and cobalt and is characterized by higher physicochemical properties in comparison with pure iron.

The introduction of tungsten into metal deposits allows for a significant improvement of the properties of the obtained coatings, increasing their hardness, corrosion stability, and heat resistance. It is found that tungsten-containing alloys obtained through the galvanic method exceed pure metals of the iron group in corrosion stability due to the tungsten inertia and the lower porosity of the coatings.

An iron–tungsten alloy has a higher wear resistance than pure iron. Fe–W alloys are used in both mechanics and micromechanics. These alloys are characterized by heat resistance and a high corrosion stability [3].

Iron–tungsten deposits are formed upon the electrolytic deposition of various electrolytes in the presence of sodium tungstate. Both traditional sulfate–chloride and sulfamate electrolytes and less widespread citrate electrolytes may be used for the deposition of Fe–W alloys [4]. Various existing viewpoints concerning the mechanisms of the codeposition of tungsten and iron-group metals are contradictory. Until now, there has been no unified theory of the codeposition of tungsten and iron-group metals.

A principal peculiarity of the electrodeposition of these alloys is induced codeposition. This effect consists in the fact that obtaining alloys is possible only upon the joint deposition of iron-group metals and tungsten, since tungsten deposition from aqueous solutions is impossible.

Many mechanisms of induced codeposition have been proposed up to now. Unfortunately, none of them allows us to predict the composition and, therefore, the properties of the obtained coatings on the basis of the control of the parameters, which are normally used upon the electrodeposition of coatings: the composition and concentration of the electrolytes, the current density, and the hydrodynamic conditions. This necessitates carrying out experimental research on obtaining Fe–W alloys. In the present work, the process of Fe–W alloy deposition from a citrate electrolyte was studied; the dependence of the composition and microhardness of iron–tungsten deposits on the current density and sodium tungstate content in the solution was investigated.

EXPERIMENTAL

Coatings were deposited from an electrolyte of the following composition: electrolyte no. 1: 49.6 g/l iron sulfate (heptahydrate), 71.7 g/l sodium tungstate, 150 g/l sodium citrate; electrolyte no. 2: 55.6 g/l iron sulfate (heptahydrate), 132 g/l sodium tungstate, 150 g/l sodium citrate. In all experiments, the electrolyte pH was maintained within the range of 7.4–7.8, the electrolyte temperature was held constant within 53–90°C, and the current density was 3–10 A/dm^2. Some experiments were carried out at an electrolyte temperature of 35°C.

The concentration of Fe(II) ions and the total iron concentration in the solution were determined using the photocolorimeter method, following the technique given in [5].

Stainless steel was used as the anodes.

Surface preparation before coating deposition was carried out using standard methods providing a high adhesion of the coatings with the metal base [6].

The local chemical composition was determined using the SEM and INCA Energy EDX systems. The morphology of the coatings was studied using the electron-microscopy method with the aid of a TESCAN scanning-electron microscope.

The structure of the alloys was investigated using a Dron-5 roentgen diffractometer in coradiation. The microhardness was measured with the help of a PMT-3 microhardness tester.

RESULTS AND DISCUSSION

Stability of Electrolytes upon Iron–Tungsten Alloy Deposition

Solutions prepared on the basis of iron sulfate and sodium tungstate for Fe–W alloy deposition significantly differ from the solutions used for the electrodeposition of Co–W and Ni–W alloys, because they may contain Fe(III) compounds formed as a result of Fe(II) oxidation in air. In this connection, it was necessary to study the problem of the Fe(III) compound influence on the cathode process and electrolyte stability and to determine from which of the compounds (Fe(II) or Fe(III)) the iron discharge in the alloy directly occurs.

The prepared solution of iron sulfate did not contain Fe(III); after the addition of citrate ions, the concentration of Fe(III) ions reached ~2 g/l. Apparently, this is due to the fact that, initially, Fe(III) was in the form of hydroxide and it was difficult to find; in the presence of the citrate ion, complex compounds were formed, which could be found upon analysis [7].

While keeping the electrolytes in air, the Fe(III) content in them increased to up to 4 g/l as a result of Fe(II) oxidation to Fe(III) in air. At this Fe(III) content, the deposits are not qualitative, and their reproducibility by the deposition rate is not observed. The Fe(III) concentration in the electrolyte depends on the initial Fe(II) concentration, temperature, and duration of storing.

A ration of Fe(II) and Fe(III) in the solution was found, which provided us to obtain solid deposits of the alloy during the reproducibility of the results upon the deposition rate and the tungsten content in the alloy. The transition of Fe(II) into Fe(III) may be realized due to the anodic process and the introduction of Fe(III) compounds into the solution. In these two cases, practically the same results upon the deposition rate and alloy composition are obtained. The influence of an anode current of 3–5 A/dm^2 on the electrolyte for a certain time resulted in an Fe(III) content of ~7 g/l, representing 70% of the total content of iron ions in the electrolyte. This made it possible to preserve the electrolyte stability for a long time and to obtain qualitative deposits. Alloys from electrolytes containing Fe(III) ions only were also obtained.

The completed experiments allow us to assume that the direct discharge of iron into the alloy occurs from three valent ions, not two valent ions; to obtain stable reproducible results on the yield of the current, deposition rate, and alloy composition, the content of Fe(III) compounds must be at least 60–70% of the total content of iron in the solution.

This is the principal difference between the process of deposition of tungsten alloys with iron from that of its alloys with nickel or cobalt. The latter are deposited from two valent ions.

It was found in [8] that decreasing the Fe(III) ions in the solution exceeds the iron mass in the obtained alloy deposit and it was concluded that, upon the cathode, an incomplete reduction of Fe(III) in Fe(II) takes place. Therefore, it may be assumed that, on the cathode, three parallel reactions are possible: the deposition of an iron–tungsten alloy, a hydrogen evolution, and the formation of products with an incomplete Fe(III) reduction [8].

Tungsten Content in the Alloy

The composition of an iron–tungsten alloy depends on the current density, the solution temperature, and the ratio of the concentrations of the salts of iron and tungsten. Thus, for example, as the sodium tungstate concentration in the electrolyte increases, i.e., as the Fe–W molar ratio decreases from 1 : 1 down to 1 : 2, the tungsten content in the deposited alloy increases from 27 to 44 wt % at i_k = 7 A/dm^2 at 90°C. It should be emphasized that the given values are the W relation in the "metal" component of the alloy $\left(\frac{C_W}{C_W + C_{Fe}}\right.$, where C_W is the tungsten concentration and C_{Fe} is the iron concen-

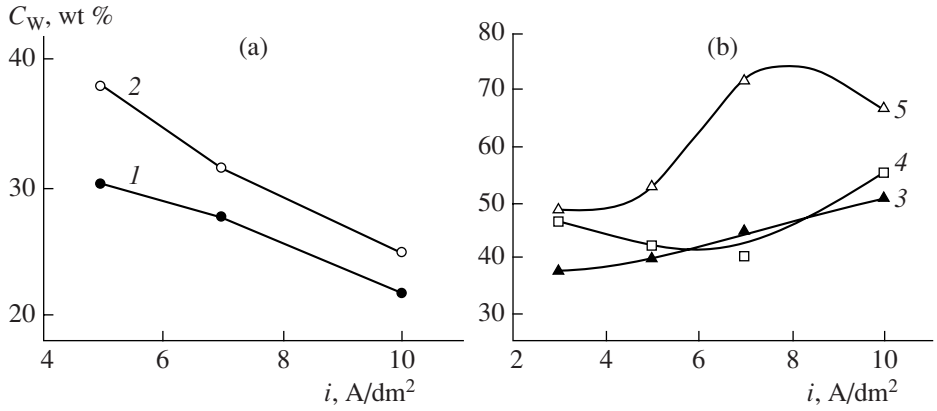

Fig. 1. Current density influence on the tungsten content in an alloy. The deposits were obtained from (a) electrolyte no. 1 with the molar ratio Fe : W = 1 : 1 at t = 90°C (curve *1*), at t = 53°C (curve *2*); (b) electrolyte no. 2 with the molar ratio Fe : W = 1 : 2 at t = 90°C (curve *3*), at t = 70°C (curve *4*); at t = 53°C (curve *5*).

tration) and they do not contain oxygen and carbon in the coating composition (see below).

It follows from the EDX analysis that, upon deposition in the electrolyte with the molar ratio Fe : W = 1 : 1 with i_k increasing from 5 to 10 A/dm^2, the tungsten percentage in the Fe–W alloy decreases from 38 to 24.5 wt % at t = 53°C (Fig.1a, curve *2* and Table 2) and from 30.3 to 21.5 wt % at t = 90°C (Table 1 and Fig. 1a, curve *1*), and the oxygen percentage increases from 0 to 6.8 wt %, respectively (Fig. 2a, curve *1* and Table 1). At the electrolyte temperature of 53°C, a film formation on the Fe–W alloy surface is observed (Fig. 3b, Spectrum *2*), wherein the oxygen content increases from 7.8 to 32.9 wt % at a current density increase from 5 to 10 A/dm^2 (Fig. 2a, curve *3* and Table 2).

When the Fe–W alloy is deposited from the electrolyte with the molar ratio Fe : W = 1 : 2 at a temperature between 53 and 90°C, a current density increase from 3 to 10 A/dm^2 is accompanied by an increase in the tungsten (Fig. 1b, curves *3–5* and Table 1) and the oxygen in the alloy (Fig. 2b, curves *4–6*); this may lead to a decrease in the crystal-phase content in the form of solid solutions and to an increase in the content of oxygen-containing amorphous deposits. The oxygen content increase in the Fe–W alloy is, apparently, caused by the adsorption of oxygen from the surroundings.

Apparently, upon the electrodeposition of iron together with tungsten, due to the alkalizing of the near-

Table 1. Chemical composition of an Fe–W alloy at various modes of electrodeposition

t, °C	i_k, A/dm^2	Elements							
		W		Fe		O		C	
		wt %	at %	wt %	at %	wt %	at %	wt %	at %
	Electrolyte no. 1 (molar ratio Fe : W = 1 : 1)								
90	5	30.3	8.7	65.5	65.5	0	0	5.5	25.4
	7	27.7	4.5	61.0	47.1	6.4	16.78	9.0	30.3
	10	21.5	5.6	71.5	66.8	6.8	16.7	7.4	25.6
	Electrolyte no. 2 (molar ratio Fe : W = 1 : 2)								
70	3	47.1	13.8	46.2	50.3	4.2	16.0	2.9	14
	5	41.6	8.4	44.3	39.4	9.4	27.9	4.0	15.8
	7	40.0	8.0	44.4	38.8	10.1	30.8	3.12	12.8
	10	54.8	6.2	24.5	17.0	21.7	48.9	4.8	15.5
90	3	37.6	8.0	53.2	43.8	5.7	16.0	9.1	31.9
	5	39.1	8.2	47.9	42.2	8.4	25.7	4.2	17.2
	7	44.2	7.7	39.3	31.8	13.5	38.0	3.7	13.8
	10	50.5	5.4	54.5	17.3	23.4	52.5	5.8	17.4

Table 2. Inhomogeneity of the composition of the surfaces obtained from electrolyte no. 1 (molar ratio Fe : W = 1 : 1)

t, °C	i_k, A/dm^2	Elements							
		W		Fe		O		C	
		wt %	at %	wt %	at %	wt %	at %	wt %	at %
53	5	Basic coating (Spectrum *1*, Fig. 3a)							
		38.0	6.2	33.8	28.1	7.8	22.1	6.1	23.3
		Surface film (Spectrum *2*, Fig. 3b)							
		20.8	4.6	68.6	57.3	4.6	13.5	5.8	22.8
53	10	Basic coating (Spectrum *1*, Fig. 3a)							
		24.5	6.4	68.9	67.2	7.4	25.0	–	–
		Surface film (Spectrum *2*, Fig. 3b)							
		27.4	6.9	43.5	22.1	32.9	58.2	4.3	17.2

cathode layer, hydroxide compounds of codeposited metals, being gel-like compounds of an amorphous type, deposit on the coating surface [9].

As the thickness of the deposits obtained at i_k = 5 A/dm^2 and t = 90°C increases from 5 to 40 μm, the content of W decreases from 49 to 34% and that of oxygen decreases from 15 to 5% (Fig. 4).The oxygen-content decrease in the thicker coating may be due to the oxygen chemical state being different from that in the thinner alloy (5–10 μm). Analysis of the oxygen spectra lines on the surface and in the depth of the coatings shows that the base peak on line 01s of the roentgen photoelectron spectrogram in the depth of cobalt–tungsten films is shifted towards the binding energy decrease [10]. This may be due to the fact that the main part of the oxygen in the depth of Fe–W films, similar to Co–W, is a component of WO_3 and tungsten.

Alloy Yield on the Current

The dependence of the yield on current (YC) on the current density for iron–tungsten alloys is shown in Fig. 5. The yield on current of the Fe–W alloy across the entire studied range of current densities for the alloys obtained from the electrolyte with the ratio Fe : W = 1 : 2 decreased from 30 to 8% (Fig. 5, curve *2*), and for the alloys obtained from the electrolytes with the ratio Fe : W = 1 : 1, the dependence of the yield on current is of an extreme character (Fig. 5, curve *1*). A change of the yield on current depending upon the current density is connected with a difference in the kinetics of the evolution of metals and hydrogen; it also depends on the alloy composition. As the W content in the alloy obtained from the electrolyte with the ratio Fe : W = 1 : 1 decreases (Fig. 5, curve *3*), the yield on current increases (Fig. 5, curve *1*). This is due to the hydrogen overstress on tungsten being lower than on iron. In this

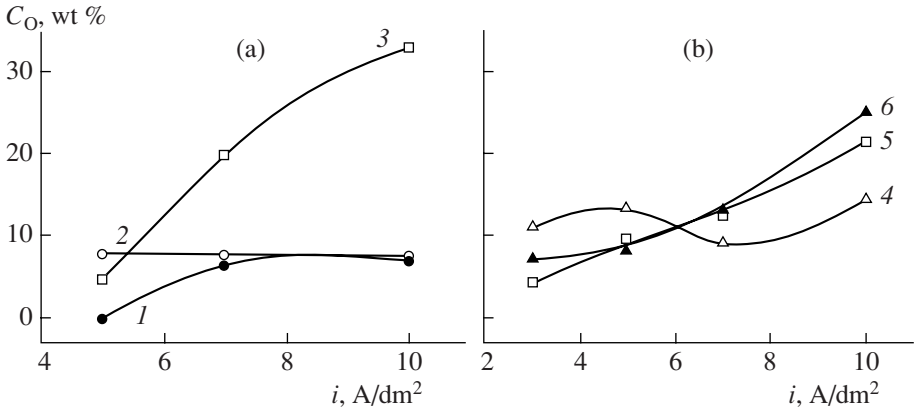

Fig. 2. Current density influence on the oxygen content in an alloy. The deposits were obtained from (a) electrolyte no. 1 with the molar ratio Fe : W = 1 : 1 at t = 90°C (curve *1*), at t = 53°C (curve *2*); at t = 53°C (curve *3*, surface film); (b) electrolyte no. 2 with the molar ratio Fe : W = 1 : 2 at t = 53°C (curve *4*), at t = 70°C (curve *5*); at t = 90°C (curve *6*).

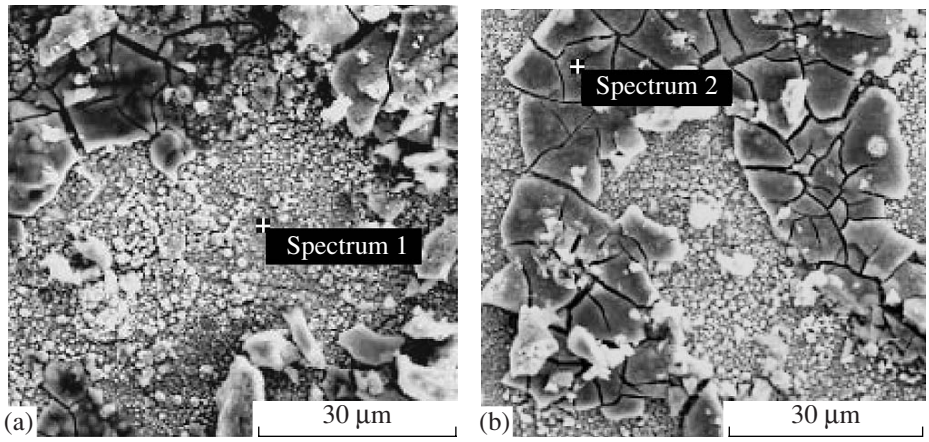

Fig. 3. Electron microphotographs of the surface of Fe–W deposits with two sectors of different composition. Electrolyte no. 1, i_k = 10 A/dm^2, t = 53°C.

case, the minimal yield on current was observed for the alloy containing 30% tungsten. In the range of high densities of the current, this somewhat decreased in comparison with the one obtained at 7 A/dm^2. The latter may be caused by the fact that, at the potential increase, the hydrogen evolution rate grows more rapidly than the rate of the alloy evolution. The evolved hydrogen influences not only yield on current of the coatings, it may directly participate in the process of W(VI) reduction. Therefore, the tungsten deposition rate depends on both the iron deposition rate and the surface concentration of active hydrogen and its possible participation in the reduction process. Furthermore, it may be assumed that the alloys contain not only a separate phase of tungsten, but that the latter may be in the form of a solid solution. The presence of oxide and hydroxide formations in the alloy is also possible [11].

It is found that an increase in the sodium tungstate content in the solution contributes to the codeposition of a refractory metal.

In Fe–W alloys obtained from an electrolyte with the molar ratio Fe : W = 1 : 2, the tungsten content in the alloy increases (Fig. 5, curve *4*) and the yield on current decreases (Fig. 5, curve *2*). The maximal yield on current corresponded to the minimal tungsten content in the alloy.

Microhardness of Deposits

The microhardness of iron–tungsten alloys is determined by the electrolysis conditions and the electrolyte composition, which is 150–450 kg/mm^2 at the current density change from 3 to 10 A/dm^2 (Figs. 6 and 7).

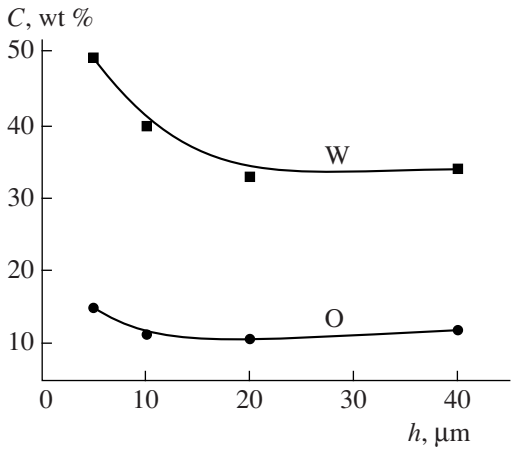

Fig. 4. Dependence of the content of tungsten and oxygen on the coating thickness. The deposits are obtained from electrolyte no. 2, t = 90°C, i_k = 5 A/dm^2.

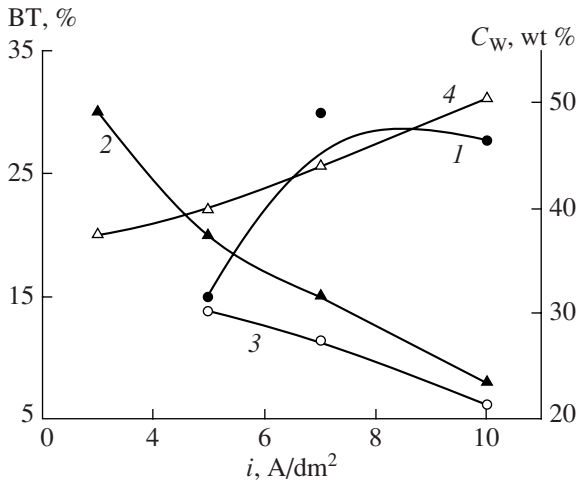

Fig. 5. Dependence of the yield on current (*1*, *2*) and tungsten content (*3*, *4*) in an iron–tungsten alloy upon deposition from electrolyte no. 1 (molar ratio Fe : W = 1 : 1) (*1*, *3*) and electrolyte no. 2 (molar ratio Fe : W = 1 : 2) (*2*, *4*), t = 90°C.

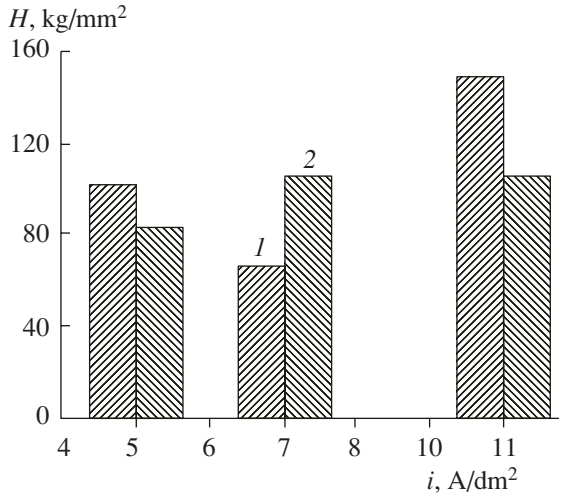

Fig. 6. Influence of the current density on the microhardness of the iron–tungsten alloy obtained from electrolyte no. 1 at $t = 53°C$.

The microhardness of the iron–tungstate alloy obtained from electrolyte no. 1 with the molar ratio Fe : W = 1 : 1 depends on the current density and the composition of the formed inhomogeneous surface films (Fig. 3). Taking into account the existence of a surface inhomogeneity, the microhardness was determined separately for a basic coating surface and for a surface film. For the basic deposit surface, the microhardness passes through the minimum and, at $i_k = 10$ A/dm^2, it is 150 kg/mm^2 (Fig. 6). For the surface film, with the current density increasing, the microhardness increases and achieves a constant value of ~106 kg/mm^2 (Fig. 6). For the deposits obtained from electrolyte no. 2 with the molar ratio Fe : W = 1 : 2, the microhardness has higher values and it oscillates within the range of ~130–440 kg/mm^2 (Fig. 7). The microhardness value gradually decreases with an increasing current density for the alloys obtained at the electrolyte temperature of 70°C (Fig. 7a, curve *2*) and it passes through the maximum at the solution temperature increasing to 90°C (Fig. 7a, curve *1*). The highest value of microhardness is observed for deposits obtained at a solution temperature increasing to 90°C (Fig. 7a, curve *1*). The highest value of microhardness is observed for those deposits obtained at $t = 90°C$; that is, for electrolytes with a high tungsten content.

The Fe–W alloy microhardness dependence on tungsten content in the alloy is found. An increase in the tungsten content in the alloy leads to an increase in the microhardness of the alloy obtained from electrolyte

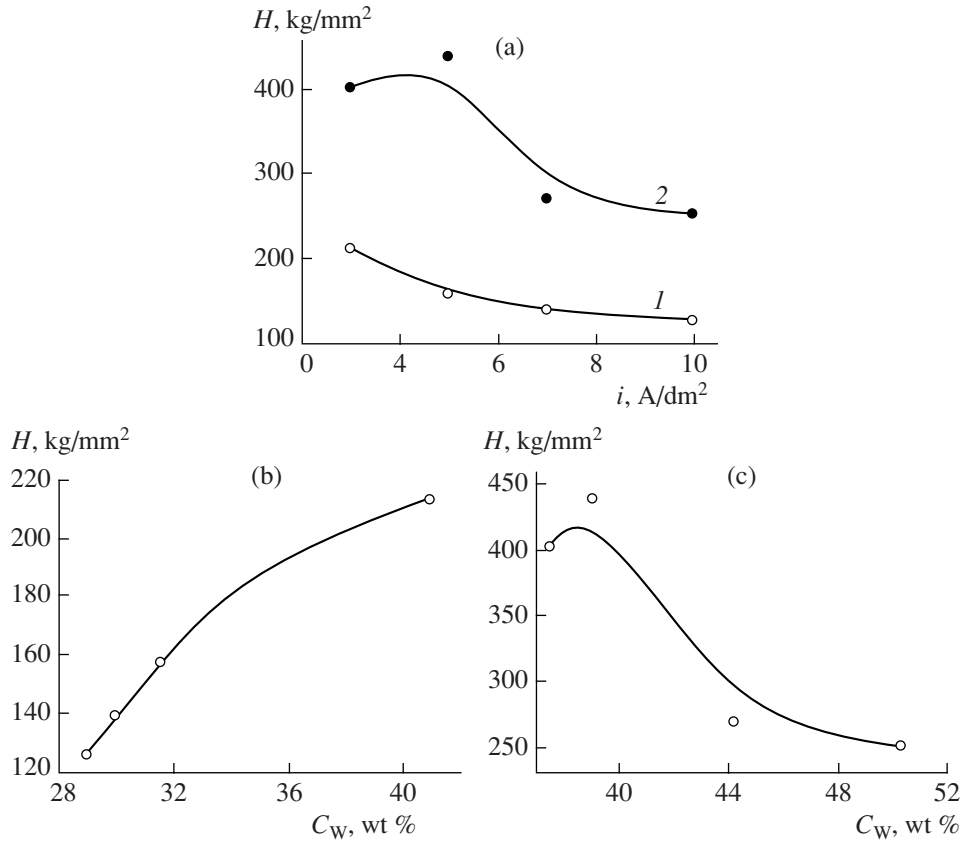

Fig. 7. Dependence of the alloy microhardness on the current density (a) and tungsten content in the alloy at temperatures 90°C (b) and 70°C (c). Electrolyte no. 2.

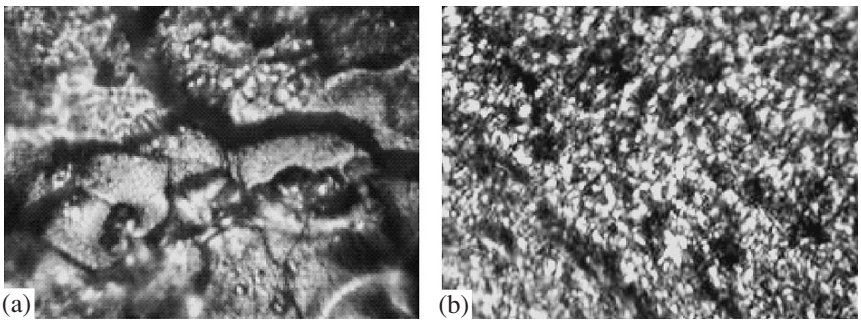

Fig. 8. Microphotographs of the optic microscopy of (a) large-grain zone (20–25 μm) and (b) small-grain zone (0.5–1.5 μm) in the alloy (electrolyte with the molar ratio Fe : W = 1 : 1). Deposition conditions: (a) $t = 35°C$, $i_k = 7$ A/dm^2; (b) $t = 70°C$, $i_k = 7$ A/dm^2.

no. 2 at a temperature of 70°C (Fig. 7b) and to appearance of the microhardness maximum for the coatings deposited at a temperature of 90°C (Fig. 7c). An appreciable increase in the microhardness was found in samples obtained at the electrolyte temperature of 90°C. Thus, the microhardness of the samples obtained at t = 35–53°C on different sectors of the deposit surface depending upon the current density varied within the range of 100–235 kg/mm^2; for the deposits obtained at $t = 90°C$, the microhardness value was 250–437 kg/mm^2. A relatively low microhardness (H_v = 100 kg/mm^2) of the electrodeposited films at the current density of 5 A/dm^2 may be connected with the fact that, at low current densities, tungsten reduction to the metal state does not occur and, therefore, a solid solution of tungsten with iron influencing the alloy microhardness is not formed. An increase in the oxygen content in the coating caused by the formation of oxide compounds can influence the microhardness by decreasing its value for the coatings obtained at high current densities (10 A/dm^2), which contain an increased content of oxygen of about 33 wt % (Fig. 2a, Table 2).

The obtained results allow us to draw the conclusion that the microhardness depends on the tungsten content in the alloy, its composition, and current density.

Alloy Surface Morphology

The electrodeposition of coatings occurs in thermodynamically nonequilibrium conditions. Upon alloy deposition, systems with characteristics of the structure are formed, which does not correspond to the thermodynamically stable state. One of the manifestations of the nonequilibrium crystallization of electrolytic alloys is the formation of oversaturated solid solutions, intermetallic compounds, and amorphous alloys. In the majority of cases, oversaturated solid solutions crystallize on the basis of the solutions containing refractory metals [12]. Nonequilibrium conditions of crystallization of these alloys determine the structural peculiarities of the electrodeposited alloys and their properties. Upon the formation of iron–tungsten deposits with a thickness of 20–30 μm, a nonuniform distribution of the alloy components over the surface is observed. The appearance of this inhomogeneity is accompanied by a change in the deposit structure.

Previously, it was noted that, for Fe–W alloys obtained upon electrodeposition from electrolytes with the molar ratio Fe : W = 1 : 1 at $t = 53°C$ and a cathodic density of 5 and 10 A/dm^2, on the surface of basic deposits, films firmly adhering to the deposit surface are found (Fig. 3b, Spectrum *2*, Table 2). The films consist of 5–10 μm blocks with a smooth surface, containing a large amount of oxygen (about 30 wt %) and are characterized by microcracking. The appearance of cracks in the films may be due to the presence of the hydroxides of deposited metals, which are located on the grain boundaries; this may lead to the weakening of the bond between them and, therefore, to cracking. The electron-microscopy study of the alloy surface base (Fig. 3a, *1*, Table 2) has shown a small-grain structure of the alloy, crystal faceting is not found, and the surface structure may be defined as cryptocrystal.

EDX analysis has shown that the composition of these two surface sectors of the basic coating and the film are inhomogeneous, although the contents of tungsten and oxygen in the deposit and in the film are different (Table 2).

In comparison with the deposit, the content of tungsten and oxygen in the film obtained from electrolyte no. 1 at i_k = A/dm^2 is lower and for the alloy obtained at i_k = 10 A/dm^2 is higher. As the tungsten content in the alloy increases, the oxygen content increases for both the deposit and the film (Table 2).

The inconsistency of the composition over the deposit surface may be due to an unequal value of the deposition potential at different points of the cathode. This leads to a nonuniform distribution of the doping component in the corresponding points of the surface and to a nonuniform development of the surface relief.

The determination of the tungsten content and the measurement of the microhardness value, with the tungsten predominance being higher in places than the averaged microhardness value across the entire deposit, confirm the inhomogeneity of the alloy composition over the deposit surface; the values for the microhard-

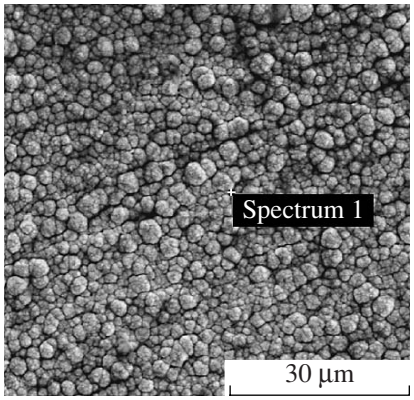

Fig. 9. Electron microphotograph of the Fe–W alloy deposited from electrolyte no. 2 at i_k = 10 A/dm^2 and t = 90°C.

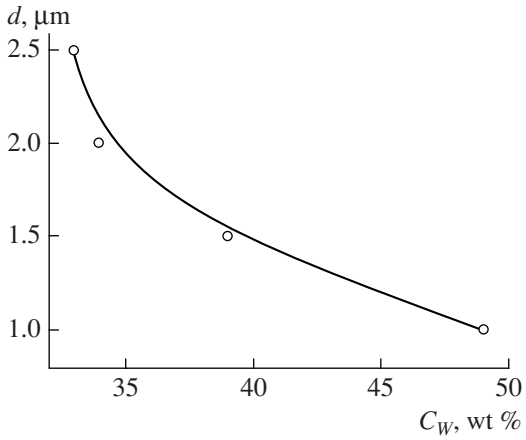

Fig. 10. Dependence of the average dimension of the alloy crystallites on the tungsten content. Electrolyte no. 2, solution temperature of 90°C.

ness of the deposits obtained in different conditions varied significantly. Thus, for iron–tungsten coatings obtained at t = 35°C and at a cathodic density of the current 3 A/dm^2, the microhardness was H_v = 110–235 kg/mm^2, and the microhardness of the coatings obtained at t = 90°C was considerably higher: H_v = 270–400 kg/mm^2.

Varying the electrolysis conditions, one can form coatings with various degrees of structure dispersion and, therefore, various properties (Figs. 8a and 8b). Upon the electrodeposition of alloys from electrolyte no. 1 (t = 35°C, i_k = 7 A/dm^2), large unequal-grain crystallites 20–25-μm in size are formed (Fig. 8a). The crystallites have a different form and, likewise, consist of separate subgrains. The alloy deposited at the electrolyte temperature 70°C has a smoother relief with crystallites of rounded or irregular forms; these are characterized by a small graininess (0.5–1.5 μm) and luster.

Electrolytic alloys iron–tungsten deposited from electrolytes with a molar ratio Fe : W = 1 : 2 at the temperature 90°C crystallize with a more homogeneous and disperse structure in comparison with pure metals obtained in similar conditions (Fig. 9). An increase in the tungsten-doping element content in the alloy influences its dispersion in the same manner as the current density increase upon the deposition of pure metals; that is, it contributes to the appearance of new centers of crystallization and the formation of small-grain deposits. An obvious correlation is observed between the dimensions of the iron–tungsten alloy crystallites determined using the microphotographs of a scanning electron microscopy and the concentration of the dissolved tungsten-doping element (Fig. 10). As the tung-

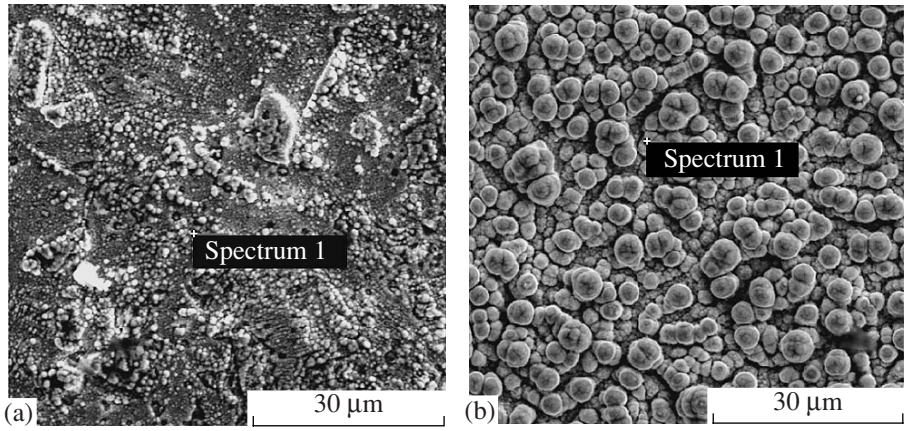

Fig. 11. Electron microphotograph of Fe–W alloys deposited from electrolyte no. 2 at temperature 90°C and i_k = 5 A/dm^2 with a coating thickness of (a) 5 and (b) 40 μm.

sten content in the alloy increases from ~30 to 50 wt %, the crystallite dimensions decrease by a factor of 2.5, leading to the dispersion of the structural elements. The observed reduction of the iron structure upon codeposition with doping refractory metals may be due to the presence in the alloys of a significant amount of impurities blocking grain growth. A similar process also takes place due to the presence in the iron–tungsten alloy deposits of adsorbed incompletely reduced compounds of tungsten; that is, the dispersion of the alloy structure occurs [13].

There is a relation between the alloy concentration inhomogeneity in thickness and its structural inhomogeneity. The tungsten-doping element concentration decreases with an increasing thickness of the obtained alloys; this may be due to the reduction of their structure. Initial layers of thickness 5 μm containing 49.4 wt % tungsten (Fig. 4) are characterized by a high dispersion (Fig. 11a). As the deposit thickness increases to 40 μm, the doping-component content in the alloy decreases to 28.4 wt % (Fig. 4) and the crystals become larger, taking on a rounded form (Fig. 11b). As the tungsten content in the alloys increases, the surface morphology changes and the crystallite dimensions decrease, i.e., the dispersion of the coatings increases. Thus, the character of change in the structure of iron–tungsten alloys is affected by their doping degree and electrolysis conditions.

CONCLUSIONS

The present results allow us to assume that, upon the deposition of iron–tungsten alloys from citrate electrolytes, the discharge of iron ions occurs from the three-valent state.

It is shown that an increase in the sodium tungstate concentration in the electrolyte contributes to the codeposition of tungsten, increasing its content in the formed alloy.

It is found that the yield on current and composition of iron–tungsten coatings depend upon the current density and electrolysis conditions. The yield on current decreases as the tungsten concentration in the coating increases.

The microhardness of iron–tungsten deposits increases with an increase in the deposition temperature and depends on the tungsten content in the alloy.

Electron-microscopy studies have shown that, on the alloy surface, surface inhomogeneous films with the content of tungsten and oxygen differing from that in the deposit are formed.

An increase in the tungsten content in the alloy contributes to the formation of small-grain deposits.

The obtained alloys are characterized by concentration and structural inhomogeneities in the thickness of the coating.

ACKNOWLEDGMENTS

This work was supported by INTAS/Moldova, project no. 05–104–7540.

REFERENCES

1. Ibrahim, M.A.M., Abd El Kehim, S.S., and Mousa, S.O., Electrodeposition of Noncrystalline Cobalt–Tungsten Alloys from Citrate Electrolyte, *J. Appl. Electrochem.*, 2003, vol. 33, pp. 627–633.
2. Yang, F.Z., Ma, Z.H., Huang, L. *et al.*, Electrodeposition and Properties of Amorphous Ni–W–B Alloy before and after Heat Treatment, *Chinese Journal of Chem.*, 2006, 24(1), pp. 114–118.
3. Gamburg, Yu.D., Zakharov, E.N., and Goryunov, G.E., Electrochemical Deposition, Structure, and Properties of Iron–Tungsten Alloy, *Elektrokhimiya*, 2001, vol. 37, no. 7, pp. 789–793.
4. Vas'ko, A.T., *Elektrokhimiya molibdena i vol'frama* (Electrochemistry of Molybdenum and Tungsten), Kiev, 1977.
5. Sharlo, G., *Metody analiticheskoi khimii. Kolichestvennyi analiz neorganicheskikh soedinenii* (Methods of Analytical Chemistry. Quantitative Analysis of Inorganic Compounds), Moscow: Khimiya, 1969, part 2.
6. Grilikhes, S.Ya., *Obezzhirivanie, travlenie i polirovanie metallov* (Cleaning, Etching, and Polishing of Metals), Leningrad, 1994.
7. Kotton, F., Uilkinson, G., *Sovremennaya neorganicheskaya khimiya* (Modern Inorganic Chemistry), Moscow: Mir, 1969.
8. Zakharov, E.N. and Gamburg, Yu.D., Some Regularities of Deposition of Iron–Tungsten Alloy from Citrate–Ammoniac Solutions, *Elektrokhimiya*, 2005, vol. 41, no. 8, pp. 1001–1004.
9. Rachinskas, V.S., Matulis, Yu.Yu., and Kharlushene, V.E., Electrolytic Magnetic Alloys Based on Cobalt. 12. New Experimental Data on Mechanism of the Processes Taking Place at Electrodeposition of Co–W Alloys, *Tr. Akad. Nauk Lit. SSR, Ser. B*, 1974, vol. 1(80), p. 55.
10. *Analiz poverkhnosti metodom Ozhe i rehtgenovskoi fotoelektronnoi spektroskopii* (Surface Analysis by Methods of Auger and Roentgen Photoelectron Spectroscopy), Briggs, D. and Sikh, M.N., Eds., Moscow: Mir, 1987.
11. Polukarpov, Yu.M. and Semenova, Z.V., Appearance of Growth Twins at Copper Electrocrystallization on the Surface of Copper Single Crystal Face (III), *Elektrokhimiya*, 1966, vol. 2, pp. 184–188.
12. Safranek, W., *The Properties of Electrodeposited Metal and Alloys. Handbook*, N.Y., 1974.
13. Povetkin, V.V., Kovenskii, I.L., and Ustinovshchikov, Yu.I., *Struktura i svoistva elektroliticheskikh splavov* (Structure and Properties of Electrolytic Alloys), Moscow: Nauka, 1992.

ISSN 1068-3755, Surface Engineering and Applied Electrochemistry, 2007, Vol. 43, No. 4, pp. 248–252. © Allerton Press, Inc., 2007.
Original Russian Text © O.M. Beregovaya, A.I. Kostrzhitskii, T.V. Cheban, 2007, published in Elektronnaya Obrabotka Materialov, 2007, No. 4, pp. 22–27.

ELECTRICAL SURFACE TREATMENT METHODS

The Influence of Oxide Films on a Steel Surface and Their Role in Adhesion Contact Formation upon the Deposition of Condensation Coatings

O. M. Beregovaya, A. I. Kostrzhitskii, and T. V. Cheban

Department of Physical and Colloid Chemistry, Odessa National Academy of Food Technologies, ul. Kanatnaya 112, Odessa, Ukraine

Received January 23, 2007

Abstract—The mechanism of contact formation, determined by the temperature mode of condensation and technological parameters of the process, is explained. Theoretical calculations and their experimental verification show that, in the case of ordinary thermovacuum deposition, the preliminary heating of steel in a vacuum in an atmosphere of residual gases determines the formation of an oxide film corresponding to the γ-Fe_2O_3 structure.

DOI: 10.3103/S1068375507040035

During all of the stages in the development of the method of evaporation and the condensation of metals [1, 2] and alloys [3, 4] in a vacuum, one of the basic problems in providing recommendations on the introduction of technologies for the metallization of low-carbon steels was the solution to two mutually exclusive problems. The first is the purification of steel surfaces from various contaminations which prevent the formation of a strong adhesion contact. The second problem is the presence of oxide films on the surface and determining the optimal modes of treatment, taking into account the possible additional formation of oxides during the treatment process, which, according to numerous authors, generally reduce the adhesion contact strength [5].

Depending upon the constructive solution to the practical realization of the process of obtaining condensation coatings for various functional applications, for the preliminary preparation of a steel surface with the purpose of purifying and obtaining a strong adhesion contact, thermal heating in a vacuum [1–3] and steel-surface treatment in the plasma of a glow discharge are the most frequently used [4, 6–8]. During thermal heating of steel samples in an atmosphere of residual gases, an interaction between the substrate material and residual oxygen takes place on the steel surface. As a result, in addition to processes of surface purification from macrocontaminations, the formation of additional oxide layers is observed. The oxide thickness, its structure, phase composition, and some electrophysical properties are determined; they depend on the steel-heating temperature and the time of heating. The authors of [9, 10], analyzing one possible mechanism of adhesion contact formation, have assumed that steel heating in an atmosphere of residual gases may be accompanied by two competing processes on the surface: the additional oxidation of iron upon interaction with oxygen on the external "surface film–vacuum" boundary and the oxide film reduction by carbon dissolved in iron on the adjacent "oxide–basic metal" surface. An important parameter in the determination of a preferential process is temperature T, whereby its absolute value ultimately determines the increase or decrease in the oxide thickness.

If the steel in undoped or low-doped, the oxide film formation process is reduced to pure iron oxidation; the kinetics of this process may be estimated using the known equations [11] and data on the physicochemical properties of oxides [12]:

$$\alpha = 8.95 \times 10^6 \sqrt{\tau} \exp\left(-\frac{16500}{T}\right), \qquad (1)$$

where τ is the oxidation time and α is the iron oxide thickness.

Calculations using formula (1) illustrate the oxide kinetics (Table 1) assuming that the oxidation rate constant K changes by the parabolic law [11].

In vacuum metallization, especially in the application of thermovacuum deposition on a thermovacuum substrate, the technological stage of the steel surface preparation by heating necessitates estimating the oxide formation kinetics not at a fixed temperature T, but at the steel heating from the initial temperature T_1,

Table 1. Oxide oxidation rate

T, K	473	573	673	773	873
$\frac{\alpha}{\sqrt{\tau}}$, nm/s$^{1/2}$	0.24	4.42	40.3	216.5	714.0

generally being room temperature to the temperature of the coating deposition beginning at T_2. It should be taken into account that the deposition process begins immediately after achieving temperature T_2; additional storing of the samples at temperature T_2 before deposition begins is not required [2, 3].

Let us suppose that the thermal heating of a steel (iron) surface from T_1 to T_2 occurs by the linear law

$$T = T_1 + \frac{T_2 - T_1}{\tau_1}, \quad (2)$$

where τ_1 is the time of heating from T_1 to T_2.

When calculating the oxide thickness growth regularities upon heating in a vacuum [10], the kinetics of the oxide growth on iron upon heating up to temperature T_2 with various rates was calculated. The results are given in Table 2 ($T_1 \approx 293$ K). Experimental analysis (Fig. 1) has shown that the theoretical predictions (solid curve) and experimental (dots) results match exactly, which matches results from the literature [10].

It should be noted that the regularities given in Tables 1 and 2 and in Fig. 1 assume an excess oxygen content in the residual atmosphere contacting the heated surface ($p > 1.013 \times 10^3$–1.013×10^5 Pa). The processes of the steel surface preliminary preparation and deposition of condensation coatings occur at significantly lower pressures of about 10^{-2}–10^{-4} Pa. A limited content of oxygen in the residual atmosphere considerably influences the oxidation kinetics and, in particular, the limiting thickness of the oxide film which may form during the process of steel heating in a vacuum. Taking into account that the normal oxygen pressure in an atmosphere and in a vacuum chamber at various degrees of pressure does not change and remains constant at 21% p_0 (where p_0 is he total pressure of the residual atmosphere), let us estimate the limiting thickness of the iron oxide film α_{lim}, which may be formed on the sample surface of the square S which is heated up to temperature T in a vacuum chamber of volume V:

$$\alpha_{lim} = \frac{0.21 V \mu}{2RT\rho S} p. \quad (3)$$

Here, μ is the oxide molecular weight, ρ is its density, α is the number of oxygen molecules required for the formation of one molecule of oxide, and p is the pressure of residual gases (Pa).

Calculations of α_{lim} assuming that oxidation upon thermal heating in a vacuum results in the formation of γ-Fe_2O_3 oxide [3, 4, 13–16] are given in Table 3 ($V = 2 \times 10^{-2}$ m^3, $S = 10^{-4}$ m^2, and $T = 298$ K).

Analysis of the calculations allows us to make the following conclusions: A decrease of pressure in the vacuum chamber can considerably influence the character of the dependence $\alpha = f(\tau)$ only when the thickness of the oxide formed at a normal atmospheric pressure exceeds the values of α_{lim} for a given pressure. For example, at $T \approx 293$ K, the oxide thickness on iron does not exceed 5.0 nm [11]; according to the data in Table 3, the oxidation rate may only decrease at the residual gas pressure $p < 10^{-2}$ Pa. At $T \approx 573$–673 K, the oxide thickness on iron achieves 20 nm and, therefore, a change in the oxidation kinetics should be expected beginning from the pressures $p \approx (1$–$2) \times 10^{-1}$ Pa. This conclusion is in a good agreement with available data [1, 3, 13].

Table 2. Kinetics of oxide growth on iron

T_2, K	473	573	673	723	773	823	873
$\frac{\alpha}{\sqrt{\tau}}$, nm/s$^{1/2}$	0.14	1.16	12.0	24.0	36.0	101.0	184

Table 3. Calculations of α_{lim}

P, Pa	5×10^{-1}	1×10^{-1}	5×10^{-2}	1×10^{-2}
α_{lim}, nm	250.0	50.0	25.0	5.0

Beginning from a certain substrate temperature, the processes of oxide film reduction using carbon dissolved in the substrate play an appreciable role. This process is competitive against the oxidation process, and the total result of both processes will be expressed either in an increasing or decreasing oxide thickness with time. Experimental analysis of the regularities of the kinetics of the oxide film reduction on an iron surface with the application of the technique from [10] has shown (Fig. 2) that a decrease of the oxide thickness α upon annealing in an inert gas atmosphere occurs in accordance with the linear law. The rates of film reduction during annealing at two temperatures $T_1 = 623$ K and $T_2 = 673$ K are determined by graphic differentiation of the dependence $\alpha f(\tau)$. According to the calculations for curves *1* and *2* (Fig. 2), the reduction rates are equal to $V_1 = 1.97 \times 10^{-2}$ nm/s and $V_2 = 0.24 \times 10^{-2}$ nm/s, respectively. The rates of the chemical reaction corre-

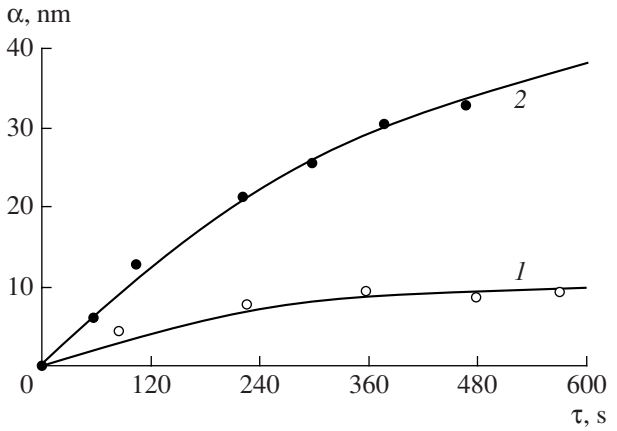

Fig. 1. Dependence of the oxide film thickness change on the time of heating τ_1 (formula (2)) from $T_1 = 293$ K to $T_2 = 573$ K (*1*) and to $T_2 = 673$ K (*2*).

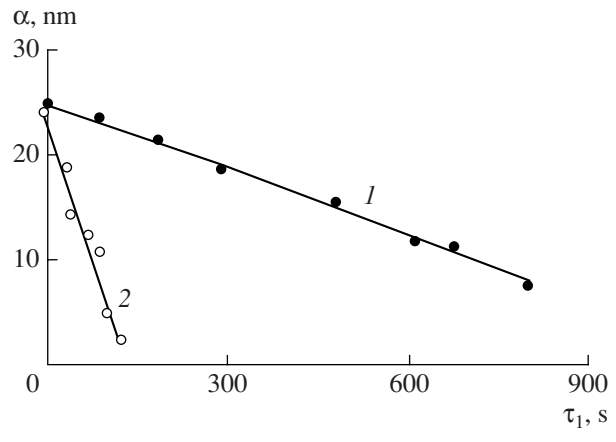

Fig. 2. Change in the oxide film thickness on steel upon annealing in an argon atmosphere at 623 K (*1*) and at 673 K (*2*).

sponding to the calculated values correspond to the known equation of the chemical reaction kinetics

$$\vartheta = KC_{\mathrm{MeO}}C_{\mathrm{C}}, \quad (4)$$

where C_{MeO} and C_{C} are the concentrations of oxide and carbon on the adjacent "metal–oxide" boundary at moment $\tau = 0$ (initial concentrations); K is the constant of the reduction reaction rate, whereby its temperature dependence is determined by the Arrhenius equation

$$K = k_0 e^{-\frac{B}{RT}}, \quad (5)$$

Here, parameter B denotes the reduction process activation energy. The experimentally found linear character of the dependence $\alpha = f(\tau)$ (Fig.2) allows us to assume that the carbon concentration in the reaction zone on the adjacent "metal–oxide" boundary is either constant or changes insignificantly, i.e., $C_{\mathrm{C}} \approx 1 = \mathrm{const}$. Then, formula (4), with a sufficient degree of certainty, may be rewritten in the form

$$\vartheta = K_1 \exp\left(-\frac{B}{RT}\right). \quad (6)$$

Using the above given values for the reduction reaction rates at two temperatures, it is possible to calculate the values of K_1 and B: $K_1 \approx 8.5 \times 10^{12}$ nm/s, $B \approx 175 \times 10^3$ J/mol. According to these data, the rate of the oxide film reduction reaction on iron at various temperatures was calculated (Table 4).

Table 4. Rates of reduction upon substrate heating up to the temperatures 673–723 K

T, K	573	623	673	723	773
ϑ, nm/s	10^{-3}	2×10^{-2}	0.24	2.13	13.77

A comparison of the rates of oxidation (Table 1) and reduction (Table 4) shows that, upon substrate heating up to the temperatures 673–723 K, the oxidation process prevails: an increase of the oxide film thickness is observed. At temperatures 673–873 K and above, the prevailing reaction is oxide reduction, and a sharp decrease in the oxide thickness with time up to its complete disappearance is observed. In the metallization of low-carbon steels [3, 4, 6, 8], the recommended temperature modes of deposition of various coatings correspond to the complete elimination of surface oxide films and to the transition of the adhesion contact formation in the "coating–substrate" system from the Van der Waals mechanism [9] to the more reliable, e.g., diffusion, mechanism [3, 5]. The advantages of this mechanism of adhesion contact formation compared with others are analyzed in [5].

Thus, these completed experiments and the proposed interpretation of the regularities of the oxidation–reduction processes in the "substrate–oxide" system upon heating in a vacuum allow us to make some generalizations regarding the prediction of the expected mechanism of adhesion contact formation upon the deposition of various coatings on low-doped steel. At condensation temperatures below 473 K, practically none of the metals used for coatings, e.g., Al, Cr, Ti, Cu, Cd, ferroalloys, etc., forms an appreciable adhesion with the substrate [1–4, 6, 8]. Obtaining metal products with qualitative adhesion to the protective coatings at low temperatures is possible only when, instead of the usual vacuum technology, the ion–plasma technology is applied [4, 6, 7]. In the first place, this is connected with the fact that one of the possible mechanisms of adhesion contact formation is the diffusion mechanism [4, 5, 8]; the conditions for its realization are analyzed in detail in [5, 6, 17].

In the case of the realization of the chemical mechanism of the adhesion contact formation in the "substrate–coating" system, the thermodynamics of the process plays an important role. The energy aspect of the adhesion contact formation upon the deposition of pure metals on an oxidized surface may be predicted a priori by calculating the isobar–isothermal potential change ΔG in the process of possible chemical reactions. For some coatings of pure metals most frequently used in a protective role [2, 4, 6], the analysis of the calculated values of ΔG in the temperature range 298–623 K (Table 5) allows us to make the following conclusions.

The classical approach to the analysis of the processes of the metal–vapor interaction with the oxidized substrate shows that the chemical interaction with iron oxide is realized for Al, Ti, and Cr, whereas for Cu and Cd this process is energetically forbidden. Experimental data on the regularities of the adhesion contact formation [1, 2, 6, 8] show that none of the metals given in Table 5 forms a strong bond with the steel surface until temperatures 623–673 K are reached, with the exception of aluminum [2]. This discrepancy between the

Table 5. Calculations of the change in ΔG by standard reactions

Possible equation of the chemical reaction taking into account the oxide phase composition [2, 3, 8, 14]	ΔG change ($\Delta G \times 10^{-6}$, J/mol) at condensation temperatures (K)		
	298	473	623
$8Al + 3Fe_3O_4 \longrightarrow 9Fe + 4Al_2O_3$	–3248	–3148	–3116
$2Al + Fe_2O_3 \longrightarrow 2Fe + Al_2O_3$	–840	–815	–802
$8Ti + 3Fe_3O_4 \longrightarrow 9Fe + 4Ti_2O_3$	–2664	–2653	–2634
$2Ti + Fe_2O_3 \longrightarrow 2Fe + Ti_2O_3$	–694	–690	–687
$8Cr + 3Fe_3O_4 \longrightarrow 9Fe + 4Cr_2O_3$	–1108	–1141	–1135
$2Cr + Fe_2O_3 \longrightarrow 2Fe + Cr_2O_3$	–305	–314	–308
$4Cd + Fe_3O_4 \longrightarrow 3Fe + 4CdO$	100	88	106
$3Cd + Fe_2O_3 \longrightarrow 2Fe + 3CdO$	46	38	56
$4Cu + Fe_3O_4 \longrightarrow 3Fe + 4CuO$	514	489	500
$3Cu + Fe_2O_3 \longrightarrow 2Fe + 3CuO$	355	338	351

calculations and experiment is explained by two factors. First, in the process of vacuum metallization using standard technology [2, 3], there is a probability of partial oxidation of the evaporated material atoms due to the interaction with oxygen molecules of the residual atmosphere. Secondly, in the calculations using the standard reactions (Table 5), the probability of the presence of adsorbed gases and water vapors on the metallized steel surface is not taken into account. The elimination of moisture vapors and adsorbed gases is possible either by thermal heating of the substrate up to the temperature 623–673 K [2, 4] or by the electrophysical purification of the substrate in a glow-discharge plasma [1, 4, 6, 8] directly before the beginning of deposition.

Regarding the probable oxidation of the evaporated metal vapors in the residual gas atmosphere, according to [14], this process can be considered significant, especially at the initial stages of the condensation process, when the first 5–10 monolayers of the condensate are formed. The formation of oxides in the vapor phase leads to the following: The adhesion contact by the chemical mechanism [5] occurs not by the reactions in Table 5, but between the iron oxide (substrate) and the evaporated material oxide; that is, the coating in the presence of TiO_2, Cr_2O_3, Al_2O_3, etc. The chemical interaction in these systems is realized in practice at temperatures above 1170 K. The only exception is Al. Experiments on the character of the temperature dependence of Al adhesion to Fe have shown [14] that, already at condensation temperatures 420–470 K, a strong adhesion contact is formed, and its phase composition corresponds to the complex oxide $FeO \cdot Al_2O_3$.

CONCLUSION

1. The presence of oxide films on an iron surface is not an obstacle to the formation of qualitative protective coatings being strongly bound to the substrate. The mechanism of the contact formation is chemical, and it is determined by the condensation temperature mode and the process of the technological parameters.

2. Theoretical calculations and their experimental analysis show that, in the case of normal thermovacuum deposition, a preliminary heating of the steel in a vacuum in a residual gas atmosphere determines the formation of an oxide film corresponding to the γ-Fe_2O_3 structure. The oxide of this modification is optimal from the viewpoint of the adhesion contact formation using the chemical mechanism.

3. During the process of steel heat treatment in an atmosphere of residual gases of a vacuum chamber, two processes proceed simultaneously: steel oxidation and oxide reduction by the carbon of the substrate. The predominance of one process over the other is determined by the ratio of the substrate temperature to the pressure of the residual gases.

REFERENCES

1. Roikh, I.L. and Koltunova, L.N., *Zashchitnye vakuumnye pokrytiya na stali* (Protection Vacuum Coatings on Steel), Moscow: Mashinostroenie, 1971.
2. Roikh, I.L., Koltunova, L.N., and Fedosov, S.N., *Nanesenie zashchitnykh pokrytii v vakuume* (Deposition of Protection Coatings in Vacuum), Moscow: Mashinostroenie, 1976.
3. Kostrzhitskii, A.I. and Lebedinskii, O.V., *Mnogokomponentnye vakuumnye pokrytiya* (Multicomponent Vacuum Coatings), Moscow: Mashinostroenie, 1987.
4. Kostrzhitskii, A.I., Methods of Obtaining and Properties of Corrosion–Stable Vacuum Multicomponent Films and Coatings, *Extended Abstract of Doctoral (Eng.) Dissertation*, Moscow: Karpov NIFKhI, 1988, p. 37.
5. Kostrzhitskii, A.I., Kalinkov, A.Yu., and Naumova, E.N., On the Problem of Condensation Coating Adhesion to Metal Substrates, *Kholodil'na Tekhnika i Tekhnologiya*, 2002, no. 1 (75), pp. 47–55.
6. Lebedinskii, O.V., Study of Technology of Deposition and Protection Properties of Ion Coatings of Copper and Iron–Chromium Alloys on Steel, *Extended Abstract of Cand. Sci. (Eng.) Dissertation*, Moscow: Karpov NIFKhI, 1980, p. 27.
7. Roikh, I.L., Koltunova, L.N., and Lebedinskii, O.V., Protection Coatings Obtained by the Method of Ion Deposition in Vacuum, *Zashchita Metallov*, 1977, vol.13, no. 6, pp. 649–661.
8. Kostrzhitskii, A.I., Karpov, V.F., Kabanchenko, M.P. and Solov'eva, O.N., *Spravochnik operatora ustanovok po naneseniyu pokrytii v vakuume* (Handbook of Operator of Installations for Coating Deposition in Vacuum), Moscow: Mashinostroenie, 1991.
9. Roikh, I.L. and Fainshtein, A.I., Oxide Film Influence of Value of the Van der Waals Interaction of Metals, *Izv. Akad. Nauk SSSR, Ser. Metally*, 1974, no. 2, pp. 230–234.

10. Fainshtein, A.I. and Kabanchenko, M.P., Oxidation–Reduction Processes on Steel Surface under Heating in Vacuum, *Izv. Akad. Nauk SSSR, Ser. Metally*, 1977, no. 4, pp. 183–188.
11. Kubashevskii, O. and Gopkins, B., *Okislenie metallov i splavov* (Oxidation of Metals and Alloys), Moscow: Metallurgiya, 1965.
12. *Fiziko–khimicheskie svoistva okislov. Spravochnik* (Physical–Chemical Properties of Oxides. Handbook), Moscow: Metallurgiya, 1969.
13. Beloritskaya, E.L., Rafalovich, D.M., Roikh, I.L., and Rybin, B.S., Influence of Oxide Films on Vacuum Deposit Adhesion to Steel, *Fiz. Khim. Obrab. Mater.*, 1968, no. 1, pp. 31–34.
14. Fainshtein, A.I., Roikh, I.L., and Litovchenko, N.A., On Chemical Interaction of Films Obtained by Method of Metal Evaporation in Vacuum, with Oxide on Substrate, *Zh. Fiz. Khim.*, 1979, vol. 52, no. 5, pp. 1079–1082.
15. Fainshtein, A.I. and Litovchenko, N.A., Change of Properties of Oxide Film on Iron in Growth Process, *Zh. Fiz. Khim.*, 1980, vol. 54, no. 3, pp. 801–803.
16. Fainshtein, A.I., Study of Electric Conductivity of Thin Oxide Films on Iron Surface, *Izv. Akad. Nauk SSSR, Met.*, 1981, no. 5, pp. 168–171.
17. Roikh, I.L., Karpov, V.F., and Pustotina, S.R., Diffusion Processes at Formation of Protection Vacuum Coatings on Magnesium Alloys, *Zashchita Metallov*, 1979, no. 1, pp. 129–132.

ISSN 1068-3755, Surface Engineering and Applied Electrochemistry, 2007, Vol. 43, No. 4, pp. 253–256. © Allerton Press, Inc., 2007.
Original Russian Text © F.P. Grosu, M.K. Bologa, 2007, published in Elektronnaya Obrabotka Materialov, 2007, No. 4, pp. 28–33.

ELECTRICAL PROCESSES IN ENGINEERING AND CHEMISTRY

The Structure of a Space Charge in Low Conductive Liquids in a Plane-Parallel Capacitor

F. P. Grosu[a] and M. K. Bologa[b]

[a] *Institute of Applied Physics, Academy of Sciences of Moldova, ul. Academiei 5, Chisinau, MD-2028 Republic of Moldova*
[b] *State Agrarian University of Moldova, ul. Mirchesht' 44, Chisinau, MD-2049 Republic of Moldova*

Received May 28, 2007

Abstract—The generation of a space charge in low conductive liquids under the influence of an external electrostatic field is considered on the basis of the Nernst–Planck equations. It is shown that, in the case of symmetric conditions for the same electric parameters of positive and negative charge carriers, only heterocharge and homocharge distributions of the field are possible, whereas bipolar structures cannot exist. Possible ways of searching for such structures are proposed.

DOI: 10.3103/S1068375507040047

It is well known that, under the action of an external electrostatic field, a low conductive (dielectric) liquid loses its local electrical neutrality [1] and, in a plane-parallel capacitor, for example, a certain charge distribution forms with the nonzero space charge density $\rho(x) \neq 0$; the x coordinate is determined in the direction perpendicular to the layer of the liquid. Two types of space electrization in liquids can be classically distinguished according to the $\rho(x)$ distribution: a heterocharge electrization, when the semilayers acquire a charge of the opposite sign with respect to adjacent electrodes; and a homocharge electrization, when the adjacent to the electrode layers acquires a charge of the same sign [2]. In both cases, a monopolar structure of the space charge manifests itself, that is, within each semilayer in the interelectrode gap, the sign of the charge is constant; hence, the field strength also changes monotonously within the semilayers.

However, so-called bipolar structures were found experimentally [3], where a maximum appears near the electrodes in the distribution of the field strength $E(x)$, which provides evidence that double structures form within semilayers: the layer adjacent to the electrode bears a charge of the same sign, and, further, it transforms into the layer with the opposite sign. Such a structure may be defined as a bipolar homocharged structure. According to experiments [4], bipolar heterostructures with minima of the field strength near the electrodes are also possible, although less probable.

Alongside the interpretation of bipolar homostructures [3–5], the authors of [6, 7] have also attempted to provide theoretical explanation. In particular, in [6], a hypothesis was put forward that, with an increase in the voltage across the layer and the field strength on the electrode surface, because of heteropolarization, a microbreakdown in the near-electrode (Debye–Huckel) layer and its homocharging can occur at some critical value of the field strength E_{cr}. Here, the main assumption was that the electric conductivity of the liquid is constant (σ = const). Therefore, one can only expect a qualitative explanation of the observed distributions $E(x)$ [4]. Furthermore, the authors of [7] rejected this hypothesis and tried to find an exact solution to the Nernst–Planck equations (for the symmetrical case, when $k_{\pm} \equiv k$; $D_{\pm} \equiv D$):

$$\begin{cases} j_+ = k\rho_+ E - D\rho_+'; \quad \rho = \rho_+ - \rho_-; \\ j_- = k\rho_- E + D\rho_-'; \quad \sigma = k(\rho_+ + \rho_-); \\ j_+' = 0; \quad j_-' = 0; \quad \rho = \varepsilon E'; \quad j = j_+ + j_- = \text{const}, \end{cases} \tag{1}$$

where conventional notations are used, and the signs $\pm$ refer to positive and negative charge carriers. Here, we assume that j_+ = const and j_- = const are specified and ρ_+, ρ_-, ρ, σ, E are unknown values.

In addition to the assumption concerning the symmetry of the parameters of charge carriers $k_+ = k_- \equiv k$ and $D_+ = D_- \equiv D$, the most significant in the given problem is an assumption related to the conservation of partial currents in the form $\operatorname{div} \vec{j}_+ = 0$ and $\operatorname{div} \vec{j}_- = 0$. The latter, however, often occurs in the electrochemistry of liquid solutions, where they seem even less reasonable because of large concentrations of charge carriers.

In [7], Eq. (1) was reduced to one dimensionless Penleve equation [8] similarly to that in [1, 4]:

$$\eta'' = \pi_0 \eta^3 + \pi_1(1 + \pi_2(1 - \xi))\eta - \pi_3, \tag{2}$$

where the following notations for the dimensionless complexes are introduced:

$$\pi_0 = \left(\frac{lkE_0}{\sqrt{2}D}\right)^2; \quad \pi_1 \equiv \frac{l^2}{\tau_* D}; \quad \pi_2 \equiv \frac{lk\delta}{\sigma_* D}; \quad \pi_3 \equiv \frac{jl^3}{\varepsilon D E_0}, \tag{3}$$

and

$$\tau_* \equiv \varepsilon/\sigma_*; \quad \delta \equiv j_+ - j_-; \quad \sigma_* \equiv \sigma_0 - \frac{\varepsilon k^2 E_0^2}{2D}; \qquad \eta \equiv \frac{E}{E_0}; \quad \xi = \frac{x}{l}; \tag{4}$$

where l is the width of the semilayer, and x is counted from the left (positive) capacitor plate.

It should be noted here, that for a completely symmetrical problem, where $j_+ = j_- \Rightarrow \delta = 0 \Rightarrow \pi_2 = 0$, the initial conditions for Eq. (2) are obvious:

$$E(x)|_{x=l} = E_0; \; E'(x)|_{x=l} = 0 \Rightarrow \eta(1) = \eta_0 = 1; \quad \eta'(1) = \eta'_0 = 0. \tag{5}$$

When $j_+ \neq j_-$, that is, $\pi_2 \neq 0$, the distance from the left plate to the plane, where $\varphi = 0$ or $\rho = 0$, may be taken as the length scale l, instead of the distance from the left plate to the center of the layer. Then, conditions (5) remain valid; however, in the case where $\pi_2 = 0$, instead of Eq. (2), we get

$$\eta'' = \pi_0\eta^3 + \pi_1\eta - \pi_3. \tag{6}$$

This equation for conditions (5) allows the first integration, which gives the result

$$\eta'^2 = \frac{\pi_0}{2}[(\eta^2 + a)(\eta + 1) - b^2](\eta - 1), \tag{7}$$

where

$$b^2 \equiv \frac{4\pi_3}{\pi_0}; \quad a \equiv \frac{2\pi_1}{\pi_0} + 1, \tag{8}$$

and where a and π_1 may be both positive or negative.

It was stated in [7] that the condition of the existence of bipolar solutions to equations (6) and (7) is that each of them should have a positive root; these are satisfied (the Cartesian rule). This allowed the authors to conclude that bipolar structures are possible.

The present paper continues from [7], and as we envisaged earlier, relates to the final solution to Eq. (7). However, to reduce this equation to a tabulated elliptic integral, we have to find a positive root of the cubic equation in the square brackets. Denoting this root as $\alpha > 0$ and substituting it into the square brackets in (7), we, then, set the expression in brackets equal to zero and obtain

$$b^2 = (\alpha^2 + a)(\alpha + 1) \geq 0. \tag{9}$$

Then, we substitute the right-hand side of (9) into (7), divide the obtained expression by $\eta - \alpha$, and find the sought factorial expansion

$$\eta'^2 = \frac{\pi_0}{2}[\eta^2 + (\alpha + 1)\eta + \alpha(\alpha + 1) + a] \times (\eta - \alpha)(\eta - 1). \tag{10}$$

To verify the sign of the trinomial in the square brackets, we substitute a from (9):

$$\eta^2 + (\alpha + 1)\eta + \alpha(\alpha + 1) + \frac{b^2}{\alpha + 1} - \alpha^2 = \eta^2 + (\alpha + 1)\eta + \alpha + \frac{b^2}{\alpha + 1} > 0,$$

since $\eta > 0$ and $\alpha > 0$. Hence, the sign of the product $(\eta - \alpha)(\eta - 1)$ defines the sign of expression (10). Since the left-hand side of Eq. (10) is the square of $\eta'^2 \geq 0$, the of the right-hand side should also be nonnegative; that is, it should have the form

$$(\eta - \alpha)(\eta - 1) \geq 0. \tag{11}$$

When the expression is equal to zero is a trivial case, where the field strength is constant $E = \text{const} = E_0$ ($\eta = \eta_0 = 1$). The sign of the strict inequality depends on the $\alpha > 1$ or $\alpha < 1$. In the first case, the inequalities

$$\alpha > 1; \quad \eta \leq 1. \tag{12}$$

will be the solution to Eq. (11).

In the second case, the inequalities of the opposite sign will be the solution:

$$0 < \alpha < 1; \quad \eta \geq 1. \tag{13}$$

On the other hand, since $\eta(1) = 1$ has the meaning of the field strength in the center of the layer, inequalities (12) and (13) refer to the monopolar homostructure (the convex $E(x)$ curve) and the monopolar heterostructure (the concave $E(x)$ curve), respectively. Hence, no bipolar structures were found in the exact solution, and the abovementioned conditions of the existence of positive roots for Eqs. (6) and (7) are the only necessary conditions. Therefore, the conclusion regarding the existence of bipolar structures was premature.

Below, we obtain an exact solution, and with this aim, we present positive-definite form (10) as

$$\eta'^2 = \frac{\pi_0}{2}[(\eta - m)^2 + n^2](\eta - \alpha)(\eta - 1), \tag{14}$$

with the following notations:

$$m \equiv -\frac{\alpha + 1}{2}; \quad n^2 \equiv \alpha(\alpha + 1) + a - \left(\frac{\alpha + 1}{2}\right)^2. \tag{15}$$

Integrating (14), we find

$$\int_\eta^1 \frac{d\eta}{\sqrt{(\eta - \alpha)(\eta - 1)[(\eta - m)^2 + n^2]}} = \pm\int_\xi^1 \sqrt{\frac{\pi_0}{2}}d\eta, \tag{16}$$

where the sign "+" corresponds to the homocharge, and the sign "–" refers to the heterocharge. The integral in the left-hand side to within the factor of $(1/\sqrt{qp})$ is an

incomplete elliptic integral of the first kind and, according to [9],

$$\frac{1}{\sqrt{qp}}F(\varphi, k) = -\sqrt{\frac{\pi_0}{2}}(\xi - 1) = \sqrt{\frac{\pi_0}{2}}\lambda, \qquad (17)$$

where $\lambda = 1 - \xi$ is the coordinate counted from the center of the cell (layer) to the electrode surface, φ and k (the absolute value of the integral) are equal, respectively, [9]

$$\varphi \equiv 2\arctan\sqrt{\frac{q}{p}\frac{\beta - \eta}{\alpha - \eta}}; \quad k \equiv \frac{1}{2}\sqrt{\frac{(p+q)^2 + (\alpha - \beta)^2}{pq}}; \qquad (18)$$

$$p^2 \equiv (m - \alpha)^2 + n^2; \quad q^2 \equiv (m - \beta)^2 + n^2,$$

and β is the upper limit of the integral $F(\varphi, k)$ ($\beta = 1$).

It follows from the first formula in (18) that

$$\eta(\varphi) = \frac{\alpha\left(q\beta/p\alpha - \tan^2\frac{\varphi}{2}\right)}{q/p - \tan^2\frac{\varphi}{2}}. \qquad (19)$$

Equations (17)–(19) give an exact analytical solution to the problem. Namely, using the numerical values of parameters π_0, α, β, m, and n in Eqs. (18), we find p, q, and K. Having obtained the latter, we find $F(\varphi, k)$ as a function of the coordinate λ according to Eq. (17):

$$F(\varphi, k) = \sqrt{\frac{\pi_0 qp}{2}}\lambda. \qquad (20)$$

Then, we find φ using the tables or plots $F(\varphi, k)$ and, using Eq. (19), we find $\eta(\varphi)$, or, to be more exact, $\eta(\varphi(F(\lambda)))$.

With the aim of utilizing the developed methods for the solution to the problem, we consider a specific numerical example that will be solved using two methods: an approximate method using the Taylor series expansion and an exact one using an elliptic integral according to the scheme described above.

First, transform initial equation (6) dividing all its terms by π_0:

$$\frac{\eta''}{\pi_0} = \eta^3 + \left(\frac{\pi_*}{\pi_0} - 1\right)\eta - \frac{\pi_3}{\pi_0}; \quad \eta(1) = 1; \quad \eta'(1) = 0, \qquad (21)$$

where

$$\pi_* = \frac{l^2}{\tau_0 D}; \quad \tau_0 = \varepsilon/\sigma_0. \qquad (22)$$

Assume $\pi_0 = 1$ and also let approximately $\pi_*/\pi_0 = 0.10$ and $\pi_3/\pi_0 = 0.55$. Then, Eq. (21) takes the form

$$\eta'' = \eta^3 = 0.9\eta - 0.55; \quad \eta(1) = 1; \quad \eta'(1) = 0. \qquad (23)$$

Table of calculations of $\eta(\lambda)$

	λ	0	0.2	0.4	0.6	0.8	1.0
1	$\tilde{\eta}$	1.00	0.99	0.96	0.91	0.84	0.73
2	$F(\varphi, 1)$	0	0.35	0.71	1.06	1.42	1.77
3	φ^0	0	20	37	52	63	69
4	$\bar{\eta}$	1.00	0.99	0.96	0.89	0.77	0.64
5	$\bar{\eta}$	1.00	0.99	0.97	0.88	0.77	0.59

Expanding the solution into the Taylor series with an accuracy to the terms $(\xi - 1)^8$, we obtain

$$\eta(\xi) \cong 1 - 0.2250(\xi - 1)^2 - 0.0394(\xi - 1)^4 + 0.0023(\xi - 1)^6 + 0.0007(\xi - 1)^8. \qquad (24)$$

The calculations made using this formula are presented in the table.

Now, we examine the exact solution calculating the necessary parameters:

$$a = 2 \times 0.1 - 1 = -0.8; \quad b^2 = 4 \times 0.55 = 2.2.$$

To find α, we set the square brackets in (7) equal to zero:

$$\eta^3 + \eta^2 - 0.8\eta - 3 = 0. \qquad (25)$$

We find numerically a positive root $\alpha = 1.3219$. Having found m and n^2 using Eqs. (15), we obtain from (14)

$$\eta' = \frac{1}{\sqrt{2}}\sqrt{[(\eta + 1.1610)^2 + 0.9215](\eta - 1.3219)(\eta - 1)}.$$

Let us calculate parameters p, q, and k using Eqs. (18), where $m = -1.1610$; $n^2 = 0.9215$; $\alpha = 1.3219$; $\beta = 1$; $p = 2.6620$; and $q = 2.3846 \Rightarrow K \cong 0.99999 \simeq 1.0000$. We find from (19)

$$\eta(\varphi) = 1.3219\frac{0.6720 - \tan^2\frac{\varphi}{2}}{0.8883 - \tan^2\frac{\varphi}{2}}. \qquad (26)$$

Equation (20) takes the form

$$F(\varphi, 1) = 17741\lambda. \qquad (27)$$

Using the values $0 \le \lambda \le 1$ and the tables in [10], we find $F(\varphi, 1)$ and φ; then, we find $\eta(\varphi)$ using Eq. (26). The results are shown in the table.

The line $\tilde{\eta}$ shows the calculations according approximate Eq. (24), while the line $\bar{\eta}$ is calculated using Eqs. (25) and (27).

It is easy to see that, for $k = 1$, the elliptic integral is expressed by an elementary formula that directly follows from its definition in Legendre's form:

$$F(\varphi, 1) = \ln\left[\tan\left(\frac{\pi}{4} + \frac{\varphi}{2}\right)\right] = 1.7741\lambda. \quad (28)$$

It follows from this that

$$\tan\frac{\varphi}{2} = \frac{e^{1.7741\lambda} - 1}{e^{1.7741\lambda} + 1} = \tanh(0.8871\lambda).$$

Hence, we obtain from (25)

$$\eta(\lambda) = 1.3219\frac{0.6720 - \tanh^2(0.8871\lambda)}{0.8883 - \tanh^2(0.8871\lambda)}. \quad (29)$$

In line 5 of the table, the values of $\bar{\eta}$ calculated according Eq. (29) are given. The difference in the results obtained using the different methods is insignificant, and it is mainly observed for large λ, that is, near the electrodes, where the convergence of the Taylor series is somewhat worse. In general, the approximate formulas according to the method using the simple Taylor series expansion to within the sixth order inclusive are quite reasonable for the calculations.

Thus, two methods for analytical solution of the Nernst–Planck equations have been developed: an approximate method using an expansion in a power series and an exact one using the method of elliptic integrals. The coincidence of the results of the calculations allows us to conclude that these methods are admissible in solving the problems of charge formation in the models using the equations mentioned above. Furthermore, it was stated that, in the framework of the same models, the classic homocharge and heterocharge distributions of an electric field in the interelectrode gap are valid.

The search for bipolar structures should be continued, either by developing the hypothesis of microbreakdown in the near-electrode layer [6,7] or by investigating the Nernst–Planck equations taking into account the nonconservation of the partial currents ($\operatorname{div}\vec{j}_+ \neq 0$, $\operatorname{div}\vec{j}_- \neq 0$). Another possibility may be hidden in discussed problem (2), which takes into account the asymmetry of currents $j_+ - j_- \neq 0$ ($\pi_2 \neq 0$). It is expedient to start a new search for the mechanisms of the charge formation from the latter problem, since it is a direct generalization of the previous one.

ACKNOWLEDGMENTS

This work is supported by the Academy of Sciences of Moldova, grant no. 06.13 CRF.

REFERENCES

1. Ostroumov, G.A., *Vzaimodeistvie elektricheskikh i gidrodinamicheskikh polei* (Interaction of Electric and Hydrodynamic Fields), Moscow: Nauka, 1979.
2. Taris, P.P. and Guizonier, P., Phenomenes lies a la conductibilies des liquides isolante, *J. Phys. Appl.*, 1964, no. 6.
3. Rychkov, Yu.M. and Stishkov, Yu.K., Electric Field Strength and Space Charge in Technical Liquid Dielectrics, *Kolloidn. Zh.*, 1978, no. 6.
4. Stishkov, Yu.K. and Ostapenko, A.A., *Elektrogidrodinamicheskie techeniya v zhidkikh dielektrikakh* (Electrohydrodynamic Flows in Liquid Dielectrics), Leningrad: Izd. Leningr. Gos. Univ., 1989.
5. Apfel'baum, M.S. and Polyanskii, V.A., On the Space Charge Formation in Low Conductive Media, *Magn. Gidrodin.*, 1982, no. 1.
6. Grosu, F.P. and Bologa, M.K., Peculiarities of Electrization of Low Conductive Liquids in an External Electric Field, *Elektronnaya Obrabotka Materialov*, 2006, no. 4, pp. 37–46.
7. Grosu, F.P. and Bologa, M.K., On Bipolar Space-Charge Structures in Low Conductive Liquids in an External Electric Field, *Elektronnaya Obrabotka Materialov*, 2007, no. 1, pp. 47–51.
8. Kamke, E., *Spravochnik po obyknovennym differentsial'nym uravneniyam* (Handbook on Ordinary Differential Equations), Moscow: Nauka, 1971.
9. Gradshtein, I.S. and Ryzhik, I.M., *Tablitsy integralov, summ, ryadov i proizvedenii* (Tables of Integrals, Sums and Products), Moscow: Gos. Izd. Fiz.–Mat. Lit., 1962.
10. Yanke, E., Emde, F., and Lesh, F., *Spetsial'nye funktsii* (Special Functions), Moscow: Nauka, 1977.

ISSN 1068-3755, Surface Engineering and Applied Electrochemistry, 2007, Vol. 43, No. 4, pp. 257–264. © Allerton Press, Inc., 2007.
Original Russian Text © P.V. Glushchenko, Yu.K. Stishkov, 2007, published in Elektronnaya Obrabotka Materialov, 2007, No. 4, pp. 34–41.

ELECTRICAL PROCESSES
IN ENGINEERING AND CHEMISTRY

Modeling of the Through EHD-Flow Structure in a Wire–Wire System

P. V. Glushchenko and Yu. K. Stishkov

St. Petersburg State University, ul. Ul'yanovskaya 3, St. Petersburg, Petrodvorets, 198504 Russia

Received January 2, 2007

Abstract—In this article, we show the results of computer modeling of a nonsymmetric EHD flow in a symmetric wire–wire electrode system. This problem was solved using the ANSYS program, which is based on the finite-elements method. We develop the computer modeling of a nonsymmetric EHD-flow algorithm in a stationary variant, which helps us to solve a wide range of electrohydrodynamic problems. In this way, we show the results of solving the problem of a symmetric and nonsymmetric liquid flow in a wire–wire electrode system. A new type of charge diffusion was found, and the disruption of the symmetry when the flow traces are at an acute angel to the center along the axis of symmetry. In this case, the nonsymmetric EHD flow is generated.

DOI: 10.3103/S1068375507040059

INTRODUCTION

In recent decades, great progress has been made in studying the electric conductivity of dielectric liquids. Beginning in the 1980s [1], conferences on this subject became regular, providing testimony to the fact that the problems of electrohydrodynamics (EHD) and electrophysics of liquid dielectrics are of increasing interest. However, with advances in computer hardware, most attention has been concentrated on the numerical modeling of the EHD processes, assisting researchers in making predictions about the outcome of experiments.

Ostroumov provided tremendous advancement for the analysis of the interaction of electric and hydrodynamic fields, and is often referred to as the "father of electrohydrodynamics." In [2], the principal electrophysical and hydrodynamic regularities responsible for the heat and mass transfer processes in insulating liquids located in strong electric fields are systematically presented. Recommendations on the intensification of these processes have been provided, as well as their application in the spheres of science and engineering. Promising avenues for further research have been outlined and recommended.

The case of through flow occurring in a symmetric electrode system at a nonsymmetric charge generation on active and passive electrodes is one of the most interesting types of EHD flows.

In [3], the results of the computer processing of an experiment on the investigation of an EHD flow in a symmetric electrode system are presented. These results are the building blocks for the comparison of the principal quantities obtained through modeling on the basis of the elaborated algorithm set out in that work. The streamlines appearing in Figs. 1a and 1b show the diagram of the through EHD-flow velocity level lines [3]. The interelectrode gap (IEG) is assumed to be a unit length. The level-line maps are normalized according to the maximum velocity value. The jet coming from the active electrode (cathode) is denoted by arrow *1*, while the jets leaving the passive electrode (anode) are denoted by arrow *2*. The electrode centers are situated at the points with coordinates 0.0 (cathode) and 0.1 (anode). It is seen from the figure that the through EHD-flow velocity structure differs substantially from the EHD-flow structure in the wire-over-plate electrode system.

Two areas of liquid acceleration are seen: acceleration area 1 in the interelectrode gap is substantially extended. Although the jets flowing from electrode 1 carry a negative charge, they go far beyond the bounds of the positive electrode and, behind it, one can see area 2, denoted by the arrow.

The through-flow deceleration area is located far beyond the bounds of interelectrode gap. In the region behind the passive electrode, at distance L, the liquid velocity is 50% less (where L is the distance between electrodes). In this region, the electric field is directed opposite to the liquid motion; however, the retarding effect is rather small. This peculiarity of the through EHD flow makes it particularly promising from the point of view of its practical implementation. Thus, studying this charge structure represents an important problem.

COMPUTER MODELING ALGORITHM

The results of computer modeling of the through EHD-flow are presented in this work. In the wire–wire electrode system, the EHD-flow structure is determined by the relation of the ion generation rates on the cathode and anode [4]. If these rates are equal, the flow is realized in the form of two streams with equal intensi-

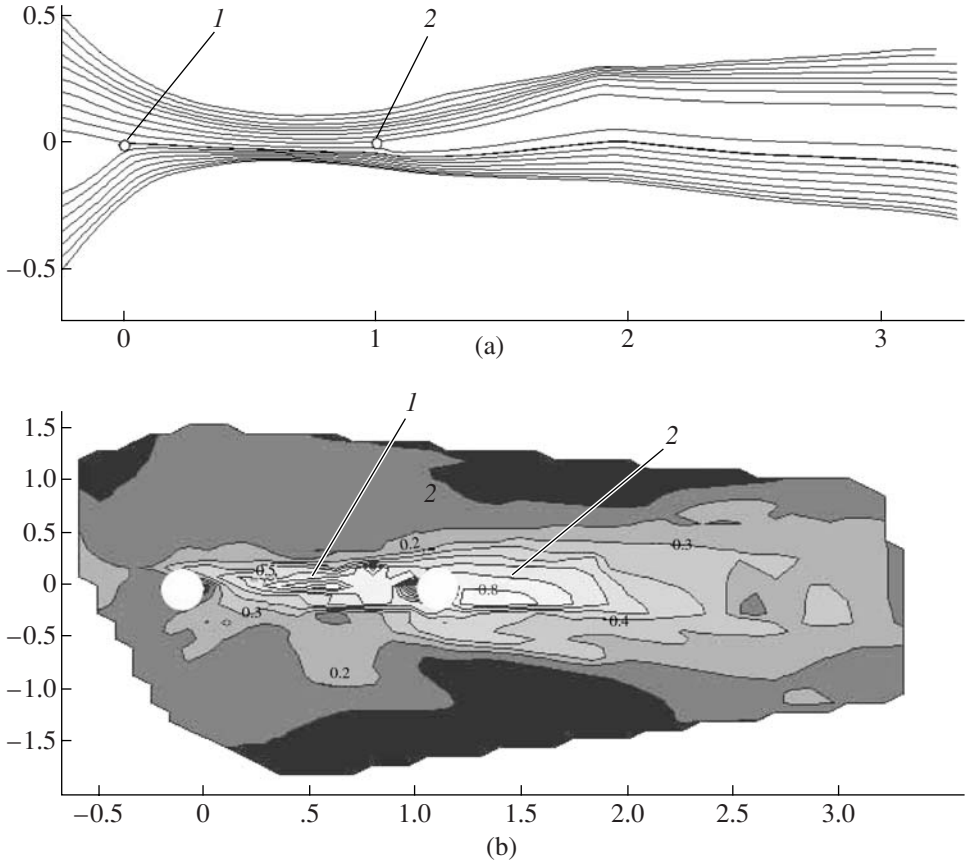

Fig. 1. Through EHD-flow streamlines (a) and rate level-line maps (b).

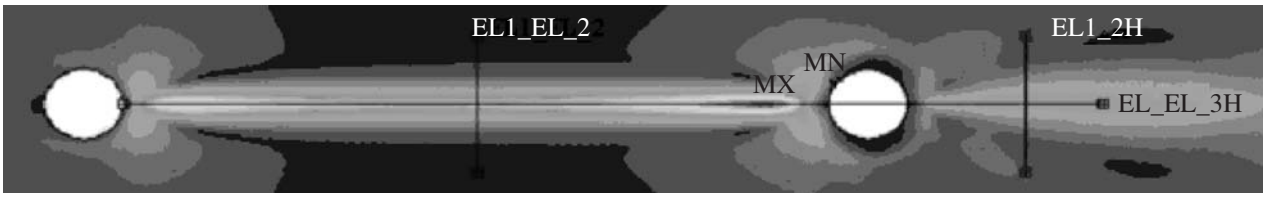

Fig. 2. Through-flow rate contour diagram in the presence of "long" bipolar jets beyond the bounds of the passive electrode.

ties. The streams meet in the interelectrode gap center, where the side jets form, coming at an angle of 90° to the initial jet direction [7]. When the symmetry of the charge generation conditions is disturbed, a distortion in the flow structure occurs. The stream from the electrode upon which the charge generation rate is higher dominates over the oncoming stream, with the side jets of the oncoming streams shifting to the electrode near which the charge generation rate is lower, and the angle of the side-jet inclination to the flow central axis becomes sharp. Through flow represents a borderline case of oncoming streams when a stream from one of the electrodes is more intensive than from the second one. The angle of the side-jet inclination to the flow symmetry axis drops to a very small value, and the jets themselves emerge far beyond the bounds of the interelectrode gap [3].

The solution to this problem was carried out in the ANSYS numerical modeling package, based on the finite-elements method. At present, ANSYS, Inc. leads the market in numerical modeling programs, which is why chose this particular product.

As in [5–7], the finite-elements method is used to solve the problem. The authors have elaborated upon the algorithm, consisting in the successive handling of electrostatic and hydrodynamics problems.

The problem-solving algorithm was as follows:

1. On the basis of the experimental data analysis, there is prescribed the initial "approximate" charge distribution charge is defined, and by tackling the electrostatic problem, we calculate the Coulomb forces, which are rearranged to the hydrodynamic part and are specified as the volumetric load.

Regions of localization of the space charge for active (at the top) and passive (at the left) electrodes

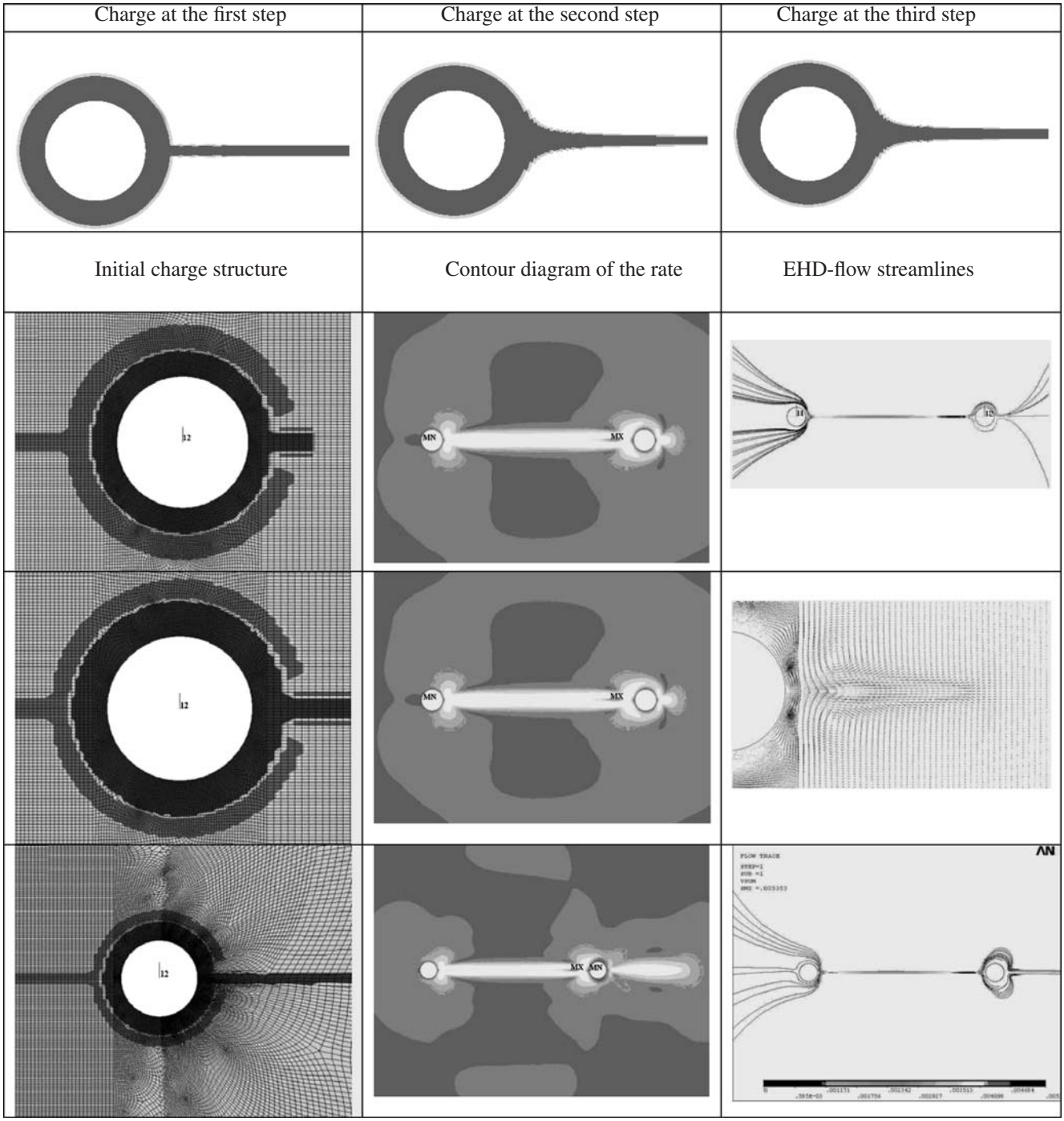

2. The problem is solved in the approximation that the charge is "frozen" into a liquid and, in accordance with these results, a new "refined" charged region is built along the EHD-flow lines, which is obtained at the first iteration.

3. The new charged region is used to solve the electrostatics problem at the following iteration; therefore, the volume electric force is calculated again.

4. The handling of hydrodynamics is repeated using the refined region of the power load.

The process is seen to be iterative, with convergence occurring in the region of the space-charge localization. Upon modeling the through flow at the first iteration, the charge structure was modeled in the form of two ring-shaped regions around the active and passive electrodes, with charges similar to each of them, as well as

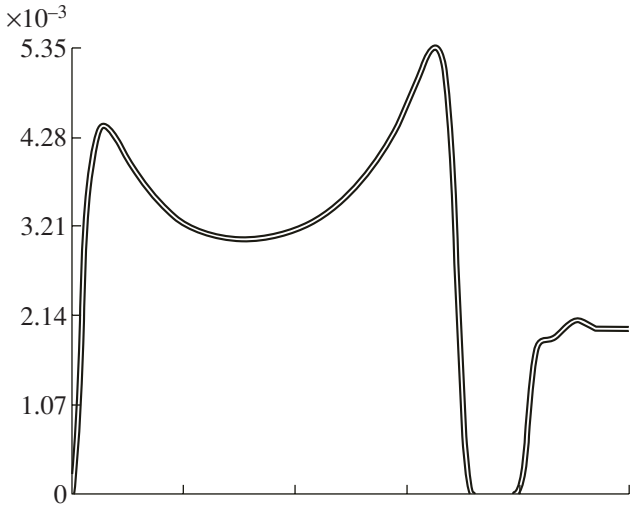

Fig. 3. Diagram of the rate in a horizontal path.

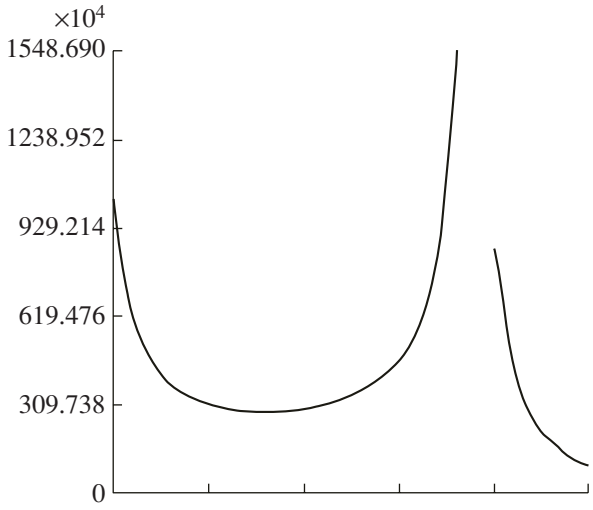

Fig. 4. Diagram of the electric field in a horizontal path.

in the form of thin (with a thickness of less than the electrode radius) charged rectangular strips elongated along the flow axis. The strip coming from the active electrode, is charged similar to it (light-grey shade), while the strip coming from the passive electrode beyond the bounds of IEG is charged with the opposite sign (dark-grey shade) and is limited on both sides by the countercharge strips (see Table 1; at the top, the charged structure in the vicinity of the active electrode; on the lower left, in the vicinity of the passive electrode). The modeling results show that the flow hydrodynamic structure essentially depends on the initial extent of the charged jets beyond the interelectrode gap. It should be pointed out that this parameter is determined by the rate of charge recombination in the bipolar charged jet. The EHD-flow streamlines, corresponding to three different charge structures, are also presented in Table 1. The EHD-flow through performance occurs in the case when the extent of the charged regions in the behind-the-electrode area is comparable with the IEG length. When the charged jets are short, the flow in the behind-the-electrode area ceases to be a through flow and vortexes appear

It should be noted that the nature of the charge distribution at the first step only influences the speed of the problem convergence to the specific distribution, but does not influence the convergence quality. If the parameters were erroneously chosen (that is, at the prescribed parameters, the generation of a through EHD-flow is impossible), some specific flow type will appear that conform to the specific parameters, including the symmetrical case when the charge is preset to be equal on both electrodes.

In the table, the possible initial distributions of the charge are indicated, as well as the concluding outline diagrams of the velocities and streamlines of the calculated flow. The initial charge distributions, in addition to the passive (in this case, the right one) electrode, are displayed in the right-hand portion of the table.

It has been noted that the charged-jet width between the electrodes depends on the near-electrode ring. This relation is constant and equal to 2(w/h = 2).

Two approaches are possible when the through EHD-flow is modeled: (i) to define the expected distribution of the charge on the basis of the experimental data and to iteratively solve the problem with the aim of finding the actual distribution; and (ii) the charge distributions, obtained thanks to the solution of the problem of the symmetrical flow (which occurs at an equal ion generation on both electrodes) [7], are used as the problem input data in the second variant. After the process becomes stationary (which is quite an interesting task), we increase the charge supplied by one of the electrodes, causing a disturbance to the stable equilibrium

Fig. 5. Contour diagram of the pressure (representative pattern for through flow).

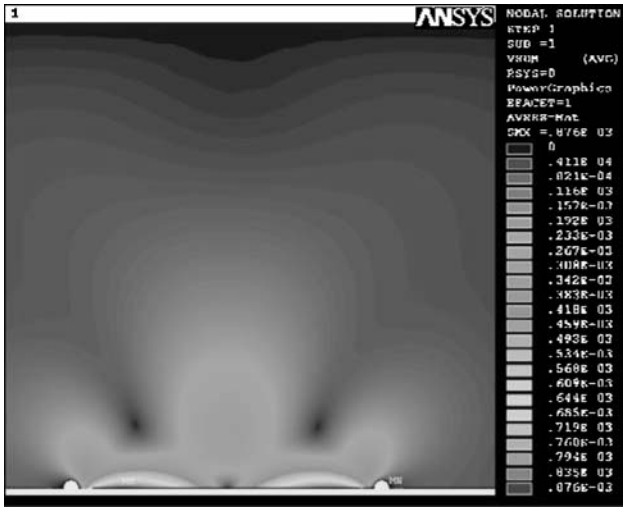

Fig. 6. Contour diagram of the through EHD-flow velocity.

of the charged jets between electrodes and at a certain relation between the charges give rise to the through flow.

I. Let's consider in greater detail the solution obtained in the case when the third variant, presented in the table, at which the most prolonged jet behind the passive electrode, that is, the initial one, is generated. In this case, the charge, coming from the active electrode, flows immediately around the passive electrode with the oppositely charged ring and leaves the interelectrode gap in the form of a thin jet, carrying out the bipolar-waffle charged structure, the external layers of which bear the charge of the active electrode sign while the inner ones bear the charge of the passive electrode with the opposite sign. Beyond the IEG bounds, the jet extends to a distance nearly equal to 3 electrode diameters (1.5 mm). The solution results, whereby the densities of the active and passive charges moderately differ in the module by two iterations, are presented in Fig. 2.

The velocity distribution in the horizontal path (EL_EL_3H in Fig. 2), drawn from the edge of the active electrode (behind the electrodes), is shown in Fig. 3, with the electrode located in the trough valley. According to the electric field distribution in this path, presented in Fig. 4, the charged-liquid rate outline has two peaks, corresponding to the field maximums. The jet speed behind the passive electrode quickly drops and is significantly less in magnitude than the maximum one inside the interelectrode gap. This distribution differs significantly from the through-flow velocity distributions obtained in the experiment (see Fig. 1), necessitating the search for other charge distributions to attain results that are more similar to the experimental ones (Fig. 1) [3].

The representative pattern of the pressure distribution is displayed in Fig. 5. This reflects the specificity of the space-charge distribution in near-electrode areas: at the active electrode, there is an underpressure region, while for the passive one, there is a bipolar structure, whereby the inner ring shows the underpressure and the outer crescent indicates the overpressure.

Special attention must be given to the fact that, in the case of through EHD-flow, there are well-defined regions of localization of charged rings near both electrodes, whereby at the passive electrode on the side facing the active one, the overpressure regions are seen, which are caused by the presence of Coulomb forces directed to the electrode centre.

II. The other method of through EHD-flow production is similar to the experimental one: at an equal ion generation, the so-called symmetrical EHD counterflow comes into existence [6, 7]. In this case, two jets moving from the electrodes meet one another and, then, shift to parallel lateral jets in the center of the interelectrode gap (Fig. 6). Controlling the liquid impurity prop-

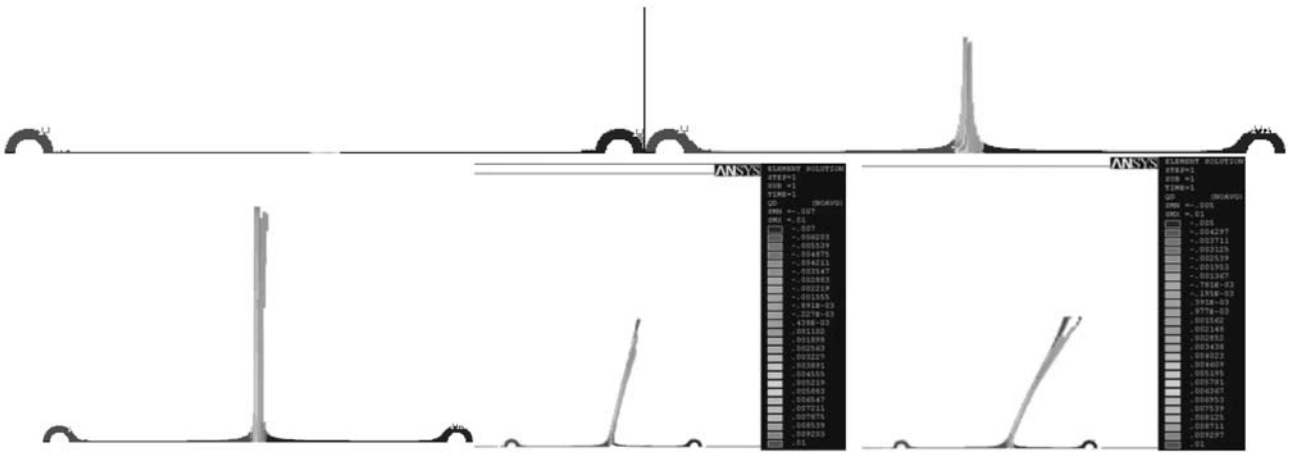

Fig. 7. Generation of the EHD flow from symmetric (steps 1, 2, 3) through to lateral jets (steps 4 and 5).

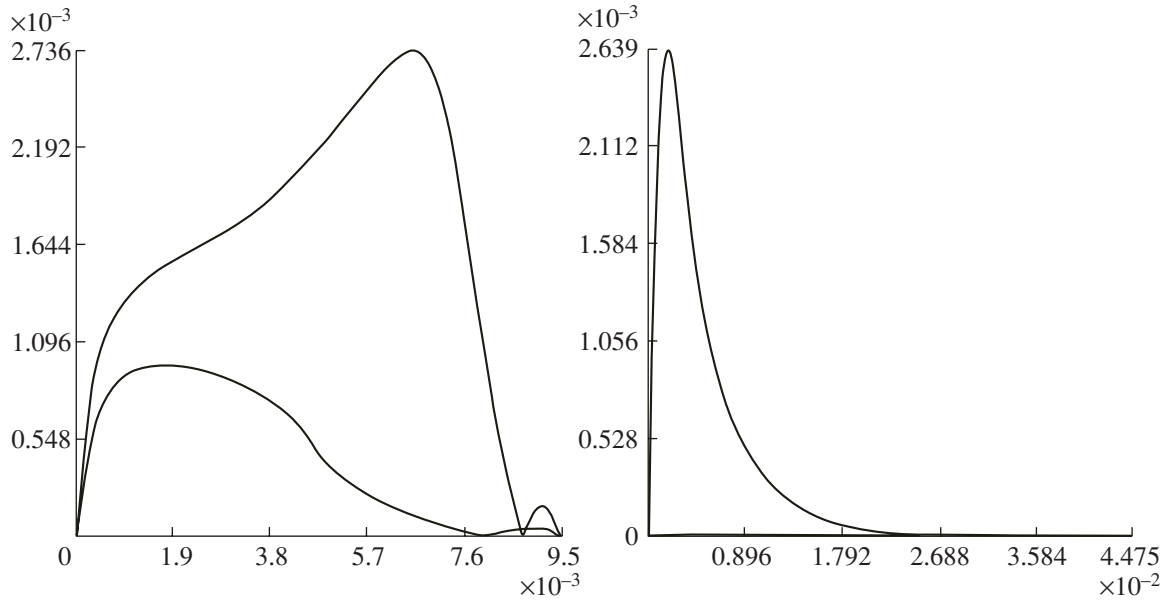

Fig. 8. Rate diagrams in a horizontal path between and behind the electrodes, respectively, at one and two iterations at the charge distributions shown in Fig. 10.

Fig. 9. Liquid-flow streamlines at the through EHD flow from the charge in Fig. 10.

Fig. 10. Charge distribution in the case of through flow.

erties, it is possible to create jets which do not move parallel to one another, but which are tilted to the electrode with a smaller charge generation. Thus, the through EHD flow will be the limiting case.

Let's change the initial geometry of the charged jets in the form of meeting opposite charged strips and assign equal charge densities in the counter jets (Fig. 7, step 1). Depending upon the recombination mechanism, it is possible to produce lateral jets of various lengths (Fig. 7, steps 1–3). Let's enlarge the charge generation on the left electrode; the charged jets remain parallel, but will tilt to the right (towards the lower charge) (Fig. 7, steps 4 and 5).

Upon the charge generation, in addition to the passive electrode being less than the active one by the factor of 8–10, a stable through EHD flow develops (Fig. 10), similar to the obtained one in experiments [3]. The results of the solution using such a relation between charges are shown below.

The peak velocity (Fig. 8, at right), arising beyond the IEG bounds, comparable with the peak (Fig. 8, at left) within the IEG boundaries as well as with the liquid streamlines (Fig. 9), provides the main support for the flow through nature.

Comparing the modeling outcome with the experimental data (Fig. 11), it is possible to distinguish sev-

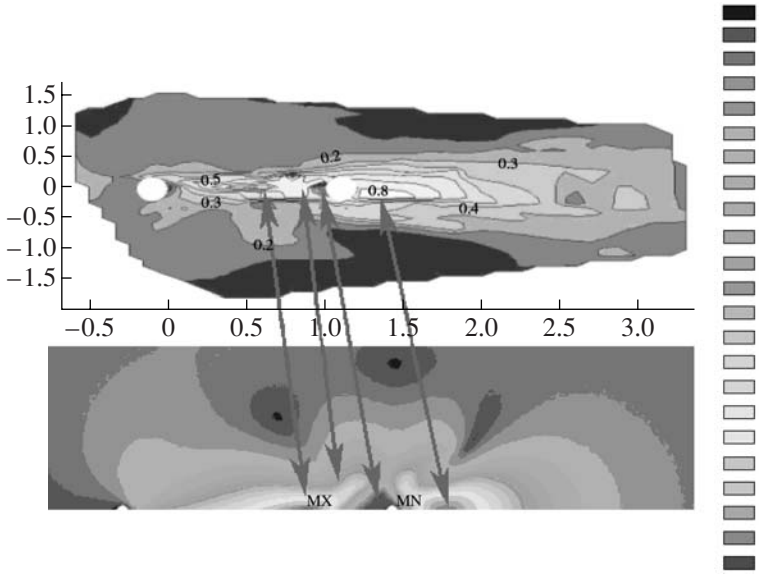

Fig. 11. Correlation between experimental data and modeling results

eral important peculiarities of this flow type (the numbering corresponds to the regions shown in Fig. 11):

(1) The absolute peak velocity is inside the IEG boundaries and is shifted about the center towards the passive electrode (see Fig. 11, arrow 1); thus, after the sharp growth of the velocity from the active electrode edge (up to a peak magnitude of 0.5 according to experimental data and 0.44 according to the modeling outcome), any further increase in velocity is virtually linear.

(2) Short-jet formation occurs, which is directed to the side of the flow around the passive electrode; this is presents in all of the results of modeling and in the experiment shown here (arrow 2).

(3) The charged jet, migrating from the active electrode, does not press the opposite charge close against the passive electrode, as occurs at the common flow around the cylinder; there is, however, an elongated region of liquid stagnancy in front of the passive electrode, caused by the pulling of the charge injected from the near electrode into the jet of the opposite charge without stirring. It is seen from Fig. 8 that, in this region, there is also some local peak caused by the effect of Coulomb forces directed from the electrode forming the acceleration; deceleration is formed by the presence of oppositely directed Coulomb forces, which effect the charge of the opposite sign, having come into this region from the active electrode.

(4) There is an additional peak for the through-flow velocity, which is equal to 0.8 at the absolute maximum of the experiment and 0.79 using the model, in the region behind the passive electrode. It is seen from Figs. 8 and 9 that the liquid goes far beyond the IEG bounds and loses its speed at a distance of several interelectrode gaps, which shows promise for the practical implementation of through EHD flow.

CONCLUSIONS

An algorithm for the EHD-flow problem, using computer modeling in the stationary case and permitting the solution to a wide range of EHD problems, has been described. The program has been written in such a way that the user does not need to study the entire ANSYS numerical modeling software package. Program efficiency has been increased substantially due to the assistance of new principles of flow modeling, which allow its use as an experiment with the purpose of analyzing possible practically useful configurations.

The results of the solution to the problem on liquid symmetric and non-symmetric (through) flows in a symmetric system of wire–wire electrodes are presented in this work. On the one hand, the analysis amplifies the outcomes presented in [7] by making symmetric jets stationary, and, on the other, it considers the fundamental case on breaking the charge distribution symmetry when jets tilted at an acute angle to the central axis of symmetry develop. The so-called through EHD flow comes into existence in this case. Two ranges of liquid acceleration are recognized: the acceleration range in the interelectrode gap is essentially elongated. Although the jets flowing from the active electrode carry the opposite (with respect to the passive one) charge, they go far beyond the boundaries of the passive electrode and, behind it, an additional range of liquid acceleration can be seen, where the speed is as much as 0.8 of the maximum. The through-flow deceleration range is taken far beyond the bounds of the interelectrode gap. In the region behind the passive electrode at distance L, the liquid speed is reduced

by one-half (where L is the distance between the electrodes). In this area, the electric field is directed to the side opposite to the liquid motion direction; however, the decelerating effect is rather small.

When the ratio of the charge injected from the active electrode to the charge coming into the bulk from the passive one is between 1 and 2, a parallel-jet flow develops (when the ratio is 1, the flow is symmetric), which is tilted to the side of the smaller charge generation. At the ratios 2–10, a well-defined through flow develops, whereby the speed increases as the ratio increases within the specified limits. However, a substantial increase in this ratio can cause a charge localization exclusively within the limits of the passive electrode, which is a consequence of the shortage of electric forces participating in repulsion of the opposite charge.

The modeling outcome correlates well with the experimental results, indicating the appropriateness of the assumptions and exclusions made in the work described here.

REFERENCES

1. *Proceedings of 7th Intern. Conf. on Cond. and Break. in Dielectric Liquids (I.C.D.L.)*, Berlin–West–Germany, 1981.
2. Ostroumov, G.A., Interaction between electric and hydrodynamic fields, *Fizicheskie osnovy electrogidrodinamiki* (Electrohydrodynamic Physical Bases), Moscow: Nauka, 1979.
3. Buyanov, A.V. and Stishkov, Yu.K., Peculiarities of EHD flow structure in symmetric electrode system, *Proceedings of the VII International Scientific Conference*, 2003.
4. Stishkov, Yu.K. and Buyanov, A.V., Electrodynamical Currents in a Wire-Wire Electrode System, *Proceedings of the 14th International Conference on Dielectric Liquids*, *Austria*, 2002.
5. Buyanov, A.V., Lazarev, A.S., and Stishkov, Yu.K., EHD flow structure modeling in wire-plane electrode system, *Proceedings of the 5th International EHD Workshop*, *France*, 2004.
6. Elagin, I.A. and Stishkov, Yu.K., Computer Simulation of Electrohydrodynamic Flow Formation Process using a Finite Element Method, *Proceedings of the 5th International EHD Workshop, France*, 2004.
7. Elagin, I.A. and Stishkov, Yu.K., The Investigation of the Recombination Area of Symmetric-Opposite EHD Flows, *Proceedings of the 15th International Conference on Dielectric Liquids, Portugal*, 2005.
8. *Album of Liquid and Gas Flows*, Van-Dike, M., Ed., Moscow: Mir, 1986.

ISSN 1068-3755, Surface Engineering and Applied Electrochemistry, 2007, Vol. 43, No. 4, pp. 265–268. © Allerton Press, Inc., 2007.
Original Russian Text © S.O. Shiryaeva, A.I. Grigoriev, P.V. Moksheev, 2007, published in Elektronnaya Obrabotka Materialov, 2007, No. 4, pp. 42–45.

ELECTRICAL PROCESSES IN ENGINEERING AND CHEMISTRY

Stability of a Rotating Charged Drop(let)

S. O. Shiryaeva, A. I. Grigoriev, and P. V. Moksheev

Demidov Yaroslavl State University, ul. Sovetskaya 14, Yaroslavl, 150000 Russia

Received March 6, 2007

Abstract—A dispersion equation of the rotation of a charged drop along its symmetry axis is derived. It is shown that the rotation increases the charged-drop stability toward the axisymmetric oscillations.

DOI: 10.3103/S1068375507040060

INTRODUCTION

The simulation of the equilibrium forms and stability calculation of rotating charged drops present significant interest for the investigation of the processes occurring in thunderclouds, tornadoes, and other charged liquid-drop systems of natural and artificial origins [1]–[4]. The investigation of the drop stability in various force fields is necessary in order to understand the physical phenomena of tornado and thunderclouds initiation and development. Due to the existence of numerous technical applications involving a rotating charged drop as the primary physical object, the investigation of the drop stability is closely associated with the investigation of the temporal evolution of nonlinearly oscillating drops and mechanisms for their instability and decay under force applications [4]–[7]. For example, E. Trinch and T. Wang [7], investigating an acoustic field that produced large amplitude oscillations of the drops suspended in the acoustic suspension, determined that the large amplitude oscillations are difficult to produce due to the appearance on the drop surface of an asymmetrical running wave, which eventually lead to the drop rotating as a solid body. A similar effect occurred in the experiments of N. Jakobi et al., [8] with free-floating drops in weightlessness, whose large amplitude oscillations were also generated by an acoustic filed. A correct interpretation of such experiments must be based on the well-known equilibrium shape of the charged rotated drop.

PROBLEM FORMULATION

Let us assume that the drop of an ideally incompressible conducting fluid with the surface tension coefficient σ, mass density ρ, and charge Q rotates with a constant angular velocity $\vec{\Omega}$ in a vacuum. Let us investigate the stability of the drop in the first order over the amplitude of the equilibrium deformation of the original spherical shape caused by the rotation related to the radius R. All analyses will be performed in the noninertial coordinate system, rotated along with the drop in the spherical coordinate system with the origin of the coordinate coinciding with the center of the drop and the polar angle ϑ counted from the positive direction of the rotational axis. The entire system consisting of the rotating drop and the surrounding electric field of its charge will be considered closed.

As has been shown in [9], the equilibrium shape of the rotating charged drop in the linear approximation over the amplitude of the equilibrium deformation is flattened along the rotational axis spheroid. The free-surface equation of the drop perturbed by the heat-induced axis-symmetrical capillary wave motion (i.e., induced by the heat motion of the liquid molecules [10]) can be written as

$$r = r(\vartheta) + \xi(\vartheta, t); \quad r(\vartheta) \equiv R(1 - e^2 P_2(\mu)/3);$$

$$\mu \equiv \cos(\vartheta);$$

$$e^2 \equiv \frac{\rho\Omega^2 R^3}{4\sigma(1-W)} \ll 1; \quad W = \frac{Q^2}{16\pi\sigma R^3}; \quad |\xi| \ll 1,$$

where $P_2(\mu)$ is the Legandre polynomial and $\xi(\vartheta, t)$ is a function describing the deformation of an equilibrium spheroidal shape of the charged rotating drop caused by drop oscillations caused by surface tension forces. The deformation amplitude $|\xi(\theta, t)| \sim \sqrt{kT/\sigma}$, where k is Boltzmann coefficient, and T is the absolute temperature. Dimensionless parameter W characterizes the stability of the isolated spherical drop of the conducting fluid relative to its own charge [10]; the drop becomes unstable at $W \geq 1$.

Let us assume that the fluid motion in the drop, caused by the oscillations at its surface, is potential with velocity field potential $\psi(\vec{r}, t)$ and that the electric field of the drop's own charge is electrostatic with potential $\Phi(\vec{r}, t)$. The potentiality of the electrical field remains both in the neighborhood of the unperturbed spheroidal surface of the drop (at $\xi(\theta, t) \neq 0$), and in the presence of a time-dependent deformation (at $\xi(\theta, t) \neq$

0), since the characteristic rate of the drop surface shape change ($\approx\nabla\psi(\vec{r}, t)$) is much smaller than the speed of light in a vacuum c: $\nabla\psi(\vec{r}, t) \ll c$. In this case, the mathematical formulation of the problem of stability of the rotating charged drop can be expressed as

$$\Delta\psi(\vec{r}, t); \quad \Delta\Phi(\vec{r}, t) = 0;$$

$$r \longrightarrow 0: \psi(\vec{r}, t) \longrightarrow 0;$$

$$r \longrightarrow \infty: \Phi(\vec{r}, t) \longrightarrow 0;$$

$$r = r(\vartheta) + \xi(\vartheta, t): \Phi(\vec{r}, t) = \Phi_S(\vec{r}, t);$$

$$\frac{\partial\xi}{\partial t} = -\vec{V}\nabla\xi(\vartheta, t) \approx \frac{\partial\psi}{\partial r} - \frac{1}{r^2}\frac{\partial\psi}{\partial\vartheta}\frac{\partial\xi}{\partial\vartheta};$$

$$p + p_\Omega + p_Q = p_\sigma,$$

where $p = -(\partial\psi/\rho\partial t)$ is the hydrodynamic pressure inside the drop associated with the fluid motion, p_Ω is the pressure on the drop free surface by the centrifugal forces associated with drop rotation,

$$p_\Omega = \int_0^{r(\vartheta)+\xi(\vartheta, t)} \rho\Omega^2 x dx \equiv \frac{1}{2}\rho\Omega^2[r(\vartheta) + \xi(\vartheta, t)]^2;$$

$p_Q = -(-\nabla\Phi)^2/8\pi$ is the pressure of the electric field of its own charge on the free surface of the drop, $p_\sigma = \sigma\mathrm{div}_S\vec{n}$ is the surface tension force pressure, $\vec{n}$ is the unity vector normal to the free surface of the drop, and $\Phi_S(t)$ is the constant along the drop surface value of the electric potential.

Additionally, the shape of the drop surface must satisfy the conditions of the mass preservation and stationarity of the center of mass,

$$\int_V r^2 dr d\mu d\varphi = -\frac{4\pi}{3}R^3;$$

$$V = [0 \le r \le r(\vartheta) + \xi(\vartheta, t),\ 0 \le \vartheta \le \pi,\ 0 \le \varphi \le 2\pi];$$

$$\int_V \vec{e}_r r^3 dr d\mu d\varphi = 0,$$

which allows us to set a lower limit to the spectrum of modes participating in the formation of the shape of the free surface of the drop by requiring $n \ge 2$ [10, 11]. The full electrical charge of the drop should also be preserved:

$$\oint_S (\vec{n}\cdot\nabla\Phi) r^2 d\mu d\varphi = -4\pi Q;$$

$$S = [r = r(\vartheta) + \xi(\vartheta, t),\ 0 \le \vartheta \le \pi,\ 0 \le \varphi \le 2\pi].$$

PROBLEM SOLUTION

We will conduct the subsequent analysis in accordance with the standard procedure described in detail in [1], [4], [10], and [12], namely, the linearization of the problem in the neighborhood of the spherical drop shape, the calculation of the unknown functions $\xi(\vartheta, t)$, $\psi(\vec{r}, t)$, and $\Phi(\vec{r}, t)$ as infinite rows along Legandre's polynomials, and obtaining the dispersion equation from the condition of compatibility of the hydrodynamical boundary conditions at the free surface of the liquid.

Let us state the problem solution as

$$\xi(\vartheta, t) = \sum_{n=2}^{\infty} A_n P_n(\mu)\exp(i\omega t);$$

$$\psi(r, \vartheta, t) = \sum_{n=2}^{\infty} C_n r^n P_n(\mu)\exp(i\omega t);$$

$$\Phi(r, \vartheta, t) = \sum_{n=2}^{\infty} D_n r^{-(n+1)} P_n(\mu)\exp(i\omega t).$$

In the derivation of these equations, we took into account that the hydrodynamic potential of the velocity field must be finite in the center of the drop, while the potential of the electric field associated with oscillations of the surface of the charged drop must approach zero at infinity. A_n, C_n, and D_n in the above expressions are the unknown coefficients.

Let us find the relation between A_n, B_n, and C_n by satisfying the hydrodynamic boundary conditions at the fluid free surface and expressing C_n and D_n through A_n, and write down the expressions for the pressures p, p_Ω, p_Q, and p_σ for the spherical drop surface:

$$r = R: p = -\rho\frac{\partial\psi(r, \vartheta, t)}{\partial t} = \omega^2 R\rho\exp(i\omega t)\left[\sum_{n=2}^{\infty}\frac{1}{n}\left\{A_n + \frac{e^2}{3}\left\{A_{n+2}\frac{3(n+1)(n^2+n-4)}{2(3+2n)(5+2n)}\right.\right.\right.$$

$$\left.\left.\left. + A_n\frac{(n+1)(n^2-n-3)}{(2n-1)(2n+3)} + A_{n-2}\frac{3(-1)^{4(2-n)}n(n-1)^2}{2(2n-3)(2n-1)}\right\}\right\};$$

$$p_\Omega = -\frac{2}{3}R\rho\Omega^2\exp(i\omega t)\left[\sum_{n=2}^{\infty}\left(A_n\left(-3\frac{n^2+n-1}{(2n-1)(2n+3)}\right)\right.\right.$$

$$+A_{n+2}\left(\frac{3}{2}\frac{(n+1)(n+2)}{(2n+5)(2n+3)}\right.$$

$$\left.\left.+A_{n-2}\left(\frac{3(-1)^{8-4n}}{2}\frac{n(n-1)(n+2)}{(2n-1)(2n-3)}\right)P_n(\mu)\right]\right];$$

$$p_Q = \frac{Q^2}{8\pi R^4}+\frac{Q^2}{4\pi R^5}\left\{\sum_{n=2}^{\infty}(n-1)A_nP_n(\mu)\right.$$

$$-e^2\exp(i\omega t)\left[\sum_{n=0}^{\infty}\left(\frac{(n+1)(n+2)(n-7)}{2(3+2n)(5+2n)}A_{n+2}\right.\right.$$

$$+\frac{n(n+1)(n-4)}{3(2+2n)(2n-1)}A_n$$

$$\left.\left.\left.+\frac{(-1)^{4(2-n)}n(n-1)(n-5)}{2(n-3)(2n-1)}A_{n-2}\right)P_n(\mu)\right]\right\};$$

$$p_\sigma = \frac{2\sigma}{R}-\frac{4\sigma}{3R}e^2P_2(\mu)+\left[\frac{\sigma}{R^2}\sum_{n=2}^{\infty}(n-1)(n+2)A_nP_n(\mu)\right]$$

$$+\frac{2\sigma}{3R^2}e^2\exp(i\omega t)\left[\sum_{n=2}^{\infty}\left(A_{n+2}\frac{3(n+1)(n+2)(n^2+5n+10)}{2(2n+3)(2n+5)}\right.\right.$$

$$+A_n\frac{n(n+1)(n^2+n-4)}{(2n+3)(2n-1)}$$

$$\left.\left.+A_{n-2}\frac{3(-1)^{4(2-n)}n(n-1)(n^2-3n+6)}{2(2n-3)(2n-1)}\right)P_n(\mu)\right].$$

Finally, substituting these expressions into the condition of the pressure balance at the free surface of the drop (dynamic boundary condition), and using the orthogonality of the Legandre polynomials, we will obtain the dispersion solution of the problem, which, in nondimensional variables, where $R = \sigma = \rho = 1$ (i.e., we choose the drop radius R, surface tension σ, and liquid density ρ as the scaling factors), can be written as

$$\omega^2 = n(n-1)[(n+2)-W]$$

$$+e^2\left[W\frac{n^4+17n^2+21n-21}{3(3+2n)(2n-1)}\right.$$

$$\left.-\frac{(n+2)(n^4-5n^3+4n^2+25n-9)}{3(3+2n)(2n-1)}\right].$$

The condition of drop instability is the passing of the frequency square ω^2 through zero into the negative value region. In this case, for the frequency itself, we will obtain two conjugated solutions ($\omega_{1,2} = \pm i\gamma$), one of which will correspond to the decay of motion with decrement $-\gamma$, and the other to their increase with increment $+\gamma$. Equating the frequency square in the obtained dispersion equation to zero, we will obtain the critical values for the drop stability relation between parameters W, n, and e^2. In the approximation $e^2 \ll 1$, this relation can be expressed in a simplified form:

$$W_{cr} = (n+2)+e^2\frac{5n^4+23n^3+47n^2+30n-24}{3n(4n^3-7n+3)}.$$

It is easy to see that, for the arbitrary mode numbers, the critical value of parameter W increases with the growth of e^2.

This means that the rotation of the drop leads to an increase in its stability with regards to axisymmetric oscillations, which agrees with the previously obtained results of both numerical [13] and analytical [12, 14] investigations, where the flattened spheroidal shape was an a priori set condition rather than caused by physical forces, as in the current work.

CONCLUSIONS

The equilibrium shape of a charged rotating drop in a wide range of angular velocities and drop charges can be approximated by a spheroid flattened along the rotation axis.

ACKNOWLEDGMENTS

This work was supported by the Russian Foundation for Basic Research (project no. 06-01-00066-a).

REFERENCES

1. Grigoriev, A.I. and Grigoriev, O.A., Influence of Rotation and Electrical Charge on Spherical Capsule Stability, *Elektronnaya Obrabotka Materialov*, 1991, no. 3, pp. 41–44.
2. Grigoriev, A.I. and Sinkevich, O.A., Nature of Electrical Phenomena in Tornado, *ZhTF*, 1986, vol. 56, no. 10, pp. 1985–1987.
3. Grigoriev, A.I. and Shiryaeva, S.O., The Possible Physical Mechanism of Initiation and Growth of Lightning, *Physica Scripta*, 1986, vol. 54, pp. 660–666.
4. Brown, R.A. and Scriven, L.E., The Shape and Stability of Rotating Liquid Drop, *Proc. R. Soc., Londo*n, 1980, vol. A371, pp. 331–357.
5. Natarajan, R. and Brown, R.A., Third-Order Resonance Effects and the Non-Linear Stability of Drops Oscillations, *J. Fluid Mech*., 1987, vol. 183, pp. 95–121.

6. Natarajan, R. and Brow, R.A., The Role of Three-Dimensional Shapes in the Break-up Charged Drops, *Proc. R. Soc.*, London, 1987, vol. A410, pp. 209–227.

7. Trinch, E. and Wang, GT.G., Large Amplitude Free an Driven Drop-Shape Oscillations: Experimental Observations, *J. Fluid Mech.*, 1982, vol. 122, pp. 315–338.

8. Jakobi, N., Croonquist, A.P., Elleman, D.D., and Wang T.G., Acoustically Induced Oscillations and Rotation of a Large Drop in Space, *Proc. 2nd Int. Colloq*. On Drop and Bubbles., Pasadena, 1982, JPL Publication 827, p. 31.

9. Shiryaeva, S.O., Grigoriev, A.I., and Moksheev, P.V., Equilibrium Shape of the Charged Drop Rotating along Axis of Symmetry, *Elektronnaya Obrabotka Materialov*, 2006, no. 4, pp. 46–52.

10. Schweizer, J.W. and Hanson, D.N., Stability Limit of Charged Drops, *J. Coll. Int. Sci.,* 1971, vol. 35, no. 3, pp. 417–423.

11. Landau, L.D. and Lifshitz, E.M., *Gidrodinamika* (Hydrodynamics), Moscow: Nauka, 1986.

12. Grigoriev, A.I. and Firstov, A.A., Critical Instability Conditions for the Flattened Spheroid Shaped Charged Drop, *Elektronnaya Obrabotka Materialov*, 1992, no. 6, pp. 20–23.

13. Basaran, O.A. and Scriven, L.E., Axisymmetric Shapes and Stability of Isolate Charged Drops, *Phys. Fluids A*, 1989, vol. 1, no. 5, pp 795–798.

14. Shchukin, S.I. and Grigoriev, A.I., Stability of the Three-axis Ellipsoid Shaped Charged Drop, *ZhTF*, 1998, vol. 68, no. 11, pp. 48–51.

ISSN 1068-3755, Surface Engineering and Applied Electrochemistry, 2007, Vol. 43, No. 4, pp. 269–275. © Allerton Press, Inc., 2007.
Original Russian Text © N.I. Kuskova, L.Z. Boguslavskii, A.A. Smal'ko, A.A. Zubenko, 2007, published in Elektronnaya Obrabotka Materialov, 2007, No. 4, pp. 46–52.

ELECTRICAL PROCESSES IN ENGINEERING AND CHEMISTRY

Obtaining Nanocarbon Using the Electric-Discharge Treatment Method of Organic Liquids

N. I. Kuskova, L. Z. Boguslavskii, A. A. Smal'ko, and A. A. Zubenko

Institute of Pulse Processes and Technologies, National Academy of Sciences of Ukraine, pr. Oktyabr'skii 43-a, Nikolaev, 54018 Ukraine

Received December 4, 2006

Abstract—The principal possibility of nanosize carbon-material synthesis in macroamounts for short intervals of time using the method of electric explosion in a liquid is shown. Conformities with the law of obtaining nanocarbon upon many-cycle treatment are explored; these demonstrated a swaying, falling practically to zero, character of an increasing material mass with an increase in the cycles. The mass of the obtained nanocarbon is determined by the amount of atoms in the chains of the hydrocarbons, by the injected energy in a plasma channel during one pulse, and the quantity of treatment cycles.

DOI: 10.3103/S1068375507040072

INTRODUCTION

Obtaining and the investigation of nanomaterials are one of the most rapidly developing and necessary directions in modern science. In this respect, problems concerning the nanostates of carbon are of special importance. International scientific literature has already adopted the term "nanocarbon" for the designation of a family consisting of various types of fullerenes, carbon nanotubes, nanographite, nanodiamonds, carbon "bulbs," etc. [1, 2]. In essence, quite a number of new carbon nanostructures has been discovered, which are interesting as the basis for modern nanomaterials being widely applied: from biology and medicine to a new generation of electronics and mechanical engineering.

Despite long and large-scale investigations in the development of nanocarbon synthesis methods, this theme is still relevant, because none of the impressive number of proposed methods (i.e., electric arc, laser sputtering, electrolysis, pyrolysis, electric explosion of graphite conductors, etc.) [3–5] allows for the rapid and qualitative attainment of material macroamounts sufficient for industrial use.

In the present paper, a high-voltage pulse electric breakdown (electric explosion) of organic liquids as a method to obtain nanocarbon is considered. This method is proposed on the basis of the following considerations:

– The possibility of nanocarbon synthesis the in flame of hydrocarbons (acetylene and ethylene) in the gas state and at the catalytic decomposition of hydrocarbons is studied in [6]. It is shown in [7, 8] that the diamond-phase formation is a common regularity for all organic liquids in the process of their molecular structure decomposition; at a sufficiently intense dynamic loading, free-carbon evolution is observed.

– Electric explosion in liquid at different stages has quite a number of conditions necessary for the destruction of hydrocarbons under the discharge-channel plasma influence, the transformation of products into vapor, and nanocarbon synthesis at the vapor–gas cavity stage [9].

EXPERIMENTAL

The experimental technique is based on the discharge of a pulse-current generator with stored energy $0.512\ \text{kJ} < W_0 < 4.608\ \text{kJ}$ on the interelectrode space in an organic liquid. A commutator is an air-sphere gap being initiated by an overvoltage of the air space. The pulse frequency was from 0.5 to 1 Hz. The oscillograms of the discharge current and voltage in the interelectrode space were registered with the help of a shunt and a capacitive-voltage divider on an S8-14 electron oscillograph. A number of high-voltage pulses was counted by the PC 02-08 one-channel metering device. The electric discharge installation and electric discharge chamber used as the reactor for the nanocarbon material are shown in Fig. 1. In the latter, the electrode system is immersed into a metal case filled with an organic liquid. The reactor scheme is provided in Fig. 2. The discharge space length was selected according to the condition of a guaranteed breakdown by the discharge voltage generated by the pulse generator. The choice of the space configuration in the form of a coaxial discharge system is caused by the necessity of increasing the resource of the electrodes in a many-pulse series of experiments with repeated cycles.

Liquids with different numbers of carbon atoms C_n (n = 2–20), such as ethyl alcohol, glycerin, hexane, white spirit, kerosene, gas oil, etc., were selected as the organic liquid. The liquid volume was 1.3 l. From 100–

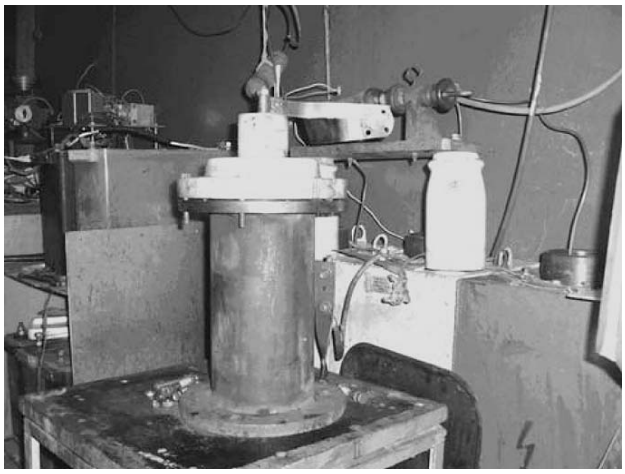

Fig. 1. Electric-discharge installation and reactor for nanocarbon synthesis.

500 pulses were supplied to the discharge space. The treatment resulted in the destruction of carbon chains and in nanocarbon synthesis. After the treatment, the colloid solution was subjected to centrifugation for from 20 min to 1 h on a centrifuge with a rotation velocity 3000 r/min. The transparent liquid was separated and the deposit was weighed. The remaining liquid was subjected to a subsequent many-cycle electric-discharge treatment and centrifugation. The cycles were repeated until the absence of the deposition mass gain. After a complete many-cycle treatment, the obtained deposit was dried. The formed ultradisperse powder was subjected to further analysis using an electron microscope and a roentgen diffractometer.

EXPERIMENTAL RESULTS

The time dependences of the electric-discharge characteristics (current and voltage) for the high-voltage breakdown of space in organic liquids have a form typical for the dielectric liquid-breakdown process. A characteristic oscillogram of the discharge voltage is shown in Fig. 3. The observed stable spread of the time of the breakdown delay from 10 to 100 μs for the given discharge space does not depend on the type of liquid and does not change during the process of the many-pulse and many-cycle treatment. As the generator voltage increases, the spread shifts towards shorter times. Due to the small length of the discharge space, the process of energy generation in the plasma channel has a well-pronounced oscillating character. According to the data from [10], for oscillating modes of discharge at the breakdown of liquid dielectrics, the highest density of the internal energy in the discharge channel is realized and, therefore, the plasma temperature, thus contributing to the thermal destruction of the hydrocarbon chains in liquid layers near the plasma channel.

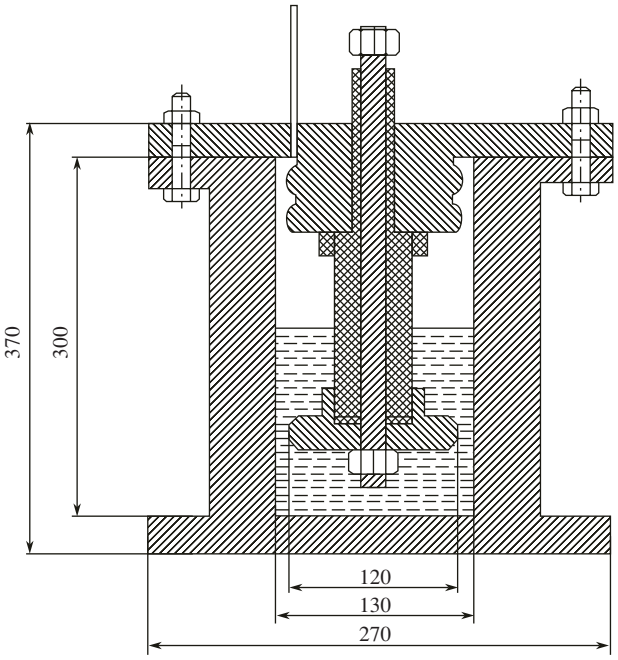

Fig. 2. Scheme of the reactor for nanocarbon synthesis.

Figures 4–8 show the dependences of the obtained nanocarbon substance mass on different parameters. Figure 4 shows a diagram of the masses of the deposit and dried powder obtained upon the treatment of liquids with different numbers of carbon atoms in chains at an equal injected energy. It follows from the diagram that a more than tenfold increase in the deposit mass and twenty-fold increase in the dry-powder mass are observed at the transition from liquids containing two carbon atoms in a molecule to hydrocarbons containing from 11 to 20 atoms in a molecule. It is also seen from the diagram that the mass loss upon drying decreases by a factor of 3–5; however, as the carbon atom number in

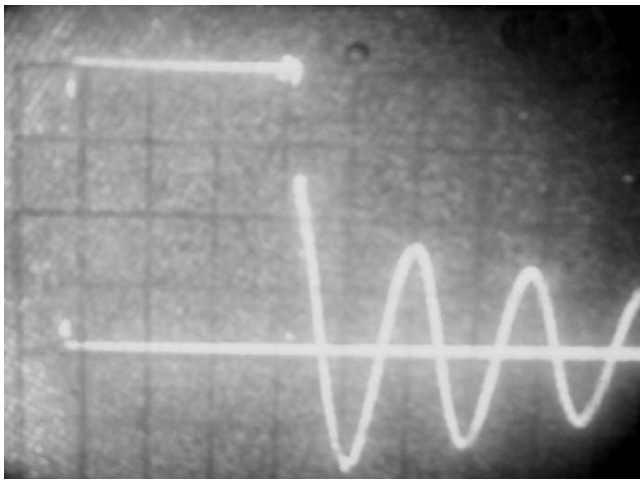

Fig. 3. Typical oscillogram of the voltage.

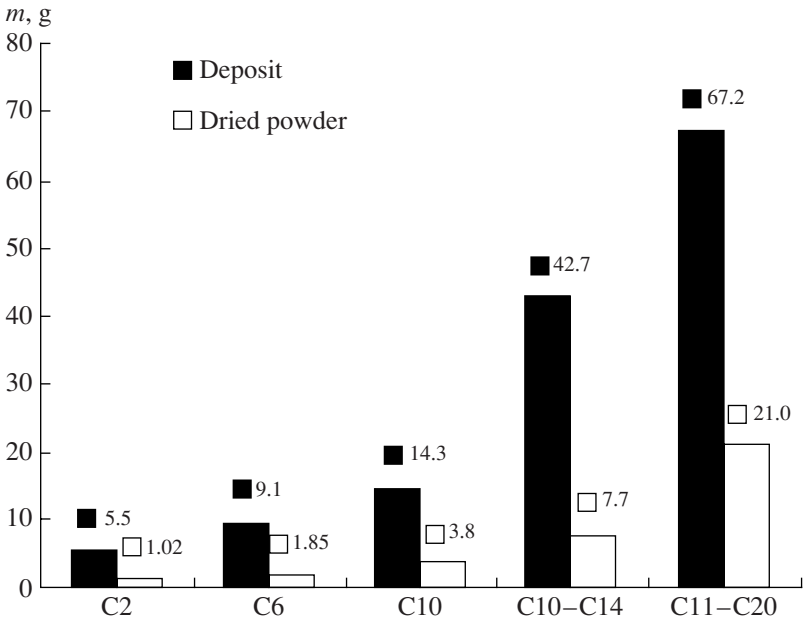

Fig. 4. Obtained masses of the deposit and dry powder of a nanocarbon at W_{inj} = 1040 kJ for organic liquids with different numbers of carbon atoms in molecules.

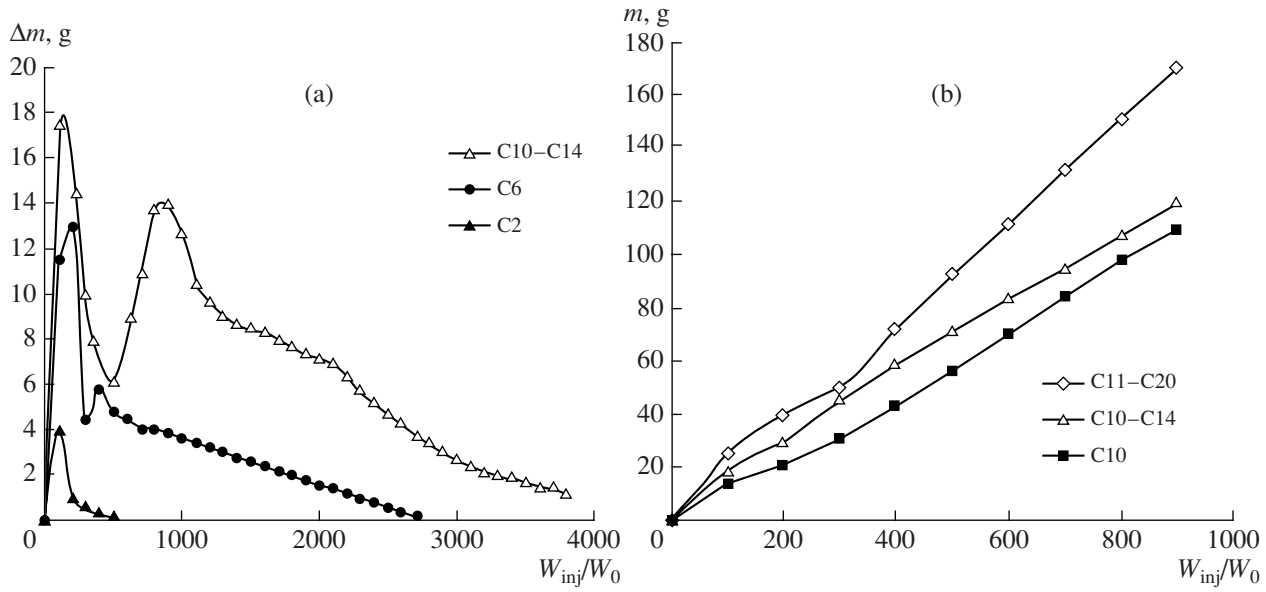

Fig. 5. Mass gain Δm (a) and mass of the deposit m (b) for various hydrocarbon liquids depending upon the injected energy (W_0 = 3.468 kJ).

the molecule increases, the difference becomes less pronounced.

Figures 5 and 6 show graphs of the dependences of the nanocarbon mass gain Δm (a) and total mass m (b) during the process of the cyclic treatment for hydrocarbon liquids with a high n in the molecule C_nH_m at the stored energy of the generator W_0 = 3.468 kJ (Fig. 5) and for liquids with a small n at W_0 = 1.734 kJ (Fig. 6). One cycle corresponds to 100 units W_{inj}/W_0, where W_{inj} is the energy injected during the treatment-cycle process. The mass gain Δm was determined as $\Delta m = m_{i+1} - m_i$, where m_i and m_{i+1} are the deposit masses obtained at previous and subsequent cycles of treatment, respectively. A characteristic peculiarity of the dependences for Δm is a peak achieved during the initial cycles of treatment; for the majority of hydrocarbons, this takes place during the first cycle. After the peak, at first, a decrease in the synthesized nanocarbon amount is observed and,

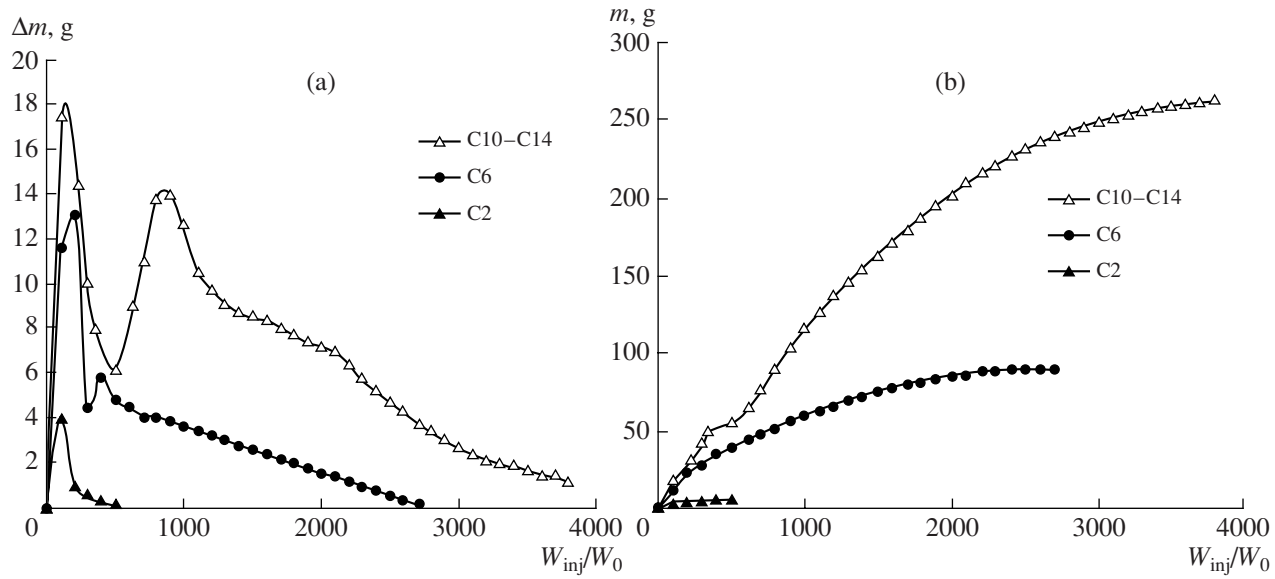

Fig. 6. Mass gain Δm (a) and mass of the deposit m (b) for various organic liquids depending upon the injected energy ($W_0 = 1.734$ kJ).

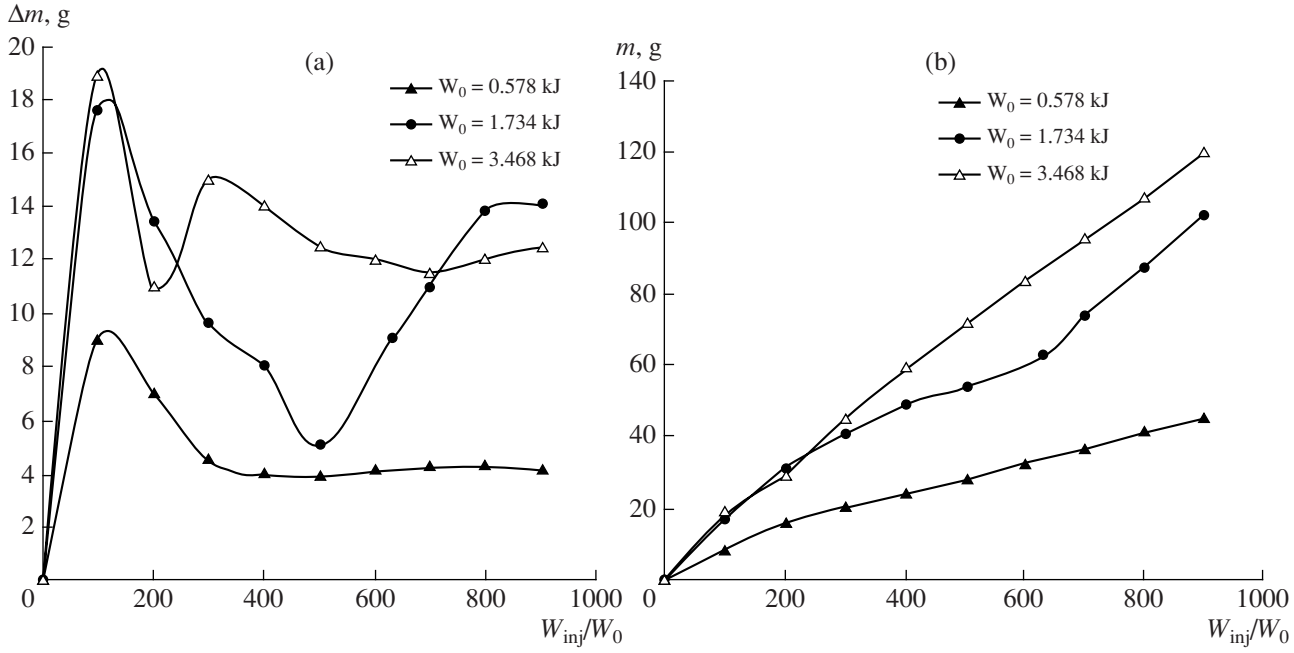

Fig. 7. Investigation of the mass gain Δm (a) and mass of the deposit m (b) for the hydrocarbon liquid C_{10}–C_{14} at different W_0.

then, an increase of the mass gain takes place, whereby the second peak is less than the first. Then, a monotonous decrease is observed, leading to a practically complete cessation of the mass gain. As n decreases, the second peak becomes appreciably less than the first (C_6) and is completely absent for C_2. The complete cessation of the mass gain Δm for the liquids with a low n is achieved after a small number of cycles, significantly increasing as the number of atoms in the hydrocarbon chains increases. In the mass graphs, depending upon W_{inj}/W_0, a decrease in the curve inclination angle in comparison with the beginning of the nanocarbon synthesis process is observed. It is also seen that, as the number of cycles grows, the curves reach saturation. For C_2, the saturation is observed after 5 cycles ($W_{inj}/W_0 = 500$), whereas for C_{10}–C_{14} after 40 cycles and for hydrocarbons with a large n, the maximum has not been practically achieved.

Figure 7 shows the dependences of the mass gain of the deposit Δm (a) and its mass m (b) for one hydrocarbon liquid C_{10}–C_{14} at various stored energies of the generator W_0. The first peak for the Δm dependences is determined by the value of W_0. However, for those cases when $W_0 = 3.468$ kJ and $W_0 = 1.734$ kJ, the peak value changes insignificantly, whereas at $W_0 = 0.578$ kJ, this mass gain decreases by a factor of 3 in comparison with the highest peak. Further behavior of the curves also has a different character. At the maximal W_0, a fall to the minimum and the second-peak achievement occur gradually through 7–8 cycles, with a decrease during 4 cycles and an increase during 3–4 cycles. At $W_0 = 1.734$ kJ, this fall is not practically observed, and the gain Δm does not change after the fall, continuously decreasing until 0. The analogous dependences on the value of W_0 are observed in the graphs showing the change of deposit mass m. The synthesized nanocarbon mass grows with an increasing stored energy. The inclination of the curves reflects the character of the Δm dependences and does not practically differ for high energies through the first three cycles.

The table shows the data for the total evolved mass of the nanocarbon and the required number of pulses at $W_0 = 1.734$ kJ for the synthesis of various hydrocarbons. The investigation was carried out up to the moment of synthesis cessation ($\Delta m \approx 0$).

It is seen from the table that the difference in the yield of total nanocarbon mass achieves two orders for substances with large and small numbers of carbon atoms in a molecule, with the time of the electric discharge treatment, i.e., pulse number, considerably increasing.

After drying, the nanocarbon material was subjected to chemical purification from metal particles and to further analysis. Figure 8 shows the characteristic electron-microscope image of the obtained material with a resolution of 200 nm. It is seen that the value (200 nm) of globules constituting the powder particles confirms the nanodimensional character of the obtained material. It follows from the nanocarbon material diffractogram (Fig. 9) that, in addition to the peaks *C* corresponding to nanographite, the peaks corresponding to the cubic nanodiamond *D* and lonsdaleite *L* are observed. The powder contains about 10% nanodiamond.

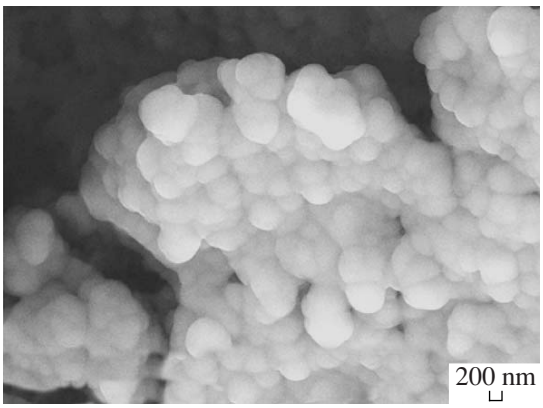

Fig. 8. Electron-microscope image of the nanocarbon material obtained upon treatment of the hydrocarbon liquid C_{10}–C_{14}.

DISCUSSION

The results on the regularities of the nanocarbon mass gain during the process of many-cycle treatment show that only certain fractions of hydrocarbon liquids can transform into the solid phase, i.e., a nanocarbon. Its mass is significantly determined by the number of carbon atoms in the molecules that evolved in the plasma channel during one energy pulse and by the number of treatment cycles. This is confirmed by the character of Δm dependences showing that, at first, the destruction of light molecules takes place and, then, heavy molecules are destroyed. Apparently, this influences the material properties; that is, the material obtained after the initial treatment cycles may differ from that obtained after further cycles.

The conditions in which the experiments were carried out coincide with the range of the physicochemical parameters, causing a high probability of the spontaneous appearance of a new carbon phase—that is, a nanodiamond [11, 12]. The new phase formed under these conditions is characterized by the following: It may be amorphous or a nanocrystal, and the crystallite dimensions significantly depend on the process parameters; the formed structures tend towards relaxation in the case when the "hardening" conditions are not satisfied. The spherical form of the carbon nanoparticles allows us to assume that their increase occurs due to the coalescence of carbon clusters, not due to the diffusion of separate carbon atoms. In addition to the thermodynamic conditions, diamond synthesis may be affected by the specific peculiarities of the shock-wave compression at the shock-wave front, contributing to the breaking of chemical bonds in the molecules of the clusters. The diamond-phase nuclei of several carbon atoms may appear directly after the shock-wave front, when the chemical reactions do not necessarily begin. In this case, the degree of the initial carbon-containing substance hybridization is of decisive importance [13].

Total mass of the nanocarbon

n	*m*, g	*N*, pulse
2	6.3	600
6	89.2	2000
10	198	3290
10–14	267	4500
11–20	448	6200

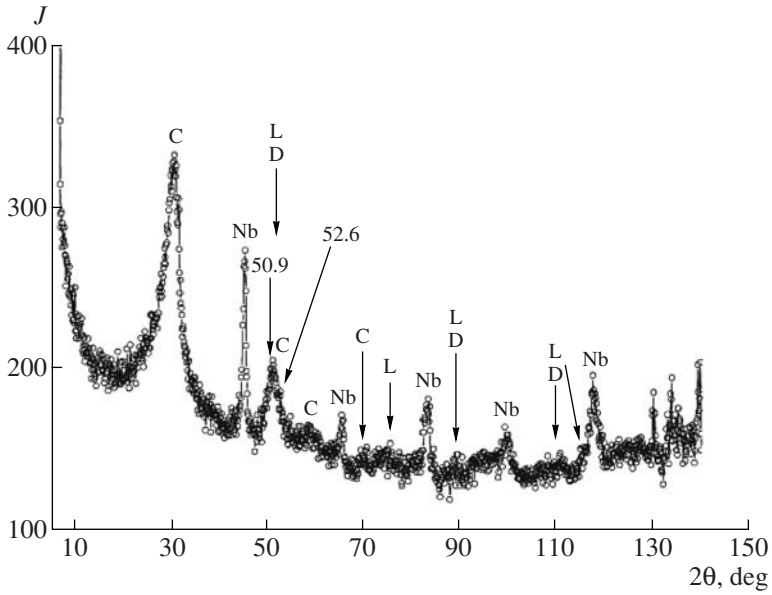

Fig. 9. Diffractogram of the nanocarbon material: *C* is the nanographite; *D* is the diamond; *L* is the lonsdaleite; and *Nb* is the substrate.

Although nanocarbon globules have nanodimensions (~200 nm), they are too large to be used in nanotechnologies. To eliminate this disadvantage in the future, applying a flow-type system for the electric-discharge treatment of organic liquids in small volumes with nanocarbon removal from the reactor zone is proposed. Nevertheless, in our opinion, this material may be applied in a number of technologies where the particle dimension is not so crucial.

CONCLUSIONS

The experimental investigations reported on here have demonstrated the possibility of the effective synthesis of nanocarbon in macroamounts for short time intervals at the electric-discharge influence on organic liquids. Nanodiamond and lonsdaleite in sufficient amounts are found in the nanomaterial composition, making it possible to consider this method promising and competitive against the other known methods: detonation and electric explosion.

The studied regularities of obtaining nanocarbon upon many-cycle electric-discharge treatment have shown significant changes in the material mass gain with an increasing number of cycles. The obtained nanocarbon mass strongly depends on the number of carbon atoms in organic liquids evolved in the plasma channel during one energy pulse and on the number of treatment cycles.

REFERENCES

1. Eletskii, A.V. and Smirnov, B.M., Fullerenes and Carbon Structure, *Uspekhi Fiz. Nauk*, 1995, no. 9, pp. 976–1009.
2. Harris, P., *Uglerodnye nanotruby i rodstvennye struktury* (Carbon Nanotubes and Related Structures), Moscow: Tekhnosfera, 2003.
3. Churilov, G.N., Review of Fullerene Obtaining Methods, *Materialy 2 Mezhregion. Konf. "Ul'tradispersnye poroshki, nanostruktury, materialy"* (Proceed. of the 2nd Interregion Conference "Ultradisperse Powders, Nanotubes, and Materials"), Kransnoyarsk, KSTU, 1999, pp. 77–87.
4. Mekalova, N.V. and Kuzeev, I.P., Method of Obtaining of Fullerenes C_{60} from Heavy Residues of Oil-Refinery, *XVI Mendeleevskii s'ezd po obshchei i prikladnoi khimii, posvyashchennyi 250-letiyu otechestevennoi khimicheskoi nauki* (XVI Mendeleev Conference on General and Applied Chemistry Dedicated to the 250th Anniversary of Home Chemical Science), St. Petersburg, 1988, part 2, p. 397.
5. Boguslavskii, L.Z., Guk, I.P., Kuskova, N.I., Khainatskii, S.A., and Shcherbak, A.N., Electric Explosion Method of Fullerene Obtaining, *Elektron. Obrab. Mater.*, 2002, no. 4, pp. 30–34.
6. Kingsuk Mukhopadhyay, Akira Koshio, Toshiki Sugai, Nobuo Tanaka, Hisanori Shinohara, Zoltan Konya, Janos B. Nagy, Bulk Production of Quasi–Aligned Carbon Nanotube Bundles by the Catalytic Chemical Vapor Deposition (CCVD) Method, *Chem. Phys. Lett.*, 1999, vol. 302, no. 1–2, pp. 117–124.
7. Anisichkin, V.F. and Mal'kov, I.Yu., Diamond Synthesis at Dynamic Loading of Organic Substances, *Dokl. Akad. Nauk SSSR,* 1988, vol. 303, no. 3, pp. 625–527.

8. Mal'kov, I.Yu., Filatov, L.I., Titov, V.M., et al., Diamond Formation from Carbon Liquid Phase, *Fiz. Goreniya Vzryva*, 1993, vol. 29, no. 4, pp. 131–134.

9. Vovchenko, A.I., Kucherenko, V.V., and Shamko, V.V., Peculiarities of Space–Time Evolution of Vapor–Gas Cavities Generated by Underwater Spark Discharge, *Zhurnal Priklandnoi Mekhan. Tekhn. Fiz.*, 1978, no. 6, pp. 58–64.

10. Krivitskii, E.V., *Dinamika elektrovzryva v zhidkosti* (Dynamics of Electric Explosion in Liquid), Kiev: Naukova Dumka, 1986.

11. Kuskova, N.I., Gordienko, V.I., Razmenov, E.P., and Khainatskii, S.A., Study of Possibility of Artificial Diamond Synthesis at Electric Explosion of Graphite Conductors in Liquid, *Elektron. Obrab. Mater.,* 2006, no. 3, pp. 153–160.

12. Vovchenko, O.I., Gorogyan, V.I., Kuskova, N.I., Razmenov, C.P., and Shvets', I.S., 77370 Ukraine Patent no. 200512866, *Byull.,* 2006, no. 3, p. 3.

13. Titov, V.M., Anisichkin, V.F., and Mal'kov, I.Yu., Study of Ultradisperse Diamond Synthesis Process in Detonation Waves, *Dokl. Akad. Nauk SSSR,* 1988, vol. 303, no. 3, pp. 117–126.

ISSN 1068-3755, Surface Engineering and Applied Electrochemistry, 2007, Vol. 43, No. 4, pp. 276–278. © Allerton Press, Inc., 2007.
Original Russian Text © V.M. Kosenkov, L.A. Kamenskaya, 2007, published in Elektronnaya Obrabotka Materialov, 2007, No. 4, pp. 53–56.

ELECTRICAL PROCESSES IN ENGINEERING AND CHEMISTRY

Estimation of the Influence of the Pulse-Load Parameter on a Decreasing Static Stress in a Steel Band

V. M. Kosenkov[a, b] and L. A. Kamenskaya[a]

[a] *Institute of Pulse Processes and Technologies, National Academy of Sciences of Ukraine, pr. Oktyabr'skii 43-a, Nikolaev, 54018 Ukraine*

[b] *Nikolaev Polytechnical Institute, ul. Nikol'skaya 11-a, Nikolaev, 54030 Ukraine*

Received December 4, 2006

Abstract—The theoretical study of the impact of the pulse-load characteristics on the relaxation of the residual stress in materials with the help of mathematical modeling is completed.

DOI: 10.3103/S1068375507040084

INTRODUCTION

Many technological processes are accompanied by the appearance of residual stresses in individual parts that most frequently lead to a decrease in the load-bearing ability and durability of constructions. The residual stress level decrease is an important practical problem, which can be solved using many methods. The most promising methods with regards energy resource expenditure are those that use no thermal operations. The pulse load of construction elements is one such method [1, 2].

In the studied processes, the relaxation of a deformed solid body occurs due to the pulse-load action on its surface; therefore, the aim of the present paper is to study the pulse influence on a stressed part and, in particular, to estimate the influence of the load parameters on its stressed-deformed state.

PROBLEM STATEMENT AND NUMERICAL EXPERIMENT RESULTS

The dynamic processes in the object of study were simulated on the basis of the equations of motion in stresses reflecting the relation between the stress-tensor components and motions [3]:

$$\rho_I \dot{u}_1 = \frac{\partial \sigma_{11}}{\partial x_1} + \frac{\partial \sigma_{12}}{\partial x_2} + \frac{\partial \sigma_{13}}{\partial x_3}, \quad (1)$$

$$\rho_I \dot{u}_2 = \frac{\partial \sigma_{21}}{\partial x_1} + \frac{\partial \sigma_{22}}{\partial x_2} + \frac{\partial \sigma_{23}}{\partial x_3}, \quad (2)$$

$$\rho_I \dot{u}_3 = \frac{\partial \sigma_{31}}{\partial x_1} + \frac{\partial \sigma_{32}}{\partial x_2} + \frac{\partial \sigma_{33}}{\partial x_3}, \quad (3)$$

where u_1, u_2, and u_3 are the motion velocities; x_1, x_2, and x_3 are the coordinates of the rectangular Cartesian system; ρ_M is the elastic-body material density; σ_{ij} is the stress tensor component ($i, j = 1, 2$, and 3); and $\sigma_{ij} = \sigma_{ji}$.

Stresses and deformations are interconnected by the generalized Hooke law [3–5]. Its expression in the tensor form is the following:

$$\dot{S}_{ij} = 2G\left(\dot{\varepsilon}_{ij} - \dot{\varepsilon}\frac{1}{3}\delta_{ij}\right), \quad \sigma_{ij} = S_{ij} - \sigma\delta_{ij}. \quad (4)$$

Here, S_{ij} ($i, j = 1, 2$, and 3) are the stress-deviator components; ε_{ij} ($i, j = 1, 2$, and 3) are the deformation-tensor components; σ is the hydrostatic-stress component found from the differential ratio $\dot{\sigma} = -K\dot{\varepsilon}$; ε is the volume deformation; and K is the volume-compression module.

The point above the symbols indicates a differentiation in time.

The deformation-tensor components are determined by Cauchy's formulae:

$$\dot{\varepsilon}_{11} = \frac{\partial u_1}{\partial x_1}, \quad \dot{\varepsilon}_{22} = \frac{\partial u_2}{\partial x_2}, \quad \dot{\varepsilon}_{33} = \frac{\partial u_3}{\partial x_3},$$
$$\dot{\varepsilon}_{13} = \frac{\partial u_1}{\partial x_3} + \frac{\partial u_3}{\partial x_1}, \quad \dot{\varepsilon}_{12} = \frac{\partial u_1}{\partial x_2} + \frac{\partial u_2}{\partial x_1}, \quad (5)$$
$$\dot{\varepsilon}_{23} = \frac{\partial u_3}{\partial x_2} + \frac{\partial u_2}{\partial x_3}.$$

The plastic-yield surface is specified by the yield condition by Huber von Mises [4–6]:

$$S_{11}^2 + S_{22}^2 + S_{33}^2 + 2(S_{12}^2 + S_{13}^2 + S_{23}^2) - \frac{2}{3}\sigma_T^2 \le 0, \quad (6)$$

where σ_T is the material-yield point.

If condition (6) is not realized, all stress-deviator components S_{ij} ($i, j = 1, 2$, and 3) must be corrected by

$$\sqrt{2/3}\,\sigma_T / \sqrt{S_{11}^2 + S_{22}^2 + S_{33}^2 + 2(S_{12}^2 + S_{13}^2 + S_{23}^2)}\,.$$

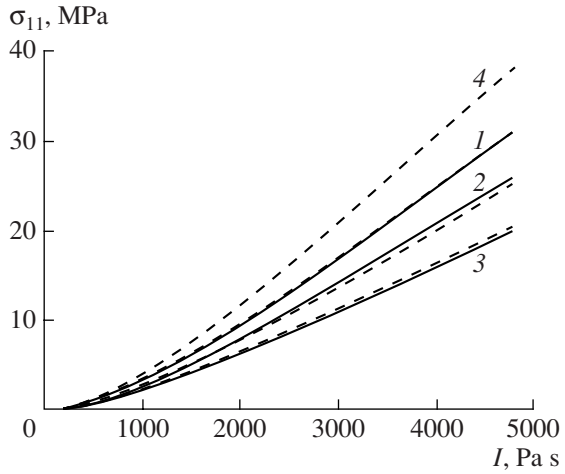

Fig. 1. Change in the average residual stresses. τ, μs: *1*, 10; *2*, 20; *3*, 40; and *4*, 5.

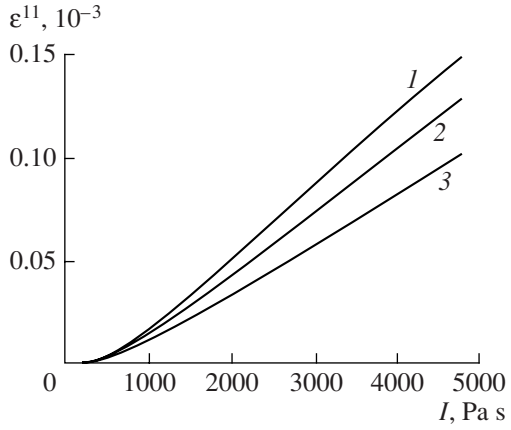

Fig. 2. Dependence of the average residual deformations on a specific pulse. τ, μs: *1*, 10; *2*, 20; and *3*, 40.

System of equations (1)–(6) is supplemented with corresponding initial and boundary conditions. For the elastic-body deformation process, it is convenient to specific the stresses on its surface. The stresses on the surface under a load are considered to be equal to the load pressure with an opposite sign and the stresses on the free surface are set equal to zero. On fixation circuits, the stresses are not calculated, because, here, the motions and velocities are obviously expressed using additional kinematic boundary conditions corresponding to the physics of the processes.

System of equations (1)–(6) was solved applying the numerical method described in [7]. Initial elastic-static stresses in the material produced by an uniaxial stretch were determined by the same method, calculating their values in time after a change of the controlled initial length of the body up to the value corresponding to the yield point.

The algorithm has been tested on model problems on the distribution of the pressure wave with a Π-like profile and with a shift wave in a solid body of the parallelepiped form. For a complex test of the influence of the normal and shift components of the stress tensor on the solid-body dynamic deformation, the problem of transverse-free oscillations of a beam with a rectangular cross section was solved.

The characteristic peculiarities of a pressure change on the surface of an object under study in time for the type of load considered, i.e., a wave of pressure from the electric discharge in water on the body surface, may be described using the exponential dependence

$$p = p_m e^{-\frac{t}{\tau}} f(x_1, x_2, t_0), \qquad (7)$$

where p_m is the pressure amplitude; τ is the pressure relaxation time, i.e., the characteristic discharge duration; $f(x_1, x_2, t_0)$ is the function of the pressure distribution over the body surface; and t_0 is the time it takes the wave to pass from the source to the specified point with the coordinates x_1 and x_2.

The load action on the body may be characterized by the pressure-pulse value on its surface:

$$I = \int_0^\infty f(x_1, x_2, t_0) p(t) dt = f(x_1, x_2, t_0) p_m \tau, \qquad (8)$$

where I, p_m, and τ may be used as the load parameters.

The object of the study is a narrow metal band of St3 steel with a yield point of 250 MPa, 360-mm long, 40-mm wide, and 4-mm thick. The control sector, where the deformation change was tested, was 180-mm long. The pressure on the band surface was determined using dependence (7). In it, the following function was used in place of $f(x_1, x_2, t)$:

$$f(x_1, x_2, t) = (\tilde{n}t - \sqrt{(x_1 - x_{10})^2 + (x_2 - x_{20})^2}) \times \frac{2\Delta r_0}{\Delta r_0 + \sqrt{(x_1 - x_{10})^2 + (x_2 - x_{20})^2}}, \qquad (9)$$

where x_{10} and x_{20} are the coordinates of the band-surface center; Δr_0 is the coefficient of the space relaxation of the pressure wave; χ is the Heaviside function; and c is the velocity of the pressure-wave front.

The band was subjected to an uniaxial stretch up to the yield point; afterwards, its corresponding end faces were rigidly fixed; then, it was subjected to the action of the pressure determined using functions (7) and (9). Then, on the control-band sector, a value of change of the average longitudinal stress $\Delta\sigma_{11}$ and average residual deformations ε_{11} in comparison with the yield point were determined. The results of the calculations are shown in Figs. 1 and 2 in the form of the dependences of the mentioned values on specific pulse I at various pressure

relaxation times τ in the range of 10–40 μs characteristic of the electric discharge in water. The value of specific pulse I shown in the figures is determined at a central point of the control-band sector ($x_1 = x_{10}, x_2 = x_{20}$). At this point, $f(x_1, x_2, t_0) = 1$; therefore, the specific pulse achieves its maximum value.

Analysis of the results allowed us to reveal the characteristic peculiarities of the load-parameter influencing the decrease in the longitudinal stresses and the value of the residual deformations.

The values of the stress change and of the residual deformations are equal to zero at any τ value, if the specific pulse is less than 300 Pa · s. As it increases, their values increase, and, as time τ increases, they decrease according to the power laws. When τ decreases from 40 to 10 μs, the value of $\Delta\sigma_{11}$ increases by 30%; for example, for a specific pulse of 2400 Pa · s, it changes from 8 to 12 MPa, i.e., from 3 to 4.5% in comparison with the yield point in the specified range of change.

The dependence of the average stress value (in MPa) on specific pulse and pressure relaxation times was approximated with an error not exceeding 2.5% in the range of change in I from 500 to 5000 Pa · s and in the range of the change in τ from 10 to 40 μs by the following power law:

$$\Delta\sigma_{11} = 1.3 \times 10^{-3}(I - 350)^{1.2}\left(\frac{10^{-5}}{\tau}\right)^{0.3}, \qquad (10)$$

It is seen from this analysis that the decrease of the residual stresses is proportional to the specific pulse value by a power of 1.2 ($\Delta\sigma_{11} \sim I^{1.2}$). The discharge duration is of significant interest. The residual stresses relax more rapidly with a decrease in time τ ($(\Delta\sigma_{11} \sim \tau^{-0.3})$). In Fig. 1, the dashed lines show the approximating curves. Extrapolation using formula (10) for a shorter time shows that, at a constant value of pulse I at with a decrease in τ from 40 to 5 μs, the value of the average stress change increases by about a factor of two.

CONCLUSIONS

On the basis of the numerical solution of the system of equations of elasticity theory, taking into account the material-plastic deformation, the characteristic peculiarities of the load-parameter influence on the process of a decreasing static-stress level are revealed. It is found that, for the realization of the process of stress redistribution in a stressed-deformed body, it is necessary to affect it by a pressure pulse exceeding 300 Pa s. Upon loading with a pressure having the pulse lower than the mentioned level, the stress relaxation processes in the material do not occur.

The dependences of the change in values for average residual stresses and deformations on the pulse and time of pressure relaxation are obtained.

Thus, we can conclude that, for the acceleration of the process of residual stress relaxation in the elements of steel constructions, it is necessary to reduce the load-action duration, while preserving the pulse value.

REFERENCES

1. Chachin, V.N., Bogoyavlenskii, K.N., and Vagin, V.A., *Elektrogydroimpul'snaya obrabotka materialov v mashinostroenii* (Electrohydropulse Treatment of Materials in Mechanical Engineering), Minsk: Nauka i Tekhnika, 1987.
2. Petushkov, V.G., *Primenenie vzryva v svarochnoi tekhnike* (Explosion Application in Welding Technique), Kiev: Naukova Dumka, 2005.
3. Sedov, L.I., *Mekhanika sploshnoi sredy* (Mechanics of Continuum), Moscow: Nauka, 1976, vol. 2.
4. Uilkins, M.L., *Raschet uprugoplasticheskikh techenii. Vychislitel'nye metody v hydrodinamike* (Calculation of Elastic Plastic Yields. Numerical Methods in Hydrodynamics), Moscow: Mir, 1967 pp. 212–263.
5. Kosenkov, V.M. and Kamenskaya, L.A., Mathematical Modeling of Stress Relaxation in a Metal Band under the Influence of Pressure Waves, *Trudy mezhdunarodnoi konferentsii. VII Kharitonovskie tematicheskie nauchnye chteniya "Ekstremal'nye sostoyaniya veshchestva. Detonatsiya. Udarnye volny"* (Proc. Int. Conf. VII Kharitonov Subject Scientific Reports "Extreme Substance States. Detonation. Shock Waves"), Sarov, RFYaTs–VNIIEF, 2005, pp. 457–462.
6. Mozharovskii, N.S., *Teoriya plastichnosti i polzuchesti v inzhenernom dele* (Theory of Plasticity and Creep in Engineering), Kiev: Vishcha Shkola, 1991, part 1.
7. Kosenkov, V.M. and Kamenskaya, L.A., Calculation of Electric Discharge Channel Broadening in the Liquid Described in the Potential Approximation, *Akustynchnyi Visnik*, 2001, vol. 4, no. 2, pp. 47–53.

ISSN 1068-3755, Surface Engineering and Applied Electrochemistry, 2007, Vol. 43, No. 4, pp. 279–286. © Allerton Press, Inc., 2007.
Original Russian Text © A.M. Romanov, V.I. Zelentsov, 2007, published in Elektronnaya Obrabotka Materialov, 2007, No. 4, pp. 57–65.

ELECTRICAL TREATMENT OF BIOLOGICAL OBJECTS AND FOODSTUFFS

Use of Electrodialysis for the Production of Grape-Based Soft and Alcoholic Drinks

A. M. Romanov and V. I. Zelentsov

Institute of Applied Physics, Academy of Sciences of Moldova, ul. Akademiei 5, Chisinau, MD-2028 Moldova

Received April 24, 2007

Abstract—A review on the electrodialysis application for the production of grape-based soft and alcoholic drinks is presented.

DOI: 10.3103/S1068375507040096

INTRODUCTION

An analysis of the recent production technology development of fruit and berry drinks, wines, and strong alcoholic drinks shows significant progress by fundamental science in the understanding of the main processes taking place in both traditional and modern technologies of drink production. Yet, numerous unsolved problems restrain the growing industrial demands. In particular, there is no reliable technology for drink treatment stabilization against crystal turbidity. The problems posed by modern industry can be solved on the basis of the existent process optimization as well as by developing principally new technologies, materials, and power sources. The development of principally new means to intensify and modernize contemporary technology through the use of electrochemical treatment techniques (already playing a substantial role in different industrial processes [1–3]) is one possible direction of the drink-quality improvement.

Electrodialysis is historically more developed and applied in the electrochemical separation processes due to its possibilities for ion-composition regulation in liquids as well as total salt-content reduction. At present, electrodialysis is widely used in the chemical, petrochemical, pharmaceutical, microbiological, nuclear, electronic, food, medical, water treatment, and other industries [4–9].

GENERAL CHARACTERISTICS OF THE ELECTRODIALYSIS PROCESS

Electrodialysis is a solution-treatment process in the direct electrical field. Here, the ions of the dissolved substances selectively pass the respective membranes. The electrodialysis refinement of liquid multicomponent systems is based on the ionized substance separation under the field-strength gradient produced in the solution at both membrane sides.

Note the difference between electrodialysis and the electro-electrodialysis (a process close to the former in its physicochemical properties and characteristics). During the process of the electro-electrodialysis (a two-section cell with a single membrane), ion migration through a permeable partition or an ion-selective membrane (cationite or anionite, or bipolar) under the electric-field action is accompanied by the oxidation-reduction reaction on the electrodes (one of the two is necessarily put into the treated liquid). In electrodialysis, the ion concentration change process takes the primary role; yet, electro-electrodialysis makes it possible not only to change the ion concentration due to the electrolysis process, but also to form (of principal importance) new products due to the oxidation-reduction reaction on the electrodes. In electrodialysis (at least a three-section cell with two membranes), the electrode zones are not in contact with the treated liquid (due to use of the membranes) and, thus, there is no electrolysis of the liquid, in contrast to other electrochemical techniques (electroflotation, electrocoagulation, etc.). In telectrodialysis, the electrode reactions are not engaged. Thus, it is a technique of "soft" impact on the ion composition of the product under treatment. Moreover, the electrodialysis treatment of drinks is often performed under an inert gas atmosphere to exclude any contact with oxygen air [10]. In the literature available, solitary papers published within the first half of the preceding century are presented on the electro-electrodialysis treatment of juices, musts, and wines aimed at regulating the total and volatile acidity and pH of the drinks [11, 12], as well as the present-day papers by Hiroshi Tanaka (Japan) on the artificial acceleration of young wine "aging" up to several seconds using the above technique [13]; another work is connected, in particular, with this use of electrode materials with a low hydrogen release during the process of wine treatment [14]. Yet, these works are not considered here, since they having no relation to the "pure" electrodialysis process.

Generally, electrodialysis facilities consist of a membrane (a set of membranes and separating filter-press frames), hydraulic (pumps, pipes, and valves),

and electric (rectifier, control panel, triggers, and signal devices) units.

The following two types of electrodialysis liquid treatment are used: periodical, where the drink is pumped through a membrane set within the closed loop until the preassigned concentration of the target product is obtained; and continuous, with the one-pass pumping of the treated liquid through the electrodialyzer. Both have certain merits and disadvantages; which one will be used is decided in each particular case taking into account the physicochemical characteristics of the treated drink as well as the construction and electrical parameters of the electrodialyzers.

DIFFERENT POSSIBILITIES FOR THE MUTUAL LOCATION OF MEMBRANES AND ELECTRODES IN THE ELECTRODIALYZER

The simplest electrodialyzer consists of three cells: the operating cell (here, the juice or wine treatment is performed) and the two electrolysis cells (here, the cathode and the anode are located and the electrolysis process takes the place of the used electrolyte) and two membranes. Yet, the three-cell electrodialyzer does not reproduce the industrial electrodialyzer with its hundreds of membranes, because the former is not supplied by cells with a flushing fluid to take or release the ions passing through the membranes under the action of the electrical current. Such a process can be primitively realized under laboratory conditions in a six-cell electrodialyzer including two desalting cells (to clear the operating food liquid), two concentrating cells (flushing fluids), and two electrolysis cells. In such an electrodialyzer, circulation takes the place of the three independent, nonmixed liquid flows: electrolyte, flushing fluid, and the food solution under treatment. Note the absence of the direct contact, inside the apparatus, of the treated food liquid with the electrodes, the electrolysis products, and with the chemicals used to prepare the flushing solutions.

Four different possibilities exist for mutual membrane-to-electrode arrangements in the electrodialyzer.

First, the anode cell is separated from the dialysis cell by an anion-selective membrane, whereas the cathode cell is separated by a cation-selective membrane. Here, under the electrode voltage, the anions will migrate from the dialysis cell to the anode cell, and the cations will migrate to the cathode cell. Thus, the ions from the electrode cells cannot penetrate into the electrodialysis cell. Hence, under such conditions, only the exhaustion of ions can take place in the operating dialysis solution with the simultaneous enrichment of the electrolyte in the anode and cathode cells.

The second arrangement is one in which the cation-selective membrane is located at the anode cell and the anion-selective membrane is located at the cathode cell. The negative ions can migrate into the dialysis cell from the cathode cell and positive ions can move from the anode cell. No ions can migrate from the electrodialysis cell, because they cannot penetrate through the likely charged membranes. Thus, in the electrodialysis cell, solution enrichment takes place with unlikely charged ions, whereas in the electrode cells, the exhaustion of positive and negative ions, respectively, takes in the electrolyte.

The third possibility consists in the use of only anion-selective membranes. Here, the exhaustion of anions takes place in the dialysis and the cathode cells and enrichment takes place in the anode cell. Under such conditions, the cations cannot penetrate through the membranes and are excluded from the migration process.

The fourth possibility consists in the use of only cation-selective membranes in the electrodialyzer. Here, the exhaustion of cations takes place in the dialysis and the anode cells and enrichment take place in the cathode cell. The anions cannot leave the cells.

The above argumentation only concerns electrodialysis with monopolar membranes (according to the charge occurring on the ion-exchanging membrane as a result of the electrolytic dissociation of the ion-exchange groups: monopolar cation exchange and monopolar anion exchange). Yet, numerous papers are available concerning the use of bipolar membranes (consisting of two layers, cation exchange and anion exchange, laminated together) combined with the monopolar membraines. In such cases, the electrodialysis patterns are much more numerous.

The purposeful use of the nature and alternation of the membrane and the electrode location makes it possible to control the must and wine pH and acidity, and the ion composition of the drinks; to remove the surplus ions of heavy metals, potassium, and calcium; to perform the must desulphitation; and also to correct wine defects to improve their organoleptic characteristics, etc.

MEMBRANES IN THE ELECTRODIALYSIS

The expediency of electrodialysis use in drink production was demonstrated under laboratory conditions in the 1960s. Yet, these works were not applied in industry. The delay in electrodialysis development was caused by the absence of highly efficient membranes for the wine and juice production industries.

For example, the requirements put to the membranes used for the tartrat wine stabilization are as follows [15]:

(i) the wine pH decrease should be within a 0.3-pH;

(ii) the acidity decrease should be below 0.12 g/l;

(iii) the content of the nonion wine components (in particular, polyphenols and polysaccharides) should not change;

(iv) diffusion of the lesser molecules (such as ethanol) should be negligible and should not cause an alcohol decrease in the wine above 0.1% (volume);

(v) the membranes should be cleaned using the substances authorized for application in foodstuff preparation;

(vi) the cation-exchange membranes should be selective and aimed at a preferable output of K^+ and Ca^{++} ions;

(vii) the anion-exchange membranes should be aimed at a preferable output of the tartrat ions;

(viii) the membranes should not significantly change the physicochemical composition and the sensor properties of the wine.

Generally, the membranes should meet the following requirements:

(i)They should be made of substances authorized for the production of polymer materials fit for use in the food industry.

(ii) During the process of dissolution, they should not discharge into the solution a quantity of a substance that is dangerous to the health of humans nor those influencing the product taste and smell.

(iii) When used, they should not have any chemical interaction with the juice and wine components, nor should they facilitate the formation of new compositions that can be toxic in the treated product.

(iv) They should possess a high selectivity and mechanical durability, a low permeability for water molecules, and a high electrical conductivity and chemical resistance.

USE OF ELECTRODIALYSIS IN JUICE PRODUCTION AND WINE MAKING

Recently, electrodialysis has been widely applied in the industrial treatment of water as a raw material for the food industry, in particular, in wine making and juice production. Here, we will not discuss this problem, but refer to a number of monographs [8, 9, 16] presenting indisputable evidence of the state-of-the-art in this field.

At the end of the 1960s and at the beginning of the 1970s, a set of papers appeared concerning electrodialysis treatment of a grape juice, where a number of problems was described to solve the use of the electrochemical technique. Here, K. Wucherpfennig et al. (Germany) demonstrated the possibility of applying electrodialysis to the tartrat stabilizing of a grape juice, and to increase and decrease the acidity of the juice and wine [17–19]. The grape juice stability was shown to be obtained by lowering the concentration of either the potassium ions or the wine acid anions—or both the potassium ions and the wine acid anions. To remove the acids, KOH solutions are proposed to serve as the flushing liquid, whereas to remove the mineral substances, it is best to use (citric) acid-containing flushing liquids. In such a case, the juice anions are substituted by hydroxyl ions and the cations are substituted by the hydrogen ions providing a total acidity regulation and a pH change. These results have been verified under industrial conditions at a large-scale laboratory facility containing 15 grape-juice chambers, with different arrangements of the Ren Pulerk membranes against the electrodes and with the use of different types of flushing liquids. Here, the juice acidity can be lowered from 7.6 g/l to 0.5 g/l, thus causing the pH to increase from 3.12 up to 5.23.

E.M. Shpritzman et al. (Moldova) [20] used an electrodialysis facility with two membrane combinations (first, only the MK-40 cation-exchange and the MA-40 anion-exchange membranes were used; second, a bipolar membrane was added) to stabilize a grape juice. The juice was treated under a current density of 6–8 mA/cm^3 and a specific facility productivity of 12–60 l/m^2 for the membrane per hour. The grape-juice tartrat stability was shown to take place at pH 3.2 and under potassium and tartratic acid contents of 1100 mg/l and 5.5 g/l, respectively. These limits are by convention named "the grape juice stability zone". A juice containing the tartratic acid and the potassium ions beyond the above limits is unstable against tartrat sedimentation. Yet, a component content below the above limits causes juice desalination and destroys its taste.

The results obtained on electridialysis juice treatment under laboratory conditions confirm the above values of the maximum potassium and tartratic acid content preceding the grape juice turbidity. Zelenskaya's studies [21] under industrial conditions at a tinned-food factory with the use of a standard electrodialysis facility with an alternate set of MK-40 and MA-40 membranes (200 chambers were used in each of the four in-series and in-parallel connected electrodialysis units) show that the stability of the grape juice against the tartrat sedimentation takes place at temperatures 0–2°C, pH 3.2–3.5, a potassium ion content of 900–950 mg/l, and a tartratic acid content of 5.5 g/l, thus being in agreement with the results of laboratory juice treatment under optimal process regimes.

Interesting works on grape juice stabilization [22–24] have been performed by Audinos et al. (France). Here, the physicochemical processes taking place in the tartrat stabilization of grape juice and wine with the use of mono- and bipolar membranes are described. Under laboratory conditions, a process of the simultaneous removal of the tartratic acid, alcohol, and metal ions (calcium, sodium, and iron) from the juice is studied. The quantity of the substances released is shown to depend on the electrical parameters and design particularities of the facility used. Then, the process of the ion-selective membrane contamination during the electrodialysis of juice and must treatment reducing their efficiency is studied [25]. The laboratory investigations show that the polyphenol drink substances are the main components contaminating the membranes.

In 1991, Audinos described the possibility of obtaining concentrated tartratic acid by use of the electrodialysis treatment of the secondary wine-making products containing the tartratic acid, using the following two variants [26]:

—using cation- and anion-exchange membranes and applying sulphuric acid and potassium bitartrat as the flushing liquids;

—using bipolar membranes combined with monopolar membranes and applying potassium bitartrate and KOH as the flushing liquids.

In the first case, the product was obtained with a tartrat acid content of 125 g/l, whereas in the second case, the content was 180 g/l (the initial potassium bitartrate content was 15 g/l for the two cases).

Escudier and coauthors demonstrated the expediency of using electrodialysis for grape must deionization, acidity reduction, and concentration increase [27]. Thus, the possibility of precise must composition preparation for fermentation, without the injection of any foreign chemical agents, occurred. Such electrodialysis must treatment before concentrating for the demineralization eliminates the danger of tartrat precipitation.

In Russia, Islamov and coauthors [28] proposed using organic complex-production solutions as the flushing liquids for electrodialysis to remove the heavy metal ions (negatively influencing the product quality and stability) from food liquids including grape juice. In particular, the use of Trilon B as the flushing liquid for electrodialysis grape juice treatment succeeded in the removal of 75–90% of the heavy metal ions. The remaining juice composition shows no appreciable variations.

Note that the use of the electrodialysis for grape juice composition regulation and its stabilization is not implemented in production quantities. In our opinion, this is caused by the absence, at that time, of high-quality ion-selective membranes as well as with the few works available in this field.

Yet, the majority of these investigations concern electrodialysis application to grape wine treatment. Of paramount importance is the problem of wine stabilization against tartrat. Boddy began pioneering studies in this field in 1970 in Italy [29]. In 1972, Shpritzman and colleague published the results of their study on lowering the potassium ion concentration in wine and model solutions using anion- and cation-selective membranes in different arrangements [30]. A dilute hydrochloric acid and a sodium chloride solution were used as the flushing liquids. First, the authors studied the potassium content decrease upon solution electrodialysis with different current amplitudes and similar impact durations. They showed that the potassium ion content decreases during the process of the electrodialysis wine treatment in agreement with the charge passed. Then, they noticed that the substitution of the potassium ions using hydrogen ions causes a decrease in the solution pH by 0.5. If the sodium chloride solution is used as the flushing liquid instead of hydrochloric acid, then a pH decrease can be avoided. Thus, with the help of electrodialysis, a precise quantitative regulation can be completed for the potassium content as well as the substitution of potassium ions by sodium ions.

In subsequent years, Wuperpfennig and coauthors in Germany [17–19, 31, 32] and Akopov in Russia [33] experimentally confirmed the possibility of electrodialysis wine stabilization against tartrat sedimentation. Based on these works, the conclusion can be made that, with the help of electrodialysis, the content of potassium ions and tartratic acid can be lowered up to the values desired. In addition, heavy-metal ions and sulfuric acid can be removed from wine.

Wuperpfennig and colleagues published a number of works aimed at the use of electrodialysis to regulate acidity (both, increase and decrease) in wine and other drinks. Also investigated were the main factors influencing the electrodialysis process, that is, the voltage, the order of the circulation of the operating and auxiliary liquids, etc. They treated different wines and juices in half-production quantities and showed the possibility of the continuous substitution of cations by hydrogen ions and of anions by hydroxyl ions for drink acidification and deoxidation. These works are now being successfully continued in Germany. For example, in 1999, Bach's paper was published on electrodialysis wine rectification [35]. Wines of 19 different brands, qualities, and origins were treated using electrodialysis to obtain tartrat stabilization; calcium, potassium, and magnium, in addition to potassium, were shown to be efficiently removed from these wines. No sensor changes were observed.

In France, papers [36–40] concerning the use of electrodialysis to treat grape must and wines were published. The results are presented on the tartrat stabilization of wines by electrodialysis treatment; the main principles of the technique are described as well as its economic aspects and prospects of application; the latter shows that potassium ions are extracted from the liquid in the first place. The organic acid ions are extracted faster from the must treated using adsorbents. The intensity of the extracted ion flow is significantly weakened if the demineralization degree (determined from the electrical conductivity decrease) is above 70–75%.

A number of works on electrodialysis wine stabilization is performed in Portugal [41–43]. Here, the efficiency of the wine stabilizing using the two technologies is compared: treatment by cold and by electrodialysis. The two technologies show nearly the same results concerning only the chemical and organoleptic parameters.

The electrodialysis process was too expensive to be applied commercially. Yet, in 1990s, French investigators in collaboration with Japanese membrane manufacturers established the electrodialysis process, applied it to wine stabilization, and made it efficient and economical. Between 1992–1998, the French

National Institute for Agricultural Research (INRA) in collaboration with Eurodia Industrie SA developed, based on modern advances in the ion exchange and membrane production fields, a technology of electrodialysis tartrat wine stabilization called STARS (Selective TArtrate Removal System) [44].

In 1997, commercial tests of electrodialysis technology were performed in France [10]. A facility with a productivity of 450 dl/hour with members of EURODIA and BOCCARD was put into operation from March through November, 1996 (the electrodialyzer worked with the use of an inert gas). A total 75 types of wine were treated during this period, with a total volume of 120,000 dl (white wines, 20%; rose wines, 22%; red wines, 58%). Here, the three regimes of electrodialysis wine treatment were applied, with a current amplitude of 10–17 A and voltage of 20–45 V.

The tests show that the use of electrodialysis causes changes in the pH, tartratic acid concentration, free SO_2, total SO_2, CO_2, Fe^{3+}, and other parameters, thus providing for tartrat wine stabilization. The organoleptic wine estimation after electrodialysis treatment did not show any principal difference from the untreated wines. Moreover, in most cases, the wines after electrodialysis treatment had improved organoleptic characteristics. According to the authors' calculations, the cost of the electrodialysis wine treatment was 1.2 to 1.6 times lower than the same for the contact processes (depending on the treated material volume).

Since the end of 2003, Eurodia has delivered special electrodialysis equipment that operates successively at wine-making factories in France, Italy, Spain, Australia, and the USA. The STARS system is shown to have the following advantages against the cooling process:

—It does not remove other wine components, except for the tartrat ions.

—It has less of an impact on the sensoric wine properties (no negative influence on the taste and race of wine).

—It possesses an abrupt cut in energy consumption (the energy resource cost is five to six times lower than the same needed for cooling).

Yet, as far as strong grape-based drinks are concerned, in the cognac industry, only solitary works are available on electrodialysis cognac treatment (in the strong drink industry, electrodialysis is predominantly used for water demineralization [8, 12]). In Moldova, Romanov and colleagues studied certain physicochemical regularities in the process of electrodialysis metal removal from cognac, optimizing the main electrical, electrochemical, and hydrodynamic parameters of the content reduction of the heavy metal and calcium ions [45, 46].Recommendations were developed to obtain stable positive results when using electrodialysis facilities for cognac demetalization under industrial conditions. Note that strong alcoholic drinks with a spirit content of 15–50% (volume) have a low electrical conductivity. Thus, when electrodialysis treating these systems, special tricks should be employed (the establishment of additional electrode pairs within the membrane set; the use of granulated ion-exchange resins as a backfilling between the membranes; the use of an ion-conducting spacer in the intermembrane volume, etc.).

INFLUENCE OF ELECTRODIALYSIS TREATMENT ON GRAPE JUICE AND WINE QUALITY

Each drink treatment is aimed at the removal of nonstable or excess components in quantities providing for stabilization and taste improvement. In every case, the impact on a drink causes a change in its composition. This is true for both traditional techniques (treatment by cold, by brightening and fining agents, by chalk, by sulphitation, etc.) and for electrodialysis. The problem is as follows: how deep is the change in the substance composition governing the quality and the biological value of the drink. Electrodialyzer construction is conditioned by the use of different materials: membranes, separators, frames, electrodes, etc. During drink production, the substances can transfer from the facility to the output product. Yet, in the electrodialysis process, only surface contact takes place for large product masses with a small surface of the above materials; thus, there is no possibility for these material solutions in quantities large enough to pose a threat to consumers' health. The following changes were analyzed [47–55] in juices and wines after electrodialysis treatment: the concentration of the primary, secondary, and tertiary amines; and the sum of the migrating organic substances with double and conjugated bonds; the total content of sugars, nonvolatile organic acids, tanning, colorant, and aromatic agents and ethanol, colloids, amino acids, mineral substances, in particular, calcium, magnesium, and copper. In addition to the integral characteristics, the content of the monomers used in the ion-exchange resin production (ethylchlorohydrine, polyethylenepolyamine, divinylbenzol, styrene), as well as the formaldehyde being the product of the polyethylene destruction, was determined in the extracts.

The chemical, sanitation, and physiological studies of juices and wines under laboratory and industrial conditions after electrodialysis treatment performed in a number of European countries showed that no taste or smell changes take place in the product and there is no ground for anxiety [55].

In 2000, at the 40th Session of the International Organization of Wine Makers in Paris with participants from 25 countries, a decision was made on the advisability of the application of the electrodialysis membrane for wine improvement and stabilization and the technique was recommended for used in practice (the following countries voted for the decision: Algeria, Australia, Austria, Belgium, Cyprus, Finland, France, Moldova, Morocco, Portugal, Russia, Spain, Sweden, the Netherlands, Tunisia, Uruguay, USA, Yugoslavia) [56].

The International Organization of Vine and Wine pronounced the electrodialysis process to be "a progressive experience" and authorized it for commercial use within the EU for treatment of all types of wines [44].

CONCLUSIONS

An analysis of the literature available on the application of electrodialysis in winemaking and juice production shows that electrodialysis technologies and facilities are gaining an ever-increasing importance. The implementation of this electromembrane technology became possible due to the development of polymer science, the use of synthetic polymer membranes, the improvement and modification of technology, the revelation of the main regularities in the interconnection of their structural characteristics, and the service conditions with the properties governing the transmembrane transfer.

In conclusion, we point out certain particular problems of electrodialysis drink treatment to which the solution will, to our mind, extend the possibilities and fields of application of this interesting and useful electrochemical process.

1. The use of electrolysis without gas release using bipolar membranes [57].

In common water electrolysis into hydrogen and oxygen, up to half of the energy consumption is spent on gas production.

2. The use of a pulsed current in electrodialysers. The pulsed-electrodialysis regime will make it possible to obtain a much higher operating current density compared with the stationary regime and, thus, to increase facility productivity. Note that, under the nonstationary electrodialysis regime, electrical power consumption will significantly decrease.

3. The wide application of reversible electrodialysis, which is the reverse of the cleaned liquid flow due to a change in the electrical field polarity, thus preventing sedimentation at the membrane surface.

4. The establishment of a new generation of electrodialysis facilities, in particular, with the use of modern electrode materials and reversible current suppliers will reduce the risk of sedimentation of insoluble salts on the membrane surface and, thus, increase the membrane serviceability in facilities.

5. To validate electrodialysis combination with other efficient processes, that is, with nanofiltration, ion exchange, etc.

6. The development of a new generation membrane set with a strongly predetermined structure will make it possible, under the selection of separation regimes, to raise their permeability and selectivity against the target components and to achieve the stability of their functional characteristics.

REFERENCES

1. Efendiev, O.F. and Chizhikov, V.I., *Elektroobrabotka zhidkostei v pischevoi promyshlennosti* (Electrical Treatment of Liquids in Food Industry), Moscow: Pischevaya Promyshlennost', 1977.
2. Romanov, A.M., Drondina, R.V., Matveevich, V.A., Syrbu, V.K., and Khmel'nitskaya, T.M., *Ochistka podzemnykh vod ot toksichnykh komponentov elektrokhimicheskimi metodami* (Underground Water Rectification by Electrochemical Methods), Chisinau: Shtiintsa, 1988.
3. Granovskii, M.G., Lavrov, I.S., and Smirnov, O.V., *Elektroobrabotka zhidkostei* (Electrical Treating of Fluids), Leningrad: Khimiya, 1976.
4. Grebenyuk, V.D., *Elelktrodializ* (The Electrodialysis), Kiev: Tekhnika, 1976.
5. Grebenyuk, V.D. and Ponomarev, M.I., *Elektromembrannoe razdelenie smesei* (Electro-Membrane Separation of Mixtures), Kiev: Naukova Dumka, 1992
6. Kul'skii, L.A., Grebenyuk, V.D., and Savluk, O.S., *Elektrokhimicheskie protsessy v vodopodgotovke* (The Electrochemical Processes in Water Treatment), Kiev: Tekhnika, 1987.
7. *Tekhnologicheskie protsessy s primeneniem membran* (Technological Processes with Membrane Application), Leycy, R, and Lab, S., Eds., Moscow: Mir, 1976.
8. Bryk, M.T., Tsapyuk, U.A., and Tverda, A.A., *Membrannaya tekhnologiya v pischevoi promyshlennosti* (Membrane Technology in the Food Industry), Kiev: Tekhnika, 1990.
9. Vurdova, N.G. and Fomichev, V.E., *Elektrodializ prirodnykh i stochnykh vod* (Electrodialysis of Natural and Waste Waters), Moscow: ACB, 2001.
10. Biau, G. and Siodlak, A. Conception, realization et utilization d'une unite industrielle de stabilization tartrique. *Revue Francaise d'Oenologoe*, 1977, no. 162, pp. 18–20.
11. Panashesku, I.S., Botoshanskii, M.M., Negru, A.I., and Romanov, A.M., State-of-the-Art and Prospects of Techniques of Electrical Treatment of Foodstuffs, *Elektronnaya obrabotka materialov* (Surface Engineering and Applied Electrochemistry), 1984, no. 2, pp. 80–84.
12. Skurikhin, I.M., *Khimiya kon'yachnogo proizvodstva* (Chemistry of the Cognac Production), Moscow: Pishchevaya Promyshlennost', 1968.
13. Tanaka Hiroshi, Jpn. Patent 2004-073056, *Patent Abstracts of Japan*, March 11, 2004.
14. Ageeva, N.M., Dribinskii, A.V., Loshkarev, G.L., and Lukovtsev, V.P., RF Patent 2 064 015, MKI C12H1/02, *Byull. Izobret.*, no. 20, publ. July 20, 1996.
15. Escudier, J.-L., New Physical Techniques for the Treatment of Wine: Electrodialysis, *Vinidea.net-Wine Internet Technical J.*, 2002, no. 4, article 4 of 5.
16. Ryabchikov, B.E., *Sovremennye metody podgotovki vody dlya promyshlennogo i bytovogo ispol'zovaniya* (Modern Techniques of Water Treatment for Industrial and Consumer Use), Moscow: DeLi Print, 2004.
17. Wucherpfennig, K., *Allg. Deutsche Weinfachz.*, 1974, no. 26, p. 681.
18. Wucherpfennig, K., Die Verhinderung der Weinsteinnausscheidung beim Konzrntrieren von Traubensaft mit

Hilfe der Elektrodialyse, *Flussiges Obst.*, 1974, vol. 41, no. 6, pp. 226–235.

19. Wucherpfennig, K. and Bretthauer, G., Uber den Einfluss einer Elektrodialysebenhandlung auf die Aromastoffe vom Wein, *Wein-Wissenschaft*, 1975, vol. 30, no. 2, pp. 61–81.
20. Shpritzman, E.M., Gavrilyuk, V.S., Popovskii, V.G., and Zelenskaya, M.I., Use of the Electrodialysis for the Tartrate Stabilization of Grape Juice, *Konservnaya i ovoshchesushil'naya promyshlennost'* (The Packing & Vegetable Drying Industry), 1976, no. 4, pp. 15–17.
21. Zelenskaya, M.I., The Electrodialysis Technique of the Grape Juice Tartrate Stabilization, *Konservnaya i ovoshchesushil'naya promyshlennost'* (The Packing & Vegetable Drying Industry), 1982, no. 10, pp. 34–36.
22. Audinos, R. and Roson, J.P., Etude de quelques parameters de l'electrodialyse utilize pour eliminer certains composant du vin et de jus de raisin, *Congress Mediteraneau de chimique. Manifestation 204 de la Federation Europienne de genie Chimique. Sociedat Espanola de Quimica Industrial, Barselona*, 1978.
23. Audinos, R. and Roson, J.P., Application de l'electrodialyse a l'eliminati on de certains composant du jus de raisin et du vin. Esas de laboratoire, *Connas. Vigne et Vin,* 1979, vol. 13, no. 3, pp. 229–239.
24. Audinos, R., Lurton, L., and Moutounet, M., Advantage of Electrodialysis to Produce Sweetening Products from Grape, *Sci. Alim.*, 1985, vol. 5, pp. 619–637.
25. Audinos, R., Fouling of Ion-Selective Membranes During Electrodialysis of Grape Must, *J. Membr. Sci.*, 1989, vol. 41, pp. 115–126.
26. Audinos, R. and Paci, S., Deux procedes Electromembranaires pour obtenir des solutions d'acide tartrique pur concentre. Electrochimie et Environnement. *Journees d'etudes, 17–18 avril, 1991*, Ecole Superieure d'Electricite a Gif-sur-Yvette, pp. 61–63.
27. Escudier, J.-L., Moutounet, M., Bariller, J.-M., Benard, P., Couttereau, Ph., Audinos, R., and Daumas, C., *Reu. Fr. Uenol.,* 1985, vol. 25, no. 99, pp. 39–44.
28. Islamov, M.N., A New Method of Heavy Metal Removal from the Food Liquids, *Khimicheskii problemy pischevoii tekhnologii* (Chemical Problems of Food Technology), Proc. Regional R&D Workshop, Krasnodar, 1990, p. 118.
29. Boddi, V., *Brevet Italien* no. 9760 A/70 du 25 Nov., 1970.
30. Shpritzman, E.M., Shapiro, B.S., and Andreev, V.V., Regulation of the Wine Ion Composition by the Electrodialysis. *Sadovodstvo, vinogradarstvo i vinodelie Moldavii* (Horticulture, Wine-Growing, and Wine-Making in Moldavia), 1972, no. 3, pp. 26–30.
31. Wucherpfennig, K., Possibilites d'application de procedes utilisant des membranes pour la stabilization des vines. (Ultrafiltration, osmose inverse, electrodialyse). *Ann. Technol. Agr.*, 1978, vol. 27, no. 1, pp. 319–331.
32. Wucherpfennig, K. and Millies, K.D. Uber den Einfluss der Elektrodialysebehaudlung auf den Schwermetallgehalt von Weinen, *Weinberg und Keller*, 1976, vol. 23, no. 6, pp. 241–256.
33. Akopov, R.A., Tokhmanchi, N.S., Lozovik, G.Ya., and Saldadze, K.M., *Vinodelie i vinogradarstvo SSSR* (Wine-Making and Wine-Growing in the USSR), 1975, no. 7, pp. 16–20.
34. Wucherpfennig, K., *Bull. OIV*, vol. 53, no. 589, pp. 187–208.
35. Bach, M.-P., Scholten, G., and Friedrich, G., Tartrat Stabilization with Electrodialysis in Comparison to the Contact Process, *Wein-Wiss.,* 1999, vol. 54, no. 4, pp. 143–156.
36. Escudier, J.-L., Saint-Pierre, B., Batlle, J.-L., and Moutounet, M., Fr. Patent 2 709 308-A1, 1993.
37. Moutounet, M., Escudier, J.-L., and Saint-Pierre, B., L'electrodialyse, adaptation a la stabilization tartrique des vins, *Les acquisitions recents dans les traitments physiques du vin*, Lavoisier Tec. And Doc., 1994, Paris, pp. 103–115.
38. Saint-Pierre, B., Batlle, J.-L., Escudier, J.-L., and Moutounet, M., Obtention de la stabilite tartrique des vins au moyen d'un procede d'electrodialyse controle, *Proc. 5th Symp*. Int. d'Oenologie, Bordeaux, France, 1995.
39. Saint-Pierre, B., Batlle, J.-L., Escudier, J.-L., and Moutounet, M., Electrodialysis Principle, Tech. Aspects are Discussed. Oenol., *95 Symp. Int. Oenol. 5th*, 1995 (publ. 1996).
40. Escudier, J.-L., Moutounet, M., Saint-Pierre, B., and Batlle, J.-L., Stabilization tartrique des vins par membranes: resultants et developments technologiques, *Proc. 11th Coloque Viticole et Oenologique*, Montpellier, France, 1997.
41. Strathman, H., Electrodialysis, Bungay, P.M., Lonsdale, H.K., and Pinho, M.N. (Eds.), *Synthetic Membranes: Science, Engineering and Applications,* NATO Asi. Series C: Mathematics and Chemical Sciences. Reidel Publishing Company, 1986.
42. Cameira dos Santos, P.J., Pereira, O.M., Goncalves, F., Tomas Simoes, J., and Pinho, M.N., Ensaios de estabilizacao tartarica em vinhos portugueses: Estudo comparative da electrodialise e de um metodo traditional, *Ciencia Tec. Vitiv.*, 2000, vol. 15, no. 2, pp. 95–108.
43. Goncalves, F., Cameira dos Santos, P.J., Barros, P., Pinheiro, J.A., and Pinho, M.N., Application de l'electrodialyse a la stabilization tartrique de vin Porto. Comparison avec le procede de froid par stabilization longue, *Proc. 6th Symp. Int. d'Oenologie, Bordeaux, France, Oenologie 99*, Paris, 1999, (Coord. Aline Lonvaud-Funel: 535–539, Ed. Tec. And Doc.).
44. Blackburn, D. and DiManno, C., New Choise for Tartaric Stability, *Practical Winemaking*, 2004, January/February, pp. 70–74.
45. Leva, S., Baraboi, B., Romanov, A., and Romanov, V., Fr. Patent MD 2310 G2, *Brevet de inventie*, 2003, November, 30.
46. Romanov, A.M., Leva, S.G., Zelentsov, V.I., Romanov, V.M., and Baraboi, B.M., Electrodialysis Cognac de-Metallization Aimed at Stabilization, *IV Int. Exhibition & Conference "Wine-Growing and Ecology,"* February 3–5, 2005, Odessa, p. 113.
47. Postel, W. and Prasch, E., Untersuchungen zur Weinsteinstabilisierung von Wein durch Elektrodialyse. I. Mitteilung: Absenkung der Kalium- und Weinsauerekonzentration zur Erzielungder Weinsteinstabilitaet, *Weinwirtsch. (Neustadt/Wstr.)*, 1977, vol. 113, pp. 1277–1283.
48. Postel, W. and Prasch, E., Untersuchungen zur Weinsteinstabilisierung von Wein durch Elektrodialyse. II. Mitt. Ein-

fluss verschiedener Verfahrensparameter, insbesondere der eleltrischen Stromstaerke und der Behandlungsdauer, *Weinwirtsch. (Neustadt/Wstr.)*, 1977, vol. 113, pp. 1410–1415.

49. Postel, W. and Prasch, E., Untersuchungen zur Weinsteinstabilisierung von Wein durch Elektrodialyse. III. Mittielung, Veraenderungen der Weininhaltsstoffe, *Weinwirtsch. (Neustadt/Wstr.),* 1978, vol. 114, pp. 28–32.
50. Postel, W. and Prasch, E., Untersuchungen zur Weinsteinstabilisierung von Wein durch Elektrodialyse. IV. Mitt.: Einfluss auf die kationischen Mineralstoffe des Weines, *Weinwirtsch. (Neustadt/Wstr.),* 1978, vol. 114, pp. 122–126.
51. Postel, W. and Prasch, E., Untersuchungen zur Weinsteinstabilisierung von Wein durch Elektrodialyse. V. Mitteilung: Einfluss auf die organischen und anorganischen Saeuren des Weines, *Weinwirtsch. (Neustadt/Wstr.)*, 1978, vol. 114, pp. 229–235.
52. Postel, W., Prasch, E., and Ziegler, L., Untersuchungen zur Weinsteinstabilisierung von Wein durch Elektrodialyse. VI. Mitteilung: Einfluss auf die Stickstoffsubstanzen des Weines, *Weinwirtsch. (Neustadt/Wstr.),* 1978, vol. 114, pp. 508–513.
53. Postel, W., Prasch, E., and Ziegler, L., Untersuchungen zur Weinsteinstabilisierung von Wein durch Elektrodialyse. VII. Mitteilung: Einfluss auf die fluechtigen Substanzen und phenolischen Verbindungen, *Weinwirtsch. (Neustadt/Wstr.)*, 1978, vol. 114, pp. 636–641.
54. Wucherpfennig, K. and Badior, S., Vergleichende sensorishe Beuzteilung von Weinen die mit Hilfe verschiedener verfahren gegen Weinsteiausfall stabilisiert wurden, *Weinberg und Keller*, 1976, vol. 23, no. 10, pp. 407–418.
55. Zelenskaya, M.I., Soboleva, I.M., and Kodner, M.S., Influence of the Electrodialyse Treatment on the Grape Juice Quality, *Vinodelie i vinogradarstvo SSSR* (Wine-Making and Wine-Growing in the USSR), 1983, no. 4, pp. 20–22.
56. Sous-Comission Conventionnelle d'Unification des Methodes d'Analyse et d'Appreciation des Vins. 40th Session, *Bulletin de l'OIV*, 2000, no. 3, pp. 611–658.
57. Strathman, H, Kroll, J.J., Rapp, H.-J., and Eigenberger, G., *J. Membr. Sci.*, 1997, vol. 125, p. 123.

ISSN 1068-3755, Surface Engineering and Applied Electrochemistry, 2007, Vol. 43, No. 4, pp. 287–290. © Allerton Press, Inc., 2007.
Original Russian Text © O.Yu. Shitik, V.I. Osipenko, D.O. Stupak, 2007, published in Elektronnaya Obrabotka Materialov, 2007, No. 4, pp. 66–70.

EQUIPMENT AND INSTALLATIONS

Technique for the Determination of a Wire-Electrode Tool Shift Value During the Process of the Conical Four-Coordinate Electroerosion Treatment

O. Yu. Shitik, V. I. Osipenko, and D. O. Stupak

Cherkassy State Technological University, bul. Shevchenka 460, Cherkassy, 18006 Ukraine

Received December 20, 2006

Abstract—The problems of obtaining an exact conical surface of workpieces as a result of the displacements of the wire-electrode tool (WET) during the process of treatment from a specified position are explored in this paper. The method of determination and correlation of the real position of the cutting-wire area electrode is developed, forming the necessary inclination angle and obtaining exact conical surfaces.

DOI: 10.3103/S1068375507040102

INTRODUCTION

At the modern stage of technological development, the branch of electroerosion wire cutting takes the leading positions in the field of the precision treatment of current conducting materials.

The requirements regarding the precision of workpiece fabrication are within strict bounds, from 10 to 2 μm. Under these conditions, a significant influence on final precision of the cutting process is exerted by such a specific tool as a wire electrode, especially in terms of obtaining complex conic surfaces.

The problem consists in the complexity of a precise formation of the conic surface of a workpiece at the motion of feed drives along a projected trajectory as the result of shifts in the wire-electrode tool (WET) from a calculated position during the process of formation of a specified inclination angle [1, 2].

As a rule, for the solution of the given problem, the modern leaders (AGIE, Sodick, Mitsubishi, etc.) apply complex multiaxial systems of sensors, which, in the real-time mode, register any deviation of the wire and transfer the obtained data to the base of a system of numerical controls (NC) for the machine, allowing for the determination of both the wire inclination angle and the cutting-wire sector shift with respect to its specified position [3, 4]. Thus, it is possible to correct the trajectory of motion of the machine feed drives and, therefore, to provide a precision of the geometry of the final product.

However, taking into account the high cost of the given control systems, both the modernization and improvement of the characteristics of the electroerosion cutting machines (EECMs) made in the countries of the Commonwealth of Independent States and the development of domestic EECMs are possible provided inexpensive, maximally simple, and efficient techniques for the determination of a real WET position are developed.

THEORETICAL ANALYSIS

Figure 1 shows the scheme of a workpiece treatment with the purpose of obtaining a figure of the conical form.

Upon the formation of the specified inclination angle of the wire, as a result of the availability of the intrinsic hardness of the electrode tool, a bend in the wire axis appears, which, in the general case, takes on a wavy form. This bend leads to the appearance of the shift value $\Delta\gamma$ at each point of contact of the wire-electrode tool and the treated workpiece.

The essence of the specified problem consists in the determination of the shift value of the WET working part points from a calculated position. For the solution to this problem, it is necessary to find only two values for $\Delta\gamma$: $\Delta\gamma_{upp}$, which is the deviation in the upper plane of the workpiece; and $\Delta\gamma_{low}$, which is the deviation in the lower part; the error $\Delta\alpha$ corresponding to them (Fig. 2) should also be determined.

Having determined the values $\Delta\gamma_{upp}$ and $\Delta\gamma_{low}$, it is not difficult to find the error of the specified inclination angle of WET: a change in the inclination angle and a shift of the cutting-wire sector result in the appearance of significant errors of the obtained workpiece geometry.

Under these conditions, for the improvement of the technical-economic characteristics of the electroerosion machine and for the solution of industrial problems, it is necessary to develop and introduce special techniques, which would allow us to provide treatment precision, taking into account the WET deviations from the nominal position, on the one hand, and to make the entire industrial process cheaper, on the other hand.

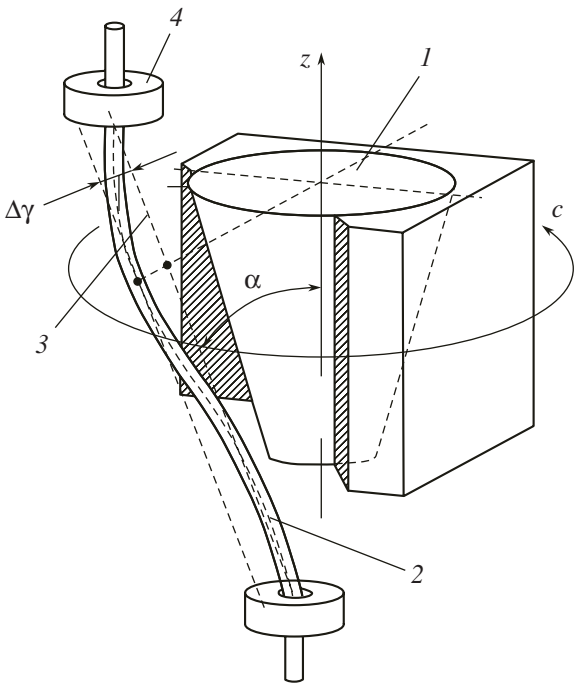

Fig. 1. Scheme of the treatment of conical surfaces by virtue of a four-coordinate electroerosion machine: *1* is the treated workpiece; *2* is the wire-electrode tool; *3* is the theoretical position of the WET axis; *4* is the system of the WET guiding; α is the specified inclination angle of the WET axis with respect to the workpiece surface; Δγ is the value of the WET shift with respect to the initial position at the point of contact with the workpiece; and *c* is the direction of motion of the electrode wire around the *z* axis.

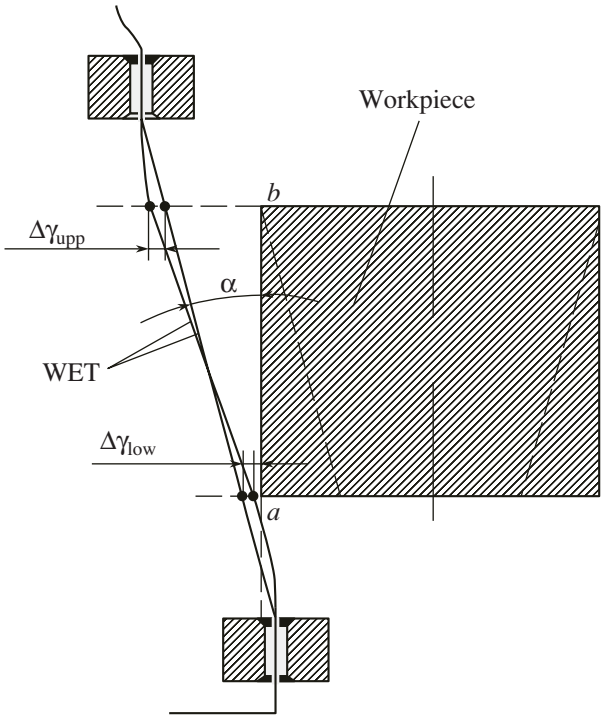

Fig. 2. Scheme of the shift of the initial WET position at extreme points of contact of the electrode and the workpiece: $\Delta\gamma_{upp}$ is the deviation value at the upper point of the contact; and $\Delta\gamma_{low}$ is the deviation value at the extreme lower point of the contact.

MEASUREMENT TECHNIQUE

In the firm "Aramis" (Cherkassy), on the basis of an essentially new four-coordinate electroerosion cutting machine *SELD-04* on linear drives, for the first time, a series of experimental measurements was carried out with the purpose of determining a precise position of a wire-electrode tool with respect to the workpiece at its conical cutoff.

The universality of the given method consists in the application of a specially designed device that imitates the treated workpiece. A characteristic peculiarity of the device is that it allows us to specify an arbitrary position of both base planes of treatment and wire inclination angles.

Directly before each experiment, all necessary measurements on the setting of the device with respect to the machine feed drives were carried out (Fig. 3).

At the first stage, the values l_1, l_2, and L were determined (Fig. 4).

The machine feed drives were positioned by virtue of NC, so that the front (cutting) edge of the WET in the point of the lower fixation of the wire in guide x_0 coincides with the ab axis of the rigidly fixed device. The WET fixation point in the upper guide was positioned from the ab axis at distance H determined by the NC system for the formation of the specified angle value α. Thus, knowing all of the necessary distances and dimensions, the following equalities may be determined:

$$H = L\tan\alpha, \tag{1}$$

$$\tan\alpha = \frac{H}{L} = \frac{H_1 - h_1}{l}, \tag{2}$$

$$H_1 = (l_1 + l)\tan\alpha, \tag{3}$$

$$h_1 = l_1\tan\alpha. \tag{4}$$

At the next stage, the machine feed drive shifted the lower guides into the point of the WET contact with the lower-end face of the device (Fig. 5). All of the coordinates of the shifts of the feed drives were registered by the machine NC.

In this case,

$$h_{1D} = x_1 - x_0. \tag{5}$$

Having symmetrically shifted the upper guides by the value –H and the lower guides into the point of the

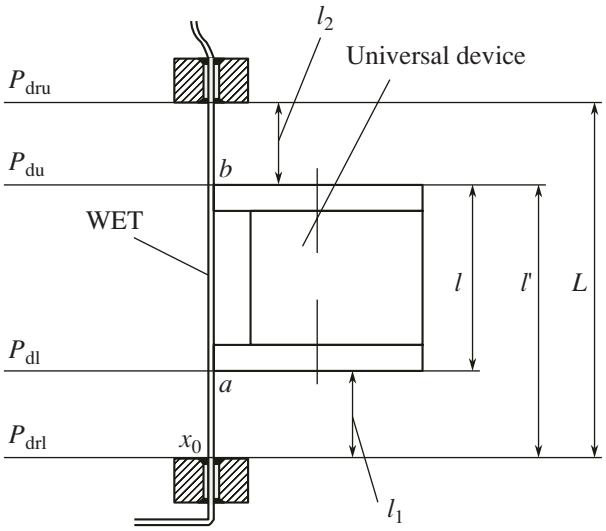

Fig. 3. Example of a scheme of a universal device setting on the four-coordinate electroerosion cutting machine SELD–04: P_{dru} is the upper plane of the drive motion; P_{du} is the upper plane of the device; P_{dl} is the lower plane of the device; P_{drl} is the lower plane of the drive motion; l_1 is the distance between the lower plane of the device and the lower plane of the drive motion; l_2 is the distance between the upper plane of the drive motion and the upper plane of the device; l is the device height; and L is the distance between the upper and the lower planes of the drive motion.

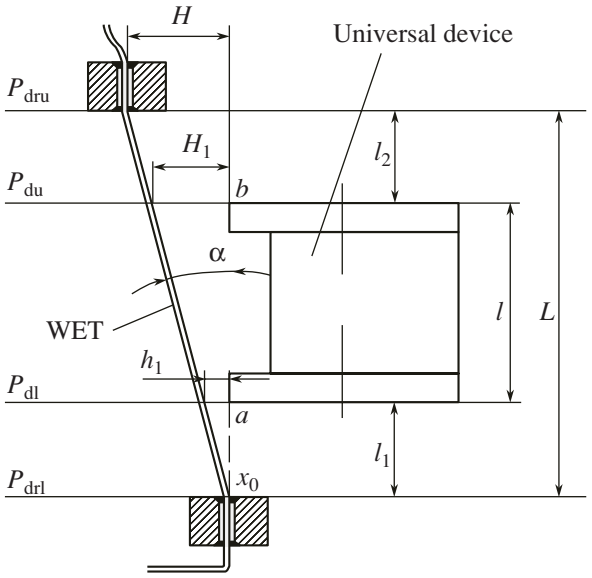

Fig. 4. Scheme for the determination of the WET position upon the formation of the inclination angle.

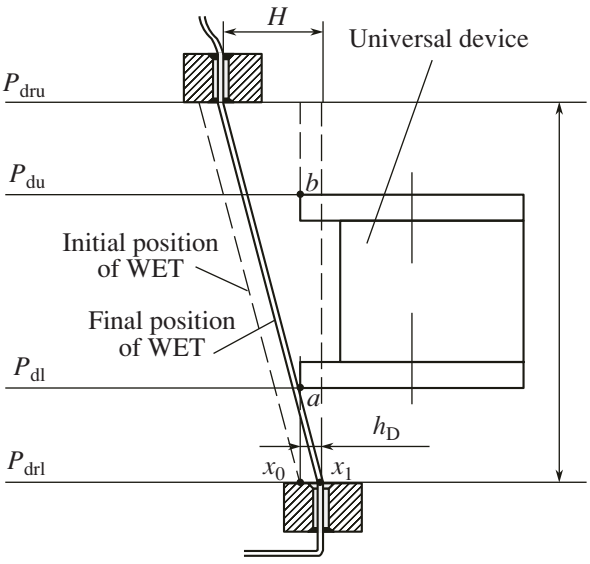

Fig. 5. Scheme of the determination of the real value of the WET shift h_D: x_1 is the obtained fixed position of the cutting edge of the WET in the lower guide.

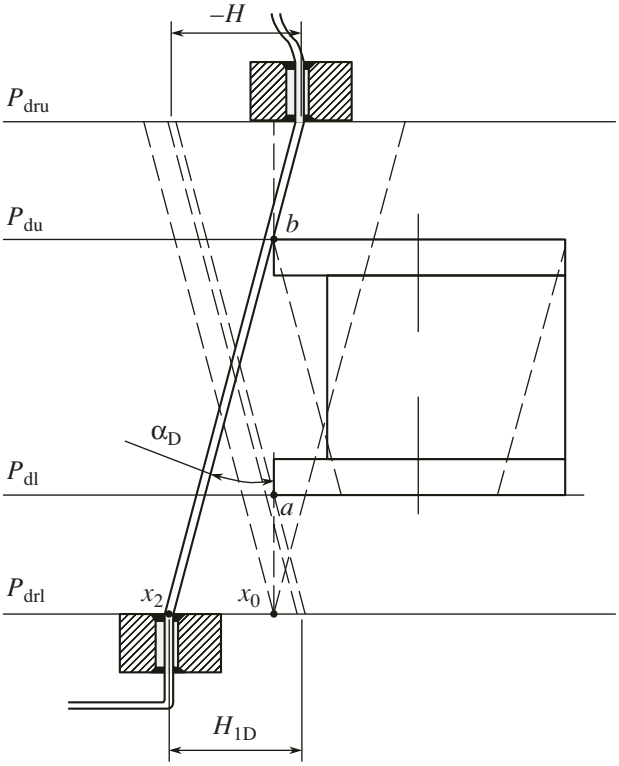

Fig. 6. Scheme of the determination of the real value of the WET shift H_{1D}.

drive contact with the upper plane of the device, we can determine the value H_{1D} (Fig. 6):

$$H_{1D} = x_0 - x_2, \qquad (6)$$

and, hence,

$$\tan\alpha_D = \frac{H_{1D} - h_D}{l}. \qquad (7)$$

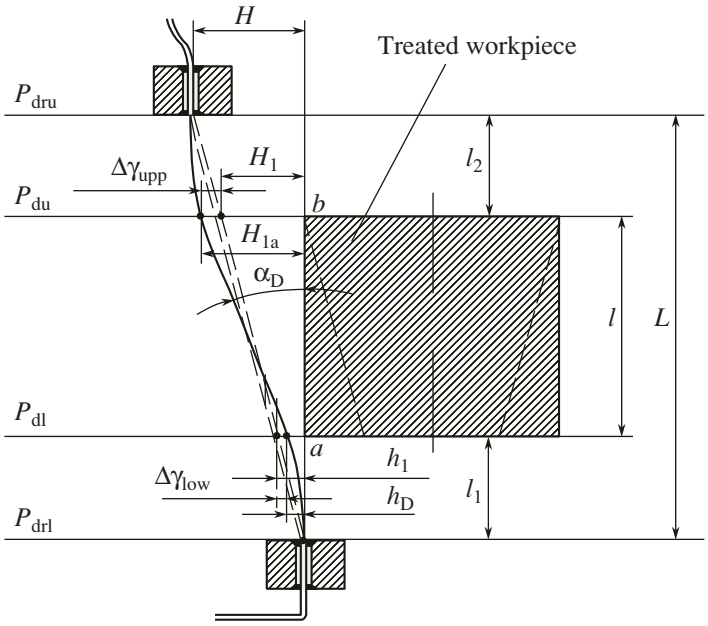

Fig. 7. Calculated and real positions of the WET upon the formation of the specified treatment inclination angle

Having obtained the values h_{1D}, H_{1D}, and α, we can estimate the deviation of the real position of the WET from the calculated one (Fig. 7):

$$\Delta\gamma_{low} = h_1 - h_D, \quad (8)$$

$$\Delta\gamma_{upp} = H_1 - H_{1D}, \quad (9)$$

$$\Delta\alpha = \alpha - \alpha_D. \quad (10)$$

Having obtained the real values of $\Delta\gamma_{upp}$, $\Delta\gamma_{low}$, and $\Delta\alpha$ using 2–4 purposeful iterations, we can select a new value for H, at which $\alpha = \alpha_D$ and $\Delta\gamma_{upp} = \Delta\gamma_{low}$ within the error of precision of the machine drive positioning. Under this condition, at the stage of the technological process projection, it is not difficult to form a trajectory of motion of the feed drives, which will compensate the wire-shift influence on the conical-surface formation precision.

CONCLUSIONS

1. The developed experimental technique allows us to determine and correct, to a precision of positioning of the feed drives of a concrete type of four-coordinate EECM, the WET position with respect to the workpieces upon formation of conic surfaces and to obtain precision for the four-coordinate treatment at the level of the two-coordinate treatment for specific types of machines, without the application of the WET position control system.

2. Due to its simplicity and universality, the determination of the WET position at the development and installation of the corresponding software may be performed automatically.

REFERENCES

1. Patent CH 681702 A5, B23H, Schneiddrahtfunkenerosionsmaschine. Mitsubishi Denki Kabushiki Kaisha, Chiyoda-ku/ Tokyo (JP), 1993.
2. Patent CH 655884 A5, B23H, Machine a teles orientables pour decoupage par electroerosion. Charmilles Technologies S.A. Geneve, 1986.
3. De Bruyr, H.E., Pekelharing, A.J., Comparison of Various Erosion Systems with Rectangular and Trapezoidal Pulse Forms, *Annals of the CTRP*, 1994, vol. 29, no. 1, pp. 103–106.
4. Jeswani, M.L., Dimensional Analysis of Tool Wear on Electrical Discharge Machining, *Wear,* 1979, 55, no. 1, pp. 153–161.

ISSN 1068-3755, Surface Engineering and Applied Electrochemistry, 2007, Vol. 43, No. 4, pp. 291–296. © Allerton Press, Inc., 2007.
Original Russian Text © E.A. Ivliev, 2007, published in Elektronnaya Obrabotka Materialov, 2007, No. 4, pp. 71–78.

OPERATING EXPERIENCE

Electroosmotic Drying of Building Walls and Basements

E. A. Ivliev

St. Petersburg State Marine Technical University, ul. Lotsmanskaya 3, St. Petersburg, 190008 Russia

Received December 25, 2006

Abstract—The basement and wall electroosmotic drying is considered. The drying duration is shortened by several months by the application of a 200-V DC power supply. The data are presented for the field measurements obtained during the industrial drying of 4000-sq.-meter rooms.

DOI: 10.3103/S1068375507040114

INTRODUCTION

In the long-term exploitation of buildings and constructions, the hydroinsulation materials partially or totally lose their protective properties. Thus, the subsoil waters penetrate freely into concrete and brick constructions of the building. The height of the capillary moisture, in particular, for basements in clayed soils, can reach up to 5 m or higher. Furthermore, the temperature-humidity regime is distorted in such buildings, which is inadmissible not only for residential, but also for most industrial constructions.

Building wall overmoistening removal consists of the two stages: wall and basement drying; and hydroinsulation recovery.

The main techniques for the horizontal hydroinsulation recovery are as follows: consecutive wall sawing and hydroinsulation substance insertion into the chinks produced; mechanical hammering of the corrugated stainless-steel sheets into the brickwork chinks using a vibration-percussion facility (BOUMAN technology, Germany); impregnation by different hydrophobic or polymer compounds pressurized or via injections through the holes drilled in the lower wall foundation (SCHOMBURG technology, Germany, technology).

After the hydroinsulation recovery, the building wall drying takes place due to natural convection over two to three years.

Of particular importance are the wall and basement drying techniques based on the electroosmotic transfer of the brick/concrete pore moisture in the direction opposite to the forces of the capillary raise or suction forces. These techniques can be divided into two groups—active and passive. In both cases, the electroosmotic-drying facility contains a set of electrodes and anodes placed inside the dried wall or at its surface and a set of electrodes and cathodes placed, as a rule, in the ground.

The passive techniques do not require a power source; here, the electroosmotic forces occur due to the electrochemical voltage difference of the anode and cathode metals. The drying duration of up to three years (comparable to natural wall drying after hydroinsulation recovery) is the essential weakness of the passive technique. This duration is caused by the fact that the voltage difference between the wall and the ground is less than 1 V. Although the electroosmotic forces occur in the wall and prevent the capillary rising of the ground moisture, the energy produced is insufficient to transfer the extra moisture from the wall into the ground.

Active techniques are based on connecting an external power source between the anodes and the cathodes, thus producing forces sufficient for the moisture transfer against the capillary rise across the entire wall thickness and height. Yet, active electroosmotic drying techniques apply low (12–24 V) voltage power sources (e.g., ELKINET technology, Austria, and HYDROPOL and DRYMaTec technologies, Germany). Thus, the certified drying duration is as long as three years, which does not differ from passive techniques.

Electroosmosis has been used in the building industry for a long time. The examples of the passive and low-voltage active techniques of electroosmotic drying are presented in [1].

The Romanian scientist Stefan Morarau made the most important contribution to the theoretical grounding of the electroosmotic drying of capillary-pored materials [2]. He was the first to study efficient electrode placing and presented simple approximate expressions to estimate the active and passive drying ratios. Then, hydrophobic compounds were proposed to feed into the tubular anodes during electroosmotic drying [3]. Different weakly soluble anode designs were proposed by Hans Oppitz, Austria [4–7]. Utklev Kjell's efforts in Norway [8, 9] substantiated the pulsed-power supply regimes to take into account corrosion resistance of the anode electrodes. Similar problems are discussed in [10].

The technical implementation of the active drying technique under higher voltages (150 to 200 V) requires, in addition to special protection measures, taking into account the following specific factors: the pattern of anode placement in the wall to be dried as

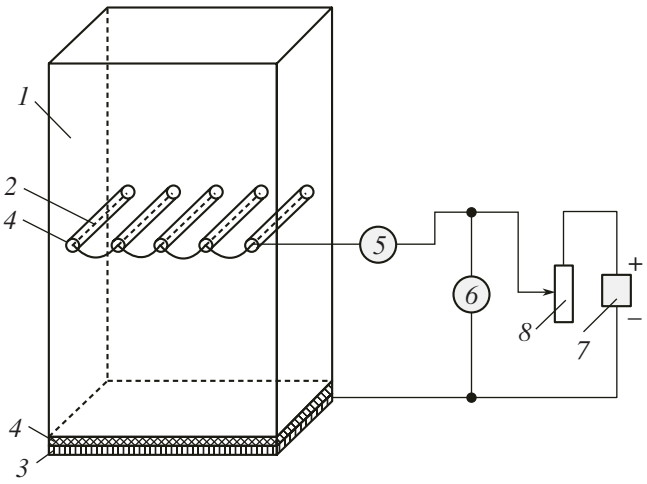

Fig. 1.

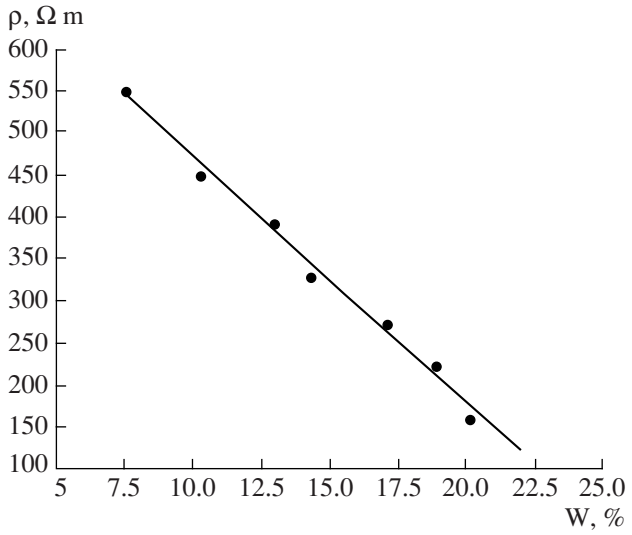

Fig. 2.

well as the power supply regimes should provide for uniform drying across the entire depth and height; the cathode arrangement should be done taking into account the ground surface location against the drying boundary needed; special measures should be taken to prevent anodic dissolution and gas release from the anode surfaces; and the anode and the cathode location should be completed taking into account the different metal constructions present in the walls and in the soil.

The goal of the present work is to substantiate the layout and the regimes of active electroosmotic drying with the use of voltages of up to 200 V, thus providing a shortening of the drying duration by up to 3–4 months [11]. The results presented generalize both the theoretical, laboratory, and field investigations and large-scale practical works.

LABORATORY EXPERIMENTS AND ANALYSIS

Laboratory studies of active electroosmosis were performed on red 260 × 130 × 70 mm^3 bricks previously dried in a thermal furnace and weighed. After a two-week brick soaking, the maximum absolute humidity was determined according to the expression

$$W_A = \frac{G_0 - G}{G} \times 100\% = 22.4\%,$$

where G is the dried-brick weight and G_0 is the humid-brick weight.

Table 1. Measurement of the humidity and the specific electrical resistivity

W_A, %	20	18.8	17.1	14.2	12.9	10.2	7.5
ρ, Ω m	160	225	275	330	395	450	550

Figure 1 shows the experimental setup for the electroosmotic drying of the brick. Here, 1 is the brick, 2 represents the anodes, 3 is the cathode made of steel mesh, 4 is the concrete compound, 5 is the ampermeter, 6 is the voltmeter, 7 is the DC power supply, and 8 is the adjusting resistor. The anode–cathode distance was equal to 0.13 m (the 1-mm steel wire anodes were placed into the holes drilled in the central brick area).

After electrode assembly, the initial absolute humidity of the brick was as high as 20%. After the power supply was turned on, drying was performed for 12 h.

The following results were obtained:

The average anode–cathode voltage was 135 V;

The average electric-field strength was 1000 V/m;

The average current was 0.1 A;

The average anode-current density was 60 A/m^2;

The specific electrical energy consumption was 800 kW h/m^3;

The absolute brick humidity at the end of the experiment was 7.5%.

Thus, after 12-h active electroosmotic drying, the brick humidity decreased by 12.5%.

During the drying process, the humidity and the specific electrical resistivity were periodically measured (Table 1). On the base of the date in Table 1, using the linear regression technique, an empirical expression is obtained for the specific resisitivity-to-humidity correlation:

$$\rho(W_A) = -29.3W_A + 763, \quad (1)$$

where ρ is expressed as [Ω m] and W_A is in %.

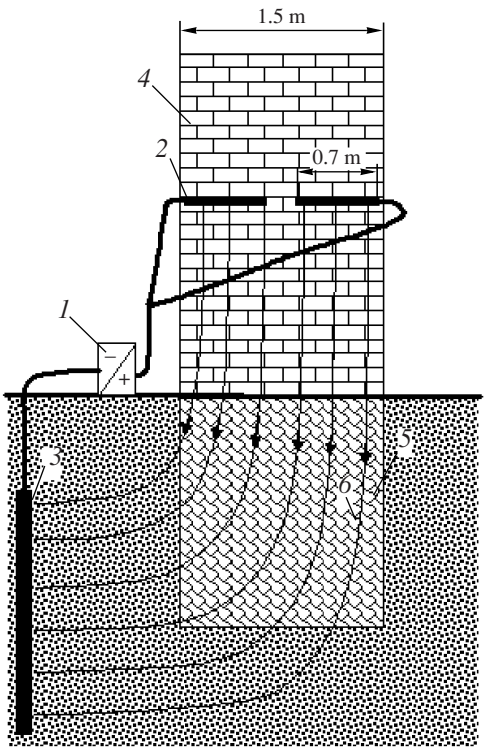

Fig. 3.

Figure 2 shows the dependence of the specific electrical resistivity on the humidity according to Eq. (1) and the data given in Table 1.

During the actual process of building drying, providing an electric-field strength of about 1000 V/m is not possible, because this value is proportional to the drying ratio. The electroosmotic velocity of the fluid moving in a capillary-pored media is governed by the expression

$$v_E = k_E E,$$

where k_E [m^2/V d] is the electroosmosis coefficient.

For the average electroosmosis coefficient value, 0.43×10^{-3} m^2/V d, within 12 h, the moisture will be removed from the brick height

$$H = k_E ET = 0.43 \times 10^{-3} \times 1000 \times 0.5 = 0.215 \text{ m}.$$

Thus, within 12 h, the moisture is actually totally removed from the brick.

The experimental results show that the duration of building-construction electroosmotic drying, using a 200-V power supply and anode–cathode distances of about several meters, can be shortened by up to several months.

PRACTICAL ASPECTS

Active electroosmotic drying was performed within the framework of the reconstruction of a house built originally between 1825–1836 in Kronshtadt City to accommodate the 1st Corps of Naval Cadet. The ground floor represents an arch-brick construction over a stone foundation. The wall depth is 1.5 m, the building hydroinsulation was destroyed, without a basement. The moisture capillary-rising level of the ground-floor walls was as high as 2–2.5 m. The brickwork humidity within the moistening zone was as high as 20–22%—that is, total fluid saturation. The renovation was performed during three 3-month stages. Within this period, 930 running meters of walls were dried, embodying 4000-m^2 lodgments. Here, 900 anodes were placed inside the building walls forming 48 independent power-supply circuits. The anode and cathode location pattern is consistent with that in [11] and is presented in Figs. 3–5. Here, 1 represents the DC power supply, 2 indicates the anodes, 3 refers to the cathodes, 4 indicates the wall to be dried, 5 shows the foundation, 6 indicates the lines of the electrical current, and 7 shows the moisture capillary-rising level in the wall.

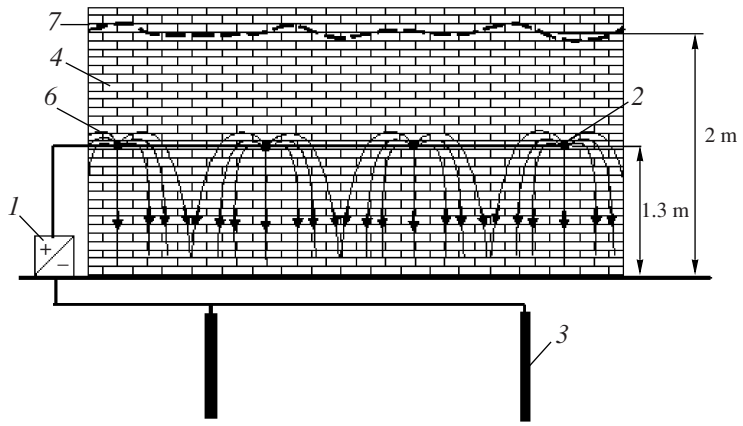

Fig. 4.

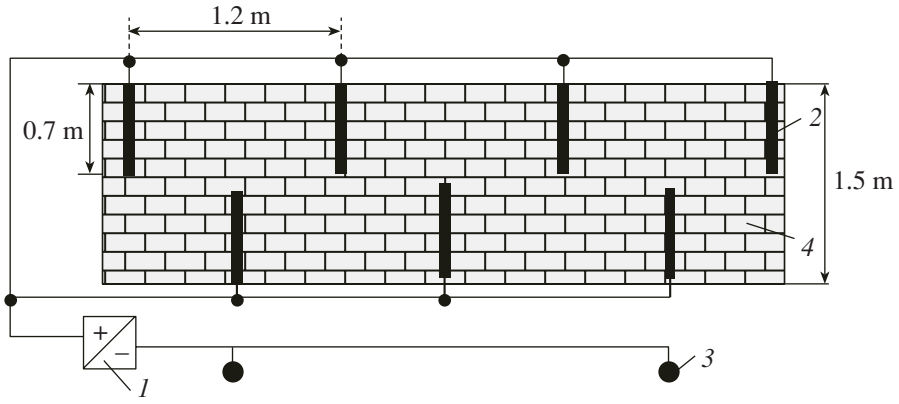

Fig. 5.

Intensive anodic dissolution is one of the main problems connected with the use of voltages of up to 200 V:

$$G = D_E I_A t,$$

where G is the material mass losses in kg, I_A is the anode current in A, D_E is the metal-mass electrochemical equivalent in kg/(A h), and t is the drying duration in h.

To mitigate anodic dissolution, graphite powder was added to the concrete compound filling the free space between the anodes and the brickwork. Graphite, like metal, possess electron conductivity; thus, no chemical reaction takes place at the boundary of these two materials and the steel anode is not exposed to dissolution at the points of contact with the graphite. Furthermore, the mass electrochemical equivalent of graphite, $D_E = 0.91 \times 10^{-5}$ kg/(A h) is two order less than the same measurement of steel, $D_E = 1.04 \times 10^{-3}$ kg/(A h).

Before drying, the absolute mass humidity was measured on the reference brick samples. From the data of 10 measurements, $W_A = 21\%$. The volume of the brickwork at that humidity was equal to 300 m^2.

During the first stage, the electroosmotic facility was connected to a 150–160-V power supply. After three months, the facility was transferred to the hydroinsulation regime with an automatic 6–12-V voltage regulation [11].

FIELD MEASUREMENTS AND ANALYSIS

Detailed study and observations of the drying process were performed over an area including three lodgments with a 100-m running length wall. Here, the electroosmotic system was connected to an independent power source with a controlled output voltage of 152 V. The anode set included 136 metal bars, 0.7-m long and 0.032-m in diameter, placed into holes 0.05-m in diameter using the concrete–graphite compound. Against the wall height, the anodes were placed at a distance of 1–1.5 m from the floor. The anodes were combined into 14 sections, thus making it possible to control each section current. The 10 cathodes were made of 3-m steel tubes, 0.05-m in diameter, and were placed inside and outside the building.

After three months of drying, the wall humidity was measured using the microwave technique. According to the data of 12 measurements, the average absolute humidity value was equal to 12%. Thus, during the drying process, the wall humidity decreased by 9% and some 50 m^3 of water was removed from the 100-m wall to the soil.

Figure 6 shows the layout of the measurement contact electrodes established at the reference area to measure the potential distribution over the wall depth and height. Here, 1 represents the electrodes to measure the potential over the wall height, 2 shows the electrodes used to measure the potential along the wall (placed every 0.2 m); and I, II, and III are the electrical resistance measuring electrodes.

To control the brickwork electrical resistance, three measurement electrodes (0.05-m in diameter and 0.7-m long) were placed at heights 0.4, 1.0, and 1.6 m from the floor level.

Tables 1, 2, and 3 present the measurement data; note that the data from Tables 2 and 3 represent fewer measurements after two months, because plastering was performed in the lodgments and the measurement electrodes became inaccessible.

Table 2 presents the data on the integral electrical characteristics at the power supply output; here, U is the output current, I is the total current, R is the total load resistance of the power supply, and T is the electroosmotic drying duration. During drying, the electrical

Table 2. Measurement of the integral electrical characteristics

T, d	1	7	20	30	40	90
U, V	152	152	152	152	152	152
I, A	42	28.5	26	22	16.8	15
R, Ω	3.6	5.3	6.1	6.9	9.05	10.1

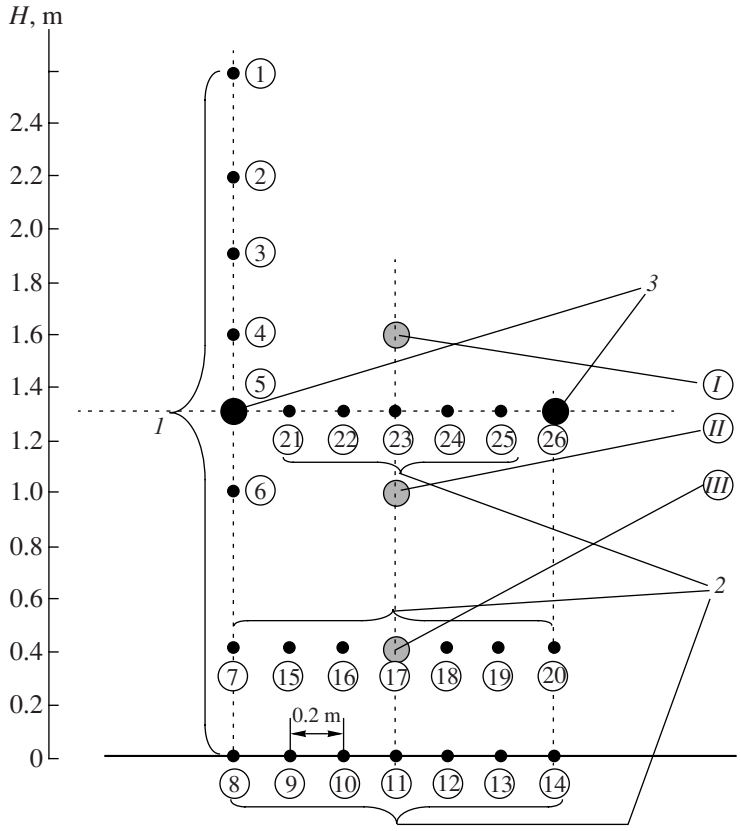

Fig. 6.

energy consumption was equal to 8000 kW h; that is, to remove 1 m^3 of water from the wall, 160 kW h is required.

Table 3 presents the data on the measurement of the electrode-spreading resistance against the cathode system. Note that the drying process is not uniform. Here, H is the electrode height from the floor, R is the spreading resistance, and T is the electroosmotic-drying duration. The data show that the upper portions of the wall dry faster, whereas in the lower part, noticeable resistance only changes take place after a month of drying. Thus, the area above the anodes is dried faster. The specific electrical resistivity in the vicinity of the measurement electrodes can also be determined. Since the measurement electrode resistance was measured against the cathode system, for which the resistance is far lower than a similar measurement electrode, the following expression can be taken for the bar electrode:

$$R = \frac{\rho}{2\pi L}\left[\ln\left(\frac{2L}{a}\right) - 0.307\right][\Omega],$$

where ρ is the specific electrical resistivity of the media, and L and a are the electrode length and radius in m, respectively.

For the given dimensions of the measurement electrodes, the specific electrical resistivity is determined from the expression

$$\rho = \frac{R}{0.845}, \ \Omega \text{ m}. \quad (2)$$

According to Eq. (2), the initial value of the spreading resistance of the measurement electrodes (120 Ω) corresponds to the 142-Ω value of the specific electrical resistivity of the brickwork–that is, according to (1), up to an absolute humidity value of 21.3%—thus being in good agreement with its direct measurements (21%) before drying was initiated. After 60 d, the specific electrical resistivities at the measurement electrode locations were equal to 166, 296, and 331 Ω, thus cor-

Table 3. Measurement of the control electrode spreading resistance

H, m	R, Ω	T, d			
		1	14	30	60
0.4	R_{III}	120	120	130	140
1.0	R_{II}	120	159	200	250
1.6	R_{I}	120	197	230	280

Table 4. The potential distribution over the wall height (a) and length (b)

(a)

H, m	U, V	T, d				
		1	7	20	30	40
2.6	U_1	120	111	104	93	89
2.2	U_2	121	113	106	95	92
1.9	U_3	124	116	110	101	96
1.6	U_4	128	120	115	105	101
1.3	U_5	152	152	152	152	152
1.0	U_6	118	111	107	95	94
0.4	U_7	79	72	68	61	56
0.0	U_8	50	50	49	47	46

(b)

H, m	Electrode number (see Fig. 5) and potential value								δ, %
1.3	N	5	21	22	23	24	25	26	27
	U, V	152	125	118	111	118	125	152	
0.4	N	7	15	16	17	18	19	20	14
	U, V	90	85	81	79	81	85	90	
0.0	N	8	9	10	11	12	13	14	4
	U, V	50	50	49	48	49	50	50	

responding to the absolute humidities of 20.4%, 15.9%, and 14.7%, respectively.

The nonuniformity of the drying process is also justified by the data from the potential measurement over the wall height presented in Table 4, where U is the potential against the cathode, and H and T are the same as in Table 3.

For the drying process, the potential nonuniformity over the wall height is also important. This nonuniformity is maximally manifested between the neighboring anodes of the electroosmotic system. Above and below the anodes, the potential distribution over the wall length is more uniform; this is confirmed by the measurement data presented in Table 4, where $\delta = \frac{U_{\max} - U_{\min}}{U_{\min}} \times 100\%$ is the degree of the potential nonuniformity. Table 4 also shows that the potential nonuniformity along the wall is negligible. Thus, the "plane condenser" model can be applied to engineering calculations.

Taking into account the fact that the potential difference between the anodes and the floor level is about 70 V, the electrical-field strength between the anodes and the floor is equal to 54 V/m. Thus, the electroosmotic fluid motion ratio inside the wall is $v_E = k_E E = 2.3$ cm/day. Hence, over three months, the moisture will be removed from the brickwork at the height $H = v_E T = 0.023 \times 90 = 2.1$ m.

Thus, the use of voltages of up to 200 V makes it possible to remove excess moisture from building walls and basements over several months.

CONCLUSIONS

1. The active electroosmotic technique of building wall and basement drying is validated with the use of power supply voltages of up to 200 V, thus providing a shortening of the drying duration of up to several months.

2. The drying process can be controlled by measuring the spreading resistances of special electrodes placed over the wall height at distances far exceeding their transverse dimensions.

3. Graphite electrodes or metal electrodes with a graphite cover have the best characteristics concerning anodic dissolution. After active electroosmotic drying, the electrode system remains operable for electroosmotic hydroinsulation when connected to a low-voltage 6–12-V power supply.

REFERENCES

1. Kad'erg, P., *Izolyatsiya i predokhranenie zdanii* (The Building Insulation and Protection), Moscow: Gosstroizdat, 1957.
2. Morarau S., Patent US 3 856 646 Int. CI B01D13/02, Filed dates 20.10.1972.
3. Bacinski A., Patent GB 2 101 188 Int. CI4 E04B1/70, Filed dates 01.12.1983.
4. Oppitz H., Patent US 4 600 486 Int. CI4 B01D13/02, Filed dates 26.10.1984.
5. Oppitz H., Patent DE 3 541 656 Int. CI4 B01D13/02, Filed dates 05.06.1986.
6. Oppitz H., Patent DE 3 714 943 Int. CI4 E04B1/70, Filed dates 12.11.1987.
7. Oppitz H., Patent DE 4 329 219 Int. CI4 E04B1/70, Filed dates 03.03.1994.
8. Kjell U., Patent WO 9 010 767 Int. CI4 E04B1/70, Filed dates 0.09.1990.
9. Kjell U., Patent EP 0 839 240 Int. CI4 E04B1/70, Filed dates 02.06.1997.
10. Miller J., Patent US 5 015 351 Int. CI4 B01D13/02, Filed dates 14.05.1991.
11. Ivliev, E.A., Iossel, Yu.Ya., Kazarov, G.S., Konstantinov, E.V., Lipatov, V.V., Patent RU 2 103 054 MKI5 B01D61/56, *Byull. Izobret.*, 1998, no. 3.

ISSN 1068-3755, Surface Engineering and Applied Electrochemistry, 2007, Vol. 43, No. 4, pp. 297–302. © Allerton Press, Inc., 2007.
Original Russian Text © E.D. Pleshka, 2007, published in Elektronnaya Obrabotka Materialov, 2007, No. 4, pp. 79–85.

OPERATING EXPERIENCE

Laser Hardening of Iron-Alloyed Coatings

E. D. Pleshka

Institute of Applied Physics, Academy of Sciences of Moldova, ul. Academiei 5, Chisinau, MD-2028 Republic of Moldova

Received February 28, 2007

Abstract—The results of the investigation of the process of laser treatment of iron-alloyed coatings, and of the structure and wear resistance of the surfaces, obtained in a methyl-sulphate-chloride electrolyte are reported. It is established that, in a multicomponent electrolyte, it is possible to obtain coatings with a thickness not less than 3 mm with a fibrous, granular, and stratified structure. The formation of many macrozones, characterized by different structure and phase transformations, is possible through CO_2 laser treatment (LT) of iron-alloyed coatings (IAC). Restored and hardened surfaces of internal-combustion engine parts under conditions that ensure the generation of an amorphous layer have a wear resistance several times higher than untreated alloyed electroplated coatings.

DOI: 10.3103/S1068375507040126

Modern electrophysical, thermal, and other methods of growing worn surfaces of parts with various substances in order to restore their geometric shapes and sizes, as well as to harden them, do not always ensure a high quality of compatibility with specifications. However, they are implemented for the recovery of a wide nomenclature of machine elements and, because of an acute need, for the reduction of important components of internal-combustion engines such as crankshafts, camshafts, etc.

The analysis of the known methods of component restoration through electroplating showed that the use of alloyed coatings based on iron might be very promising for factory overhaul.

The significant advantages of the alloyed-iron coatings obtained in stable electrolytes in compared with normal iron coatings are worth mentioning. They former possess high mechanophysical properties, are wear resistant, and fit, to a certain extent, the working conditions in different conjugations.

Special chemicothermal treatment of parts may be an important reserve in order to improve the quality of restoration and hardening by electroplating. In such cases, some particular requirements are placed upon the coatings, such as a high-bonding strength, a significant thickness, a thermal stability, the presence of alloying elements, etc. [1, 4].

Thus, solving the problem of obtaining adhesive iron coatings, alloyed using special elements, to improve their properties and ability to be hardened using various methods (Fig. 1 and 2) was a worthwhile exercise. It was established [4, 6, 7] that laser treatment with flows of power densities of up to 10^9 W/cm^2 provides the possibility to perform a large number of structure-phase transformations in alloyed-galvanic coatings and to obtain properties suitable under different conditions of their service.

RESEARCH METHODS AND MATERIALS

The process of electrolysis in a multicomponent methyl-sulphate-chloride electrolyte to the properties of adhesive iron-alloyed coatings, applied to samples and elements manufactured from construction steels using special high-grade gray cast irons, as well as the process of laser treatment of iron-alloyed coatings and restored parts, is the object of this investigation.

The material structure and hardness were examined using the metallography technique with the aid of MIM-8, MBI-6, and PMT-3M microscopes and an REM-200 electron microscope.

The mechanical processing of polished specimens, samples, and parts was carried out by commonly

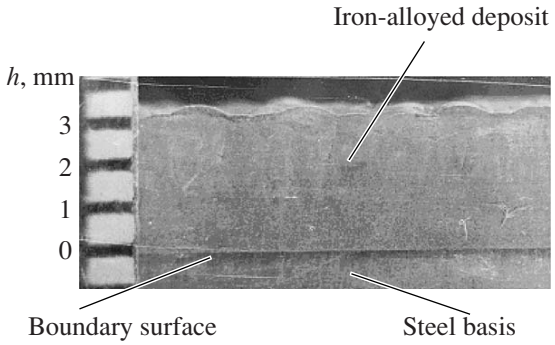

Fig. 1. Thick-layer iron-alloyed coatings, obtained in a multicomponent methyl-sulphate-chloride electrolyte, applied on a carberized chilled steel (HRC 54-56).

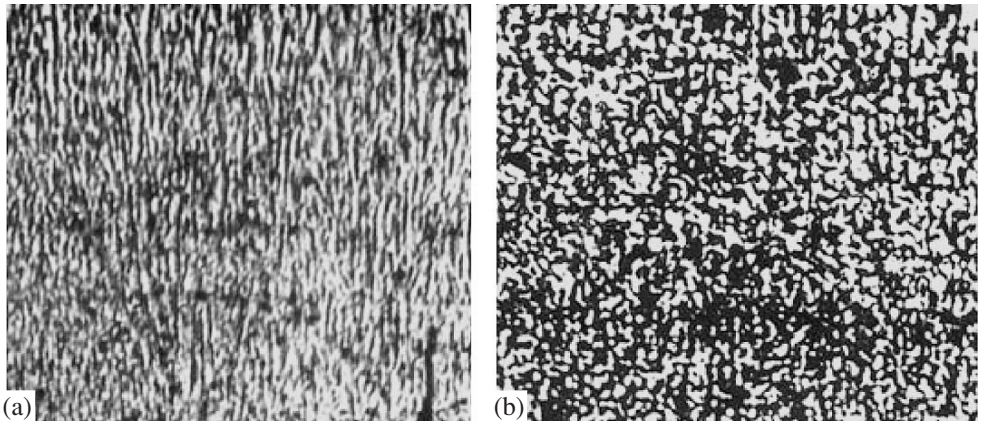

Fig. 2. Structure of iron-alloyed coating: (a) fibrous structure; (b) granular structure (800 × 4).

accepted methods to fit the specifications. Laser processing using a CO_2 laser was conducted under continuous conditions with a power flux of 0.5–0.6 kW with a radiation wavelength $\lambda = 10$ μm. The intervals of the production-cycle change during the analysis of the laser treatment of iron-alloyed coatings were determined to meet the recommendations for processing steels and cast irons [5] with regard to the thermophysical properties of the materials and the energy characteristics of the radiation flux. Estimations of the sample material characteristics and the properties of the saturation of surface and diffusion layer were in accordance with GOST 20495-75.

In the available literature, there is no information on the processes of iron-alloyed galvanic-coating treatment using energy-intensive fluxes produced by lasers. In this connection, to determine the conditions that ensure various types of iron-alloyed coating treatment, factors influencing their properties and structure-phase transformations were analyzed. The calculated regimes were used in the experimental investigations to process the samples, and to restore and harden parts. The laser-effect estimation was performed through the examination of the diffusion layer of the outer areas, including the general and effective thickness of the diffusion layer and the rough surface configuration effects.

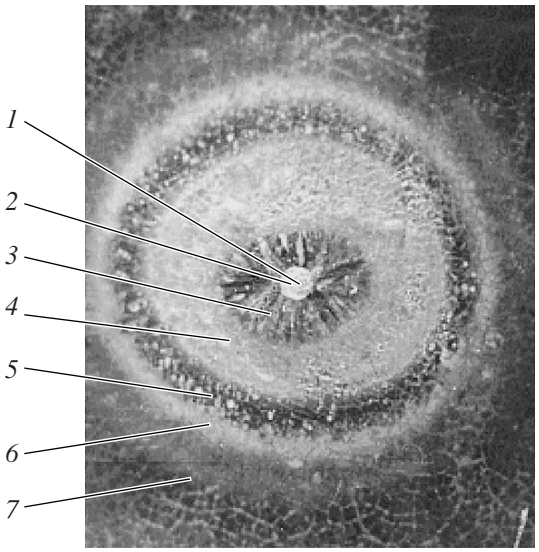

Fig. 3. Macrozones of structure transformations of iron-alloyed coatings treated by a continuous CO_2 laser.

RESULTS

The treatment of iron-alloyed coatings using highly intensive energy fluxes, ensuring that the structure transformation processes take place with substantially larger rates than processing using traditional methods, is the most sound and effective method.

For the process of coating-material treatment using energy fluxes characterized by density P_i, speed of movement or exposure time t_0, the conditions of the qualitative treatment in the general form can be presented by the expression

$$AP_{kmin}t_0 < A(P_i \pm \Delta P_i)t_0 < AP_{kmax}t_0, \qquad (1)$$

where P_k is the energy density critical value, ΔP_i is the flux-density change during the treatment process, and A is the complex parameter characterizing the effect of different factors on the treatment process.

By changing the treatment conditions (flux density, exposure time, or other factors), it is possible to vary the level of radiation acting upon the coating being processed, which leads to a change in the mechanophysical properties and geometrical characteristics of the surface and diffusion layer.

The time of the continuous radiation effect on the processes surface t_0 at any point upon the displacement

of the beam with diameter d_l is described by the known equation

$$t_o = \frac{2t_d\sqrt{r_l^2 - a_1^2}}{\sqrt{b^2 + (\pi d_d)^2}}, \quad (2)$$

where r_l is the radiation flux-beam radius, mm; a is the distance of the point from the diametric axis of the direction of movement, mm; b is the treatment-delivery step, mm/rev; d_d is the part diameter, mm; and t_d is the revolution period of the part, s.

The maximum energy absorbed by the electroplating elementary section that crosses the radiation flux in the diametric plane and coincides with the direction of movement direction can be determined from equation

$$W = \frac{P_i A d_l t_d}{\sqrt{b^2 + (\pi d_d)^2}}. \quad (3)$$

Complex parameter A incorporates the radiation energy-absorption coefficient depending upon the temperature and character of the laser radiation spectra, the absorption spectra, the radiation, and the workpiece medium components; the roughness of the surface, its reflective or radiating power; and the energy release or absorption during the process of phase transformations. Other factors influencing the process can be introduced in accordance with the type of treatment and the electroplating material thermophysical properties.

For sections situated at distance a from the displacement direction axis, the energy absorbed by the surface elementary part can be determined using the formula

$$W = \frac{2P_i\sqrt{r_l^2 - a_1^2}t_d}{\sqrt{b^2 + (\pi d_d)^2}}. \quad (4)$$

According to [5], the rates of heating and cooling and the relationship between the temperatures of the electron gas (T_e) and the crystal lattice (T_i) play the governing role for the processes of phase transformations upon multicomponent system hardening. We believe that the approximated definition of this relation can serve as a criterion of validity of the production cycles or as the probability of achieving the phase transformation conditions in alloyed-electroplating coatings. To determine them, we can use the known equation [5]

$$(T_0 - T_i)_{\max} = \frac{2q}{\alpha\sqrt{\pi a\tau}}, \quad (5)$$

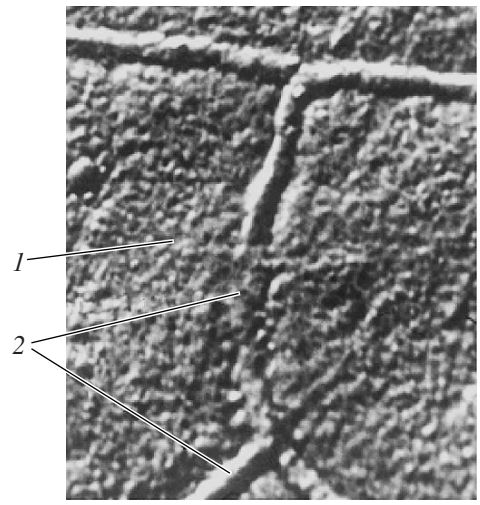

Fig. 4. The surface of an amorphous layer of an iron-alloyed coating treated by a CO_2 laser (3000 × 2): 1, amorphous surface layer; 2, amorphous layer in the microcrack areas.

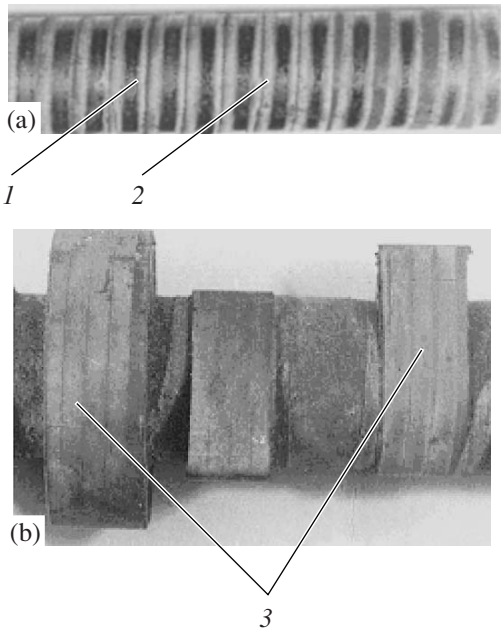

Fig. 5. Surface of internal-combustion engine parts treated by a continuous CO_2 laser: (a) wrist pin; (b) camshaft.

where q is the radiation flux density, α is the coefficient of the heat transfer between the electrons and the lattice; a is the temperature-conductivity coefficient of the electron gas, and τ is the laser-radiation exposure time.

The above equation most likely characterizes the process of the laser-radiation effect on pure metals with a more perfect crystal structure. In the case of an electroplating-iron coating, it can only be applied to approximate calculations. Substituting into it the flux density values and exposure time from equations (1)–(4) for the

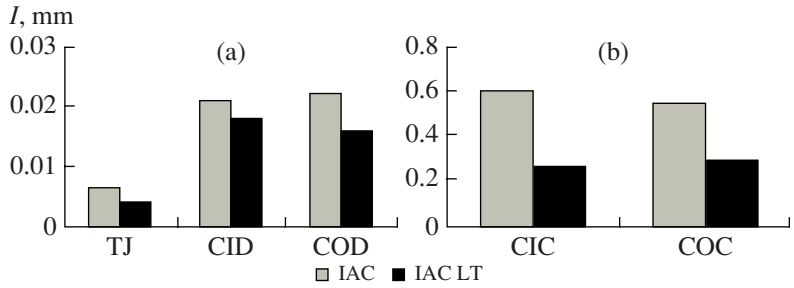

Fig. 6. Wear I of internal-combustion engine camshafts restored using iron-alloyed coatings (IAC) and treated by a laser (IAC LT): (a) wear of the thrust journals; (b) wear of the cams.

processes of continuous radiation treatment at material displacement, we obtain

$$(T_e - T_i)_{\max} = \frac{2(P_i + \Delta P_i)A}{\alpha\sqrt{\pi a \dfrac{d_l t_d}{\sqrt{b^2 + (\pi d)^2}}}}. \qquad (6)$$

Taking into account the complexity of the calculations in multicomponent materials and the effect of the energy transfer between phases with different heat capacities, it is worthwhile calculating the temperature from the average material heat capacity. For technological calculations, the coating surface-layer temperature can be determined from the expression

$$T_n = \frac{K_1 W}{K_2(c_1 m_1 + c_2 m_2 + \ldots + c_n m_n)}, \qquad (7)$$

where c and m are the heat capacities and masses of the components and certain phases of the coating-material structure, respectively; K_1 the coefficient accounting for the energy absorption; and K_2 is the coefficient accounting for the interaction of the heat flow between the phases of the coating material.

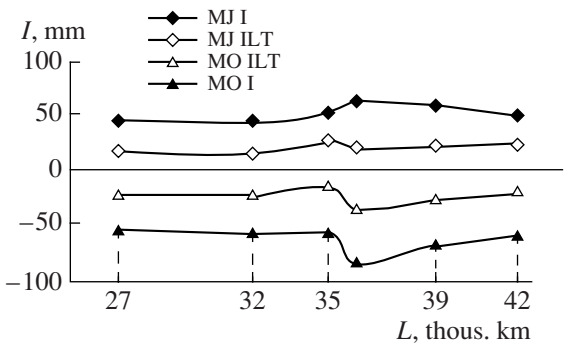

Fig. 7. Wear I of internal-combustion engine-crankshaft main journals and bushings depending on the car landing run L, restored using iron-alloyed coatings (IAC) and treated with a laser (IAC LT).

Using the presented equations, dependencies, and the thermophysical characteristics of the substances, it is possible to calculate the necessary specifications and conduct test estimations for the treatment of materials and parts.

To improve the quality and obtain particular properties, it is expedient to determine the regime-critical parameters (flux density, exposure time, surface-layer temperature) to ensure polymorphous phase transformations and the chemical processes of the formation of amorphous phases of intermetallic compounds. Such phase transformations as evaporation and partial melting of the surface layer, which cause changes to the surface geometric characteristics because of configuration effects, are acceptable within the limits of the requirements of the product.

Equations (1)–(6) can more plausibly describe the phenomena of the process under the conditions of a high uniformity of the energy-flux density in the normal beam section. Actually, for instance, for CO_2 lasers with continuous operation, the energy-flux density in the beam diametric section has explicitly pronounced maximums in the central regions. This factor manifestation is revealed experimentally at varying conditions of iron-alloyed coating treatment. Thus, at the energy-flux density causing evaporation in the central area (of the beam action) and partial-melting of the material, at certain time cycles, seven ring macrozones appear (see Fig. 3) with peculiar levels of conversion of the initial surface and depth states accompanied by the formation of different structures owing to the phase transformations achieved at the respective temperatures (Fig. 3). Changing the beam energy-flux density and time of action on an iron-alloyed coating within the limits of the conditions necessary to achieve the temperature of evaporation and melting up to the temperatures below the critical values, causes a certain transformation of the structure of the surface and depth layers; thus, the possibility of obtaining a wide range of material states has been demonstrated on numerous occasions.

With the aid of metallography and electron-microscope analysis, it has been revealed that, at the transition boundary and within the limits of every macrozone, different microstructures and phase components both in the surface and depth layers of the coating have been revealed. Their generation is connected with the level of the energy effect upon laser treatment using the thermophysical and chemical properties of the components (Fig. 4). The calculation of these processes taking place in the treated alloyed coating during the stages of heating and cooling is a rather complicated problem. Thus, the conclusion on the application of one or another treatment regime might be made only after the correlation between the theoretical computation with the experimental data is carried out.

Analyzing the laser effect levels, the state of the surface and structural-depth constituents, and correlating the phase transitions with the thermophysical characteristics of the alloyed-coating components, it is possible to estimate the attained temperatures in typical areas and critical values of the energy and time conditions to obtain some properties and to determine acceptable treatment conditions.

Thus, for example, macrozone 4 is characterized by a thicker surface layer of the material subjected to amorphization, consisting of the components of the iron-alloyed coating and the components of substances applied to the surface of the coating in order to improve its ability to absorb radiation and impart to it some peculiar properties (corrosion resistance, wear resistance, etc). The iron-alloyed coating-depth layers subjected to laser treatment are characterized by such changes, manifesting themselves in the formation of new structural components, which are limited by the heat effect and the values of the heating temperatures attained and the rate of cooling. The laser treatment conditions that ensure the formation of an amorphous state in the external region of the surface layer were used to harden parts, were restored by iron-alloyed coatings, and were obtained in a multicomponent methyl-sulphate-chloride electrolyte. For surfaces working under friction at high and low speeds of the slipping-treatment regime corresponding to the formation of an amorphous surface layer through the evaporation and melting of microrelief peaks, the geometrical dimensions in the tolerance zone remain the same (Fig. 5).

Bench and operation trials of preproduction lots of crankshafts and camshafts, restored using iron-alloyed coatings, have shown the advantage of laser treatment under conditions ensuring the generation of an amorphous layer on the surface. Thus, camshaft-thrust journals (TJ), treated with a laser (IAC LT) and tested on a bench using abrasion (see Fig. 6*a*), had 30–35% less wear than those that were untreated (IAC). The diameters of the cams were worn down (CID, inlet; COD, outlet). The best improving effect was found for the laser-processed inlet (CIC) and outlet (COC) cams. Their height wear was less by a factor of 2–2.2 than for those untreated (see Fig. 6*b*). During the operational analysis of cars, the same results for the crankshafts of engines restored using iron-alloyed coatings (I) treated by a laser (LT) were obtained. The wear of the restored and laser-hardened main journals (MJ) and main bushings (MB) was less by a factor of 2.5–2.8 than for those untreated (see Fig. 7).

The theoretical and experimental investigations reported on here of the process of the production and treatment of iron-alloyed coatings using intensive fluxes of laser radiation energy give grounds for characterizing the principal virtues of the mentioned method of treatment: its high rate, the possibility of changing the structure and phase state of the alloyed coatings and their properties over wide limits, and the possibility of local treatment without disturbance of the initial structure and properties of the detail material. The application of the laser treatment method for factory overhaul is rather promising from the point of view of the improving quality and efficiency of the parts restoration process.

CONCLUSIONS

Theoretical calculations of the critical values of the treatment energy-flux density, the process kinematics, and time characteristics, performed on the basis of modern theories on the energy flux-treated material interaction have helped to determine the conditions, acceptable for technological purposes, at which there is attained a change in the properties of the surface and depth layer of iron-alloyed coatings.

Experimental results confirm theoretical predictions on the interaction of the energy flux with the iron material and iron-alloyed electroplating.

The experiments show that, by changing the iron-alloyed electroplating treatment conditions, it is possible to obtain various structures in the coating surface and depth layers.

The method of evaluating the critical states of the treated coatings, at which phase and structure transformations are obtained, is proposed.

Iron-alloyed coatings hardened by a CO_2 laser, under conditions that ensure the formation of an amorphous layer, improve substantially the wear resistance of the part surface in moving conjugations.

REFERENCES

1. Petrov, Yu.N., *Gal'vanicheskie pokrytiya pri vosstanovlenii detalei* (Electroplating Coatings at Parts Restoration), Moscow: Kolos, 1965.

2. Vyacheslavov, P.M., *Elektroliticheskoe formirovanie* (Electrolytic Forming), Leningrad: Mashinostroenie, 1979, p. 198.

3. Gologan, V.F., Effect of Electrolysis Conditions on Wear Resistance of Electrolytic Iron Coatings as Applied to the Repairing Parts of Cars, Tractors and Agricultural Machines, Cand. Sci. (Eng.) Dissertation, 1968, p. 22.

4. Pleshka, E.D., Restoration of parts by alloyed electroplating, *Proceedings on the International Workshop on Repairing Machines*, Kishinev, 1996, pp. 27–28.

5. Rykalin, I.I., Uglov, A.A., Zuev, I.V., and Kokora, A.N., *Lazernaya i elektronno-luchevaya obrabotka materialov* (Laser and Electron-Ray Treatment of Materials), Moscow: Mashinostroenie, 1985, 496 pp.

6. Pleshka, E.D., Restoration of Steel and Cast Iron Crankshafts of Engines by Iron Alloyed Coatings, *Proceedings of the Conference*, Kishinev, 1984.

7. Pleshka, E.D., Laser Hardening of Parts Restored by Iron Coatings, *Proceedings of IX All-Union Conference on Electrochemical Tehnology "Galvanotechnika 87*," Kazan, 1987.

8. Recommendations on Quick Test of Restored Parts, GOCTNITI, Moscow, 1979.

9. GOST 17510-72. Product Reliability, Mashinostroenie.

ISSN 1068-3755, Surface Engineering and Applied Electrochemistry, 2007, Vol. 43, No. 4, pp. 303–305. © Allerton Press, Inc., 2007.
Original Russian Text © M.M. Susan, R.C. Baciu, P.G. Dumitras, Z.C. Predescu, 2007, published in Elektronnaya Obrabotka Materialov, 2007, No. 4, pp. 86–88.

OPERATING EXPERIENCE

Changes in the Structure and Properties of Aluminum Alloys Solidified in an Ultrasonic Field

M. M. Susan[a], R. C. Baciu[a], P. G. Dumitras[b], and Z. C. Predescu[c]

[a] *Asachi Tehnical University, 59 D. Manjeron Blv., Iasi, Romania*

[b] *Institute of Applied Physics, Academy of Sciences of Moldova, ul. Academiei 5, Chisinau, MD-2028 Moldova*

[c] *Politehnica University, Bucharest, Romania*

Received November 8, 2006

Abstract—An ultrasonic field was applied to melted metal alloys during their solidification with the aim of obtaining their microstructure in a solid state characterized by small-sized grains. In this paper, the results of experimental research are presented, obtained under the application of an ultrasonic field of 100–350 W during the solidification of an ATC $Si_{10}Cu_4$ alloy cast in a mold.

DOI: 10.3103/S1068375507040138

INTRODUCTION

The structure of a metal alloy (its phase composition, the dimensions and shape of the grains, the distribution of the formed particles, etc.) constitutes an essential criterion that characterizes the quality of the obtained material.

The importance of the structural parameters is determined by the fact that they directly influence the physical and mechanical properties of the metal alloy.

An efficient way of improving the metal alloy structure is the use of an ultrasound action during the solidification process. Ultrasound excitation of metals in the melted state may be achieved by the direct action of an ultrasound on the bath with the melted metal, the mold, the casting form, or other intermediate devices.

Using ultrasound during the solidification of metal alloys yields materials with superior structural characteristics and improved properties [1].

1. EXPERIMENTAL METHOD

The experiments were performed on the aluminum alloy ATC $Si_{10}Cu_4$ (3.6% Cu, 0.1% Mg, 11.2% Si, 0.5% Mn, 3% Zn, the remaining—Al) and solidified in a mold under the action of an ultrasonic field produced by a 1000-W ultrasound generator (USG) using the ultrasonic (oscillating) system shown in Fig. 1.

The useful power can be varied by modifying the intensity of the premagnetization current in the oscillating system; this condition may be achieved using the step-cylindrical concentrators with various degrees of amplification of the oscillation amplitude (A = 8–25 μm).

The step-cylindrical concentrators and the micromold are made of titanium alloys resistant to ultrasonic action [2].

2. EXPERIMENTAL RESULTS

Samples of the ATC $Si_{10}Cu_4$ alloy were solidified in an ultrasonic field with the frequency of ν = 17.5 kHz and P_{us} = 100–350 W. In order to attain the maximum efficiency of the ultrasound, the ultrasonic field was switched on until the end of the solidification process.

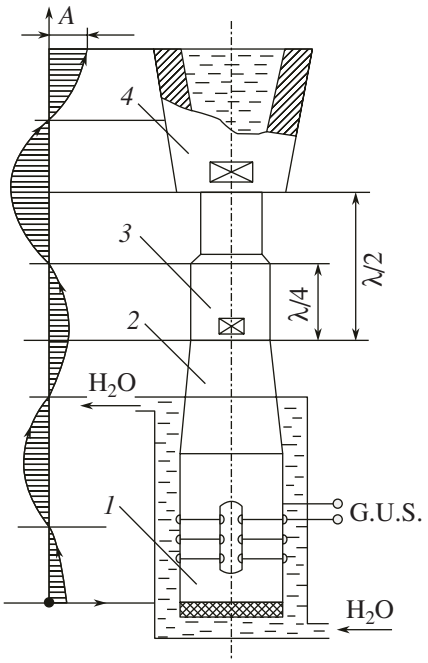

Fig. 1. Scheme of the ultrasonic system. *1*—magnetostrictive transducer; *2*—standard concentrator; *3*—step-cylindrical concentrator; *4*—micromold.

Phases found in the ATC $Si_{10}Cu_4$ alloy solidified in an ultrasonic field

Sample	Ultrasound power, P_{US}, W	Phases						Hardness, HB, N/mm^2
		Al	Cu	Si	$CuAl_2$	Cu_2O	Al_2O_3	
1	0	(111) (200)	(111) (200)	(111) (220)	(110)	–	(101)	691
2	100	(111) (331)	(111) (222)	(400) –	–	–	(123)	715
3	125	(111) (200)	(111) –	(111) (220)	(110) –	(110)	–	742
4	150	(111) (200)	(111) (311)	(111) (220)	(110)	(110)	(101) (123)	771
5	175	(111) (200)	(111) (220)	(111) (220)	(110)	(110)	(101) (123)	802
6	200	(111) (200)	(111) –	(220) (400)	(110)	–	–	831
7	225	(111) (200)	(111) (220)	(111) (400)	(110)	–	–	863
8	250	(111) (200)	(111) (220)	(111) (220)	(110)	(110)	(123) (233)	900
9	275	(111) (200)	(111) –	(111) (220)	(110) (112)	(110)	(101) (123)	942
10	300	(111) (200)	(111) –	(111) (220)	(110) (112)	(110)	(123)	981
11	350	(111) (200)	(111) –	(111) (220)	(110)	–	(112) (101)	1021

These samples were analyzed by diffractometry, and their microstructure and hardness were also investigated.

The diffractometric analysis has shown the presence of Al, Cu, and Si as distinct phases in the solid solution, as well as the presence of the chemical compounds $CuAl_2$, Cu_2O, and Al_2O_3 (table).

Microscopic investigations confirmed that the dendritic structure of the samples solidified under normal conditions (P_{us} = 0 W) transforms into the cellular structure in the samples solidified in ultrasonic field (Fig. 2).

It should be noted that the chemical compounds $CuAl_2$, Cu_2O, and Al_2O_3 can be found at the grain boundaries of the solid solution.

CONCLUSIONS

The experimental results may be explained on the basis of a decrease in the surface tension at the boundary surface between the metal melt and the micromold wall, as well as at the solid phase–liquid phase interface

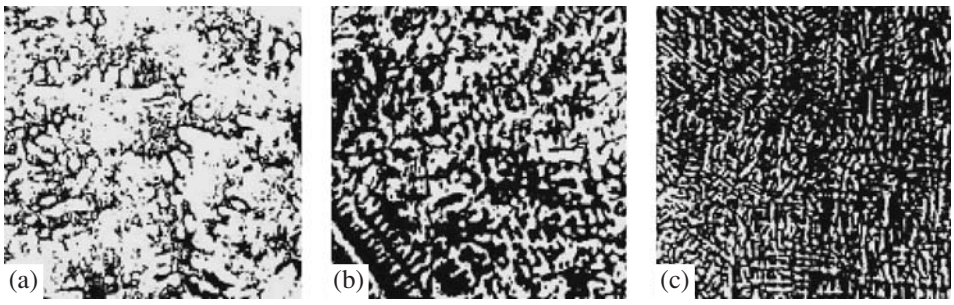

Fig. 2. Structure of the solid ATC $Si_{10}Cu_4$ alloy using (a) normal solidification; (b) solidification in an ultrasonic field, A = 8 μm; and (c) solidification in an ultrasonic field, A = 25 μm (chemical reagent, 0.5% HF; magnification, 100 : 1).

due to the increase in the adhesion between the elements in contact.

Ultrasonic excitation of the micromold decreases the degree of undercooling and increases the nucleation ability of the melted metal, favoring the formation of a fine-grain microstructure with superior mechanical properties.

An increase in the oscillation amplitude and, hence, in the ultrasound power results in a decrease in the crystalline grain size, the elimination of some solidification defects, and substantially increases the hardness of the studied alloy.

REFERENCES

1. Amza, Gh., et al., *Sisteme ultraacustice,* Bucuresti: Editura Tehnica, 1988.
2. Dragan, Ov., et al., *Ultrasunete de mari energii*, Bucuresti: Editura Academiei, 1983.